MICROWAVE STUDIES OF AN AMORPHOUS FERROMAGNET

by

Richard A. Baartman

B.Sc., Simon Fraser University 1975

A THESIS SUBMITTED IN PARTIAL FULFILLMENT OF

THE REQUIREMENTS FOR THE DEGREE OF

MASTER OF SCIENCE

in the Department

of

Physics

Simon Fraser University

April 1981

APPROVAL

Name: Rick A. Baartman

Degree: Master of Science

Title of Thesis: Microwave Studies of an Amorphous Ferromagnet

Examining Committee:

Chairman: M. Plischke

John F. Cochran
Senior Supervisor

A.S. Arrott

R.H. Enns

B. Heinrich
External Examiner
Department of Physics
Simon Fraser University

Date Approved: April 10, 1981

PARTIAL COPYRIGHT LICENSE

I hereby grant to Simon Fraser University the right to lend my thesis, project or extended essay (the title of which is shown below) to users of the Simon Fraser University Library, and to make partial or single copies only for such users or in response to a request from the library of any other university, or other educational institution, on its own behalf or for one of its users. I further agree that permission for multiple copying of this work for scholarly purposes may be granted by me or the Dean of Graduate Studies. It is understood that copying or publication of this work for financial gain shall not be allowed without my written permission.

Title of Thesis/Project/Extended Essay

Microwave Studies of an Amorphous Ferromagnet

Author: _____
(signature)

Richard A. Baartman
(name)

April 14, 1981
(date)

ABSTRACT

The technique of ferromagnetic microwave antiresonance transmission at 24GHz was used to study the magnetic properties of the amorphous ferromagnet Co_3P from 5 to 414°K. The resulting data were used to obtain the saturation magnetization, the g-factor, and the Landau-Lifshitz damping parameter, λ. The magnetization was compared with the Bloch $T^{3/2}$ law over the interval 5 - 79°K. The spin wave dispersion coefficient obtained from this comparison was significantly smaller than the value obtained by other researchers from neutron diffraction experiments. The g-factor and λ were found to be slightly temperature dependent. This temperature dependence is shown to indicate the presence of uniaxial anisotropy. The possible origin of this anisotropy is discussed.

to dad

ACKNOWLEDGEMENT

I here acknowledge the debt I owe to John Cochran for his constant encouragement, advice, and patience. Thanks are also due to Bretislav Heinrich and Graeme Dewar who were never unwilling to give advice.

I also thank the Natural Sciences and Engineering Council and Simon Fraser University for assigning funds which supported this work.

TABLE OF CONTENTS

Page

Page

LIST OF TABLES

LIST OF FIGURES

CHAPTER 1

INTRODUCTION

1.1 FMR and FMAR

A ferromagnet is a condensed material which has a magnetic moment even in zero applied magnetic field. This spontaneous magnetization arises because the atoms have electrons with uncompensated magnetic moments and these moments have a very strong tendency to lie parallel to one another. Ferromagnetic resonance (FMR) occurs when the ferromagnet is subjected to radiation whose frequency matches the natural frequency of precession of the spins. This natural frequency varies monotonically with the applied magnetic field; a field of a few thousand oersteds results in a precession frequency in the microwave range.

In an FMR experiment, one usually subjects the specimen to microwave radiation of a single frequency and measures the absorption as a function of the externally applied magnetic field. It is generally the aim of such an experiment to obtain information about the saturation magnetization, the electron g-factor, the magnetic anisotropy, and the magnetic damping of the specimen. This approach is fruitful for non-metallic ferromagnets. However, for metallic ferromagnets, a complicating feature is the skin effect. The skin effect causes essentially all microwave absorption to take place within approximately 1000 Å of the irradiated surface. The results of an FMR experiment are then very sensitive to the sample surface condition. Moreover, the resulting misalignment

of spins near the sample surface makes the microwave absorption function sensitive to the exchange parameter (the parameter that quantifies the tendency for neighbouring spins to remain parallel to each other) and the surface spin pinning parameter. It is fortunate, therefore, that in the case of metals, one can measure the radio frequency magnetic properties by making use of a different phenomenon, namely, the phenomenon of ferromagnetic antiresonance (FMAR).

FMAR depends upon the fact that for a particular value of the applied magnetic field (different from the field value at which FMR occurs), the transverse radio frequency (r.f.) field $\vec{h}$ inside the metal is equal in magnitude but opposite in direction to the r.f. component of the magnetization $4\pi\vec{m}$. Hence, there is no r.f. $\vec{b}$ field inside the ferromagnet to induce the dissipative eddy-currents. As a consequence, the skin depth increases dramatically (becomes infinite in the absence of magnetic damping). The result is that the transmission of microwave radiation through a metallic ferromagnet is very small (unobservable in samples thicker than $\sim 10\mu m$) except in a magnetic field interval near the FMAR field. This transmission maximum was predicted by Kaganov (1959) and was first observed in permalloy by Heinrich and Meshcheryakov (1969, 1970). The wavelengths of the waves excited in the metal at FMAR are sufficiently long that from an FMAR experiment, one can obtain information about the magnetization, the g-factor, the magnetic anisotropy, and the magnetic damping uncomplicated by effects

of exchange, pinning and the sample surface condition. It turns out that the shape of the experimental transmission curve near FMAR is so well described by the theory (developed in Chapter 2) that one can determine the saturation magnetization to within $\sim 0.1\%$ (see figure 4.11). This is significant because by means of the Bloch $T^{3/2}$ law (F. Bloch, 1930), an accurate determination of the saturation magnetization at low temperatures can be used to obtain information about the exchange parameter.

1.2 The Scope of the Thesis

This thesis contains the results of a study of the magnetic properties of the amorphous ferromagnet cobalt-phosphorus (~ 25 atomic percent phosphorus) over the temperature range 4 - 414°K. The study was motivated in large part by a desire to discover whether or not the magnetic properties of an amorphous ferromagnet differ in any essential way from those of a crystalline ferromagnet. Co-P was chosen because it is simple to prepare as a thin sheet, the form necessary for use in the microwave transmission apparatus and because its microscopic structure is simple and well understood (Cargill, 1975). The study was made using the FMAR transmission technique. The particular parameters of Co-P focussed upon in this thesis are, therefore, the magnetic damping parameter, the saturation magnetization (and, therefore, also the exchange parameter), and the magnetic anisotropy field.

Though much effort has recently been exerted by other

researchers in measuring the static magnetic properties of amorphous ferromagnets in general and Co-P in particular (see Dietz, 1977, for a good review), very little has been accomplished in the dynamic direction. The magnetic damping parameter (essentially the reciprocal of the lifetime of a spin fluctuation) can, in principle, give information about the basic types of interactions in the ferromagnetic system (Turov in Vonsovskii (1966), Chapter 6). One can see, therefore, that it is of great interest to measure the damping parameter of Co-P and its variation with temperature and to compare it with results obtained for other ferromagnets of different structures and compositions.

As stated above, a precise measurement of the magnetization as a function of temperature can yield a value for the exchange stiffness constant. One can also obtain this constant from neutron diffraction experiments. However, in some ferromagnets there has consistently been found a discrepancy of as much as 50% between the values obtained by these two methods. It was the intention of the present study to measure the exchange parameter of Co-P and to compare it with previously reported values (by both methods) for similar materials.

Amorphous ferromagnets are important from the point of view of real world applications because they are magnetically very 'soft' (they have a large permeability). This softness is connected with the fact that perfectly homogeneous and

randomly packed ferromagnets have no magneto-crystalline anisotropy. It is, therefore, of great interest to measure and, if possible, to determine the origin of any anisotropy that does exist.

1.3 The Organization of the Thesis

The remainder of this thesis is subdivided as follows. In the first part of the next chapter, the Herring and Kittel (1951) theory of spin waves is summarized. This leads to the Bloch $T^{3/2}$ law for the temperature variation of the saturation magnetization and further to the equation of motion for the magnetization. In the second part of chapter 2, the equation of motion is combined with the Maxwell equations to predict the response of a metallic ferromagnet to microwave radiation. This part of chapter 2 is based upon the work of Ament and Rado (1955), Rado and Weertman (1959), and, more recently, the work of Cochran et al. (1977a). For the convenience of the reader, an index of symbols is contained in Appendix C.

Chapter 3 is devoted to a description of the measurement and of the 24GHz microwave apparatus used to study the amorphous Co-P specimen. Chapter 4 contains the results obtained from a comparison of the experimental data with the theory of chapter 2. In the fifth chapter, the results are discussed and compared with already published data for Co-P and other ferromagnetic metals. The conclusions that could be drawn from this discussion are concisely restated in the last chapter.

CHAPTER 2

THEORY

2.1 Spin Waves in Ferromagnetic Media

Consider a single quantum mechanical spin of magnetic moment μ in free space. It is known that for spin 1/2 particles this spin can only be oriented either parallel or antiparallel to the direction of an imposed steady magnetic field H. The difference in energy between these two orientations is*

$$\Delta E = 2\mu H \tag{2.1}$$

One would, therefore, expect a single photon of exactly this energy, that is, of frequency

$$\omega = 2\mu H/\hbar \equiv \gamma H \tag{2.2}$$

to be absorbed; ie., a resonance will occur at this frequency. The constant, γ, which has here been introduced, is called the gyromagnetic ratio and is equal to

$$\gamma = 2\mu/\hbar = g\mu_B/\hbar = \left|\frac{ge}{2m_e c}\right| \tag{2.3}$$

* The reader is reminded at this point of the index of symbols in Appendix C.

μ_B is the Bohr magneton, e and m_e are the charge and mass of the electron, and c is the speed of light. The quantity g is called the Landé g-factor and is used to take into account the fact that the angular momentum and the magnetic moment of an electron in a ferromagnet do not arise solely from spin; there is a small contribution from the electron's orbital motion.

It is possible to construct a completely quantitative quantum mechanical theory of the response of a ferromagnet to microwave radiation (see, for example, Turov in Vonsovskii (1966), chapter 3). However, the absence of Planck's constant in the resonance condition (2.2) (when coupled with (2.3)) suggests that a classical theory is possible. This is indeed the case and, as such, the present chapter will be devoted to the development of a simple phenomenological classical theory whose input parameters can be measured experimentally and compared with those derived by quantum mechanical methods.

2.1.1 The Isolated Spin

In this approach, we regard each (uncompensated) electron as a classical particle with angular momentum $\vec{s}$ and magnetic moment $\vec{\mu}$. In a magnetic field $\vec{H}$ (comprised, in general, of both a static and a dynamic part), a torque

$$\vec{\tau} = \vec{\mu} \times \vec{H} \tag{2.4}$$

will act on the electron. This torque changes the angular momentum according to the usual relation

$$d\vec{s}/dt = \vec{\tau} \tag{2.5}$$

The magnetic moment associated with each spin is given by

$$\vec{\mu} = -\gamma\vec{s} \tag{2.6}$$

Combining the last three equations yields

$$d\vec{\mu}/dt = -\gamma(\vec{\mu}\times\vec{H}) \tag{2.7}$$

In order now to generalize the last equation to a collection of magnetic moments, $\vec{\mu}_i$, whose magnitudes are all the same ($|\vec{\mu}_i| = \mu$), we must take into account the interaction between individual moments. This interaction consists of two parts; one part arises from the field at a particular site caused by the other spins; the other part is what is known as the exchange interaction.

2.1.2 The Dipole-Dipole Interaction

The contribution to the magnetic field at the i^{th} spin site from all the other spins (labelled j) is called the dipole-dipole or local field. It has the form

$$\vec{H}_{Di} = \sum_{j\neq i} \vec{h}_{ji}$$

$$\text{where } \vec{h}_{ji} = \frac{-\vec{\mu}_j r_{ji}^2 + 3\vec{\mu}_j \cdot \vec{r}_{ji}\, \vec{r}_{ji}}{r_{ji}^5} \tag{2.8}$$

is the field at the i^{th} site caused by the j^{th} moment and $\vec{r}_{ji} = \vec{r}_j - \vec{r}_i$ is the position vector connecting the two sites. The present analysis considers only homogeneous single domain ferromagnets of near ellipsoidal shape. It is well known (see, for example, Brown (1962), Ch. 2 and 3) that in this case, the time-averaged dipole-dipole field is also uniform and depends only upon the particular shape of the ellipsoid through the demagnetization tensor, $\vec{\vec{N}}$, and upon the average (saturation) magnetization, $\vec{M}_s$ given by

$$\vec{M}_s = \sum_i \vec{\mu}_i / V \tag{2.9}$$

where V is the volume of the specimen. In particular, the relation is

$$\vec{H}_D = \vec{\vec{N}}\, \vec{M}_s \tag{2.10}$$

Strictly speaking, there should also be a time dependent contribution to $\vec{H}_D$ arising from the bulk non-uniformity of the magnetization because of spin fluctuations. This contribution is included in the more exact theory of Appendix A. However, none of the important features of the theory being here developed are lost if it is, for the moment, ignored.

2.1.3 The Exchange Interaction

The other part of the interaction between spins - the exchange interaction - is the reason that a spontaneous magnetization exists in ferromagnets. This interaction is quantum-mechanical in origin and can be naively understood as follows. The Pauli exclusion principle prevents two electrons of the same spin from being in the same place at the same time. Thus, electrons of parallel spin are kept far apart - farther apart than electrons of opposite spins. The Coulomb energy of electrons of parallel spin is therefore lower than the Coulomb energy of electrons having opposing spins.

One way of modelling the exchange interaction is by inserting terms proportional to $\vec{\mu}_i \cdot \vec{\mu}_j$ into the Hamiltonian of the system (the Heisenberg model). In the isotropic case and provided that spin disturbances are small enough that

$$|\vec{\mu}_i - \vec{\mu}_j| \ll \mu \quad (i,j \text{ are neighbours}) \tag{2.11}$$

one can then show (Herring and Kittel (1951)) that the effects of the exchange interaction can be taken into account by adding an exchange effective field

$$\vec{H}_{EX}(\vec{r}) = \frac{D}{2\mu^2} \nabla^2 \vec{\mu} \tag{2.12}$$

to the field acting on a given spin. D is called the spin

wave dispersion coefficient (for reasons which will become apparent), $\mu = |\vec{\mu}|$, and we have replaced $\vec{\mu}_i$ by the continuous function $\vec{\mu}(\vec{r})$ such that $\vec{\mu}_i = \vec{\mu}(\vec{r}_i)$. However, justification of the Heisenberg model especially in the case of metallic ferromagnets is still the subject of considerable theoretical interest. (See, for example, Keffer section 3 (1966) and references therein or Prange and Korenman (1979) for more recent advances). Nonetheless, Herring and Kittel (1951) have shown that (2.12) can be derived by requiring only that spin fluctuations be small (2.11) and that the exchange contribution to the Hamiltonian have the symmetry required for a medium having cubic or higher symmetry.

2.1.4 Spin Waves and the Block $T^{3/2}$ Law

Summarizing, we have the equation of motion of a system of spins in the continuum approximation:

$$\partial\vec{\mu}/\partial t = -\gamma(\vec{\mu} \times \vec{H}_{eff}) \tag{2.13}$$

where

$$\vec{H}_{eff} = \vec{H} + \vec{H}_D + \frac{D}{2\mu^2}\nabla^2\vec{\mu} \tag{2.14}$$

is the effective field acting upon $\vec{\mu}$ and as such includes the externally applied field, the demagnetization field, and the exchange effective field respectively. Using this equation, we will now determine how the magnetization of a ferromagnet

depends on temperature. For simplicity, let us consider the case where the internal field, $\vec{H} + \vec{H}_D$, is zero. The general case is presented in Appendix A. In the present case, we have simply

$$\partial\vec{\mu}/\partial t = \frac{-\gamma D}{2\mu^2} \quad (\vec{\mu} \times \nabla^2\vec{\mu}). \tag{2.15}$$

Let us assume that the spin system is very close to the ground state: the ground state having all spins aligned along the Z-direction. That is, $\vec{\mu} = (\mu_x, \mu_y, \mu_z)$ where $\mu_z \approx \mu$ and $\mu_x, \mu_y << \mu$. Using $\gamma = 2\mu/\hbar$, we get

$$\hbar \quad \partial\mu_x/\partial t = D \nabla^2\mu_y, \tag{2.16}$$

$$\hbar \quad \partial\mu_y/\partial t = -D \nabla^2\mu_x$$

Combining these two yields

$$\hbar^2 \partial^2\mu_x/\partial t^2 = -D^2\nabla^4\mu_x \tag{2.17}$$

and a similar equation for μ_y. This is essentially a wave equation and trial solutions of the form

$$\mu_x = \mu_{xo} \exp\left[i(\vec{k} \cdot \vec{r} - \omega t)\right] \tag{2.18}$$

are successful and yield the dispersion relation

$$\hbar\omega = Dk^2 \tag{2.19}$$

These types of waves are called spin waves. From a completely quantum mechanical analysis (Holstein and Primakoff (1940) or see Sparks (1964) Ch. 3 for a particularly lucid rendition of the Holstein-Primakoff transformations), one can show that these waves are quantized in the usual way. That is, the energy associated with spin waves of frequency ω is $(n_\omega + 1/2)\hbar\omega$ where n_ω is an integer. Specifically, n_ω is the number of spin wave quanta (magnons). Further, one can show that each magnon reduces the Z-component of total magnetic moment $M_S V$ by 2μ. Here, M_S is the magnetization and V is the volume of the ferromagnet. That is, if we define M_o as the magnetization of the ferromagnet in its ground state ($M_o = \mu N/V$ where N is the total number of moments), then

$$M_S V = M_o V - 2\mu n \tag{2.20}$$

where n is the total number of magnons ($= \sum_\omega n_\omega$). This result implies that with the creation of a magnon, each spin is tipped through an extremely small angle such that the total change in magnetic moment is the same as if one spin were flipped completely over. This is an aesthetically pleasing picture because it is as if in an exchange coupled spin system the eigenstates are still flipped spins but owing to the large amount of energy required to flip one spin against

exchange forces, this flip is shared among all the spins as a wave-like disturbance.

Since there is no restriction on the number of magnons of a given frequency that can be excited*, photon statistics apply and the number of magnons at a given temperature is given by

$$n = \sum_{k} \left[\exp(\hbar\omega/k_B T) - 1 \right]^{-1}$$

$$\approx \frac{V}{(2\pi)^3} \int_{k=0}^{\infty} \frac{4\pi k^2 dk}{\exp(\hbar\omega/k_B T) - 1} \qquad (2.21)$$

in the contimuum approximation. Making use of the dispersion relation (2.19), we get

$$\frac{n(T)}{V} = (2.612) \left(\frac{k_B T}{4\pi D} \right)^{3/2} \qquad (2.22)$$

Now using $2\mu = g\ \mu_B$ (2.3) and equation (2.20), we have the magnetization as a function of temperature

$$M_S(T) = M_o - (2.612) g\ \mu_B \left(\frac{k_B T}{4\pi D} \right)^{3/2} \qquad (2.23)$$

This is the $T^{3/2}$ law first derived by F. Bloch (1930).

It is worthwhile at this point to remark on the manner in which (2.23) was obtained. First of all, the only

*This is not exactly true since spin waves do interact. It is, however, true within the framework of the approximations already made.

characteristic that has been assumed for the structure of the spin system is that it is isotropic. Hence, the results should apply at least as well to amorphous ferromagnets as to crystalline materials.

Secondly, all approximations made have depended upon the 'small disturbance condition' (2.11). This condition is true for spin waves whose wavenumbers satisfy $k << 2\pi/a$, 'a' being a typical nearest neighbour distance. For thermal spin waves, $\hbar\omega \sim k_B T$. Using this information along with the dispersion relation (2.19) and also that $M_o = (1/2) g \mu_B N/V \sim (1/2) g \mu_B / a^3$, one can show that the above condition on k becomes $M_o - M_S(T) << 2\pi^{3/2} M_o$.

Third, (in stating (2.20)) we have assumed that spin waves are the only thermally excited states which change the bulk magnetization. It was shown by Stoner (1938) that the band model of itinerant ferromagnetism predicts that the magnetization should decrease as T^2. However, it has been argued theoretically by Herring and Kittel (1951) (and more recently by Korenman et al. (1977a)) that at low temperatures the so-called Stoner excitations are not important compared with the spin wave states. This conclusion has been verified experimentally by, for example, Argyle et al. (1963) for Nickel and Silicon-Iron.

2.1.5 An Equation of Motion for Any Temperature

Although we have only used the equation of motion (2.13) at low temperatures, a simple renormalization (Keffer and

Loudon (1961)) enables us to apply it at all temperatures. As the temperature increases and more spin waves are excited, the average angle between each spin and the direction of bulk magnetization gradually increases causing M(T) to drop. The system at temperature T, then, resembles a completely aligned array of spins each of moment $\mu M(T)/M_o$ rather than μ. Hence, the renormalized equation of motion is

$$\partial\vec{M}/\partial t = -\gamma(\vec{M} \times \vec{H}_{eff}) \tag{2.24}$$

Here $\vec{M}$ is the local magnetization vector. Specifically, $\vec{M}$ is the magnetic moment per unit volume averaged over a volume which is at the same time much larger than a^3 but very much smaller than the cube of any length in which we are interested. For the work reported here, $\vec{M}$ is well-defined because the smallest macroscopic length of interest is the skin depth $\sim 10^3$ Å. In terms of $\vec{M}$, $\vec{H}_{eff}$ is now

$$\vec{H}_{eff} = \vec{H} + \vec{H}_D + \left(2A/M_S^2\right)\nabla^2\vec{M} \tag{2.25}$$

where A is called the exchange stiffness parameter.

$$A = \frac{M_S D}{4\mu} = \frac{M_S D}{2g\ \mu_B} \tag{2.26}$$

2.1.6 The Damping Term

Magnetic disturbances in real ferromagnets have finite

lifetimes due to the interactions of spins with the surrounding medium. Phenomenologically, we can take this into account by adding a damping term to the equation of motion (2.24). Three forms of this damping term are in common use:

$$\left.\frac{\partial \vec{M}}{\partial t}\right|_{\text{damping}} = \begin{cases} \dfrac{-\lambda}{M_s^2}\ \vec{M} \times (\vec{M} \times \vec{H}_{\text{eff}}) & (2.27) \\ \dfrac{G}{\gamma M_s^2}\ (\vec{M} \times \partial\vec{M}/\partial t) & (2.28) \\ -\dfrac{\vec{M}_T}{\tau_1} \quad -\dfrac{\vec{M}_L - \vec{M}_S}{\tau_2} & (2.29) \end{cases}$$

$\vec{M}_L$ is the vector component of $\vec{M}$ in the direction of $\vec{M}_S$ and $\vec{M}_T = \vec{M} - \vec{M}_L$; λ, G, and $1/\tau_1$ and $1/\tau_2$ are appropriate relaxation frequencies.

The first form (2.27) is due to Landau and Lifshitz (1935). When this term is added to the right-hand side of the equation of motion (2.24), we see that the expression for $\partial\vec{M}/\partial t$ consists only of terms proportional to the cross product of $\vec{M}$ with other vectors. It is clear, therefore, that $\partial\vec{M}/\partial t$ is perpendicular to $\vec{M}$. In other words, $\vec{M} \cdot \partial\vec{M}/\partial t = 0$, or, M^2 = constant. Physically, this means that in the case of Landau-Lifshitz damping, $\vec{M}$ fluctuates about its equilibrium value ($\vec{M}_S$) without changing its magnitude.

The Landau-Lifshitz term (2.27) can be written in a simpler form but first a few definitions are necessary. Let $\vec{m}$ be the time dependent component of $\vec{M}$; that is, $\vec{M} = \vec{M}_S + \vec{m}$. If $m << M_S$ then to a first approximation, $\vec{m}$ is perpendicular to $\vec{M}_S$.

Further, let $\vec{h}$ be the time dependent part of $\vec{H}_{eff}$ and let $\vec{H}_N$ be the static part, i.e., $\vec{H}_{eff} = \vec{H}_N + \vec{h}$. Also, let us divide $\vec{h}$ into a vector along $\vec{H}_N$ ($\vec{h}_{||}$) and a vector perpendicular to $\vec{H}_N$ ($h_\perp$). We know intuitively (and it is clear from the equation of motion (2.24)) that $\vec{M}_S$ is parallel to $\vec{H}_N$. Using the above information along with the vector identity $\vec{a} \times (\vec{b} \times \vec{c}) = (\vec{a} \cdot\cdot \vec{c})\vec{b} - (\vec{a} \cdot\cdot \vec{b})\vec{c}$, we can rewrite (2.27) to first order as

$$\partial M/\partial t\Big|_{LL} = - \lambda\left[(H_N/M_S)\vec{m} - \vec{h}_\perp\right] \qquad (2.30)$$

The second damping form (2.28) was proposed by Gilbert (1955) and can be seen to be the same as the Landau-Lifshitz form in the limit $\gamma M_S >> G$. Inspection of the equation of motion of $\vec{M}$ with the Gilbert form of the damping term will convince one that also with this form, $\vec{M} \cdot\cdot \partial\vec{M}/\partial t = 0$; that is, $M = M_S$ = constant. If we write down the complete equation of motion with the Gilbert damping term as

$$\partial\vec{M}/\partial t = - \gamma_G(\vec{M} \times \vec{H}_{eff}) + \frac{G}{\gamma_G M_S^2}(\vec{M} \times \partial\vec{M}/\partial t) \qquad (2.31)$$

and multiply it vectorially by $\vec{M}$ (keeping in mind that $\vec{M} \cdot \partial\vec{M}/\partial t = 0$), we get

$$\vec{M} \times \partial\vec{M}/\partial t = -\gamma_G \vec{M} \times (\vec{M} \times \vec{H}_{eff}) - \left(G/\gamma_G\right)\partial\vec{M}/\partial t \qquad (2.32)$$

Now we can substitute this back into (2.31) and get

$$\left[1+\left(\frac{G}{\gamma_G M_s}\right)^2\right]\frac{\partial \vec{M}}{\partial t} = \gamma_G\left(\vec{M}\times\vec{H}_{eff}\right) - \frac{G}{M_s^2}\vec{M}\times\left(\vec{M}\times\vec{H}_{eff}\right) \quad (2.33)$$

Hence, (2.27) and (2.28) are formally identical and one can make the identification

$$\gamma_{LL} = \frac{\gamma_G}{1+\left(\frac{G}{\gamma_G M_s}\right)^2} \quad , \quad \lambda = \frac{G}{1+\left(\frac{G}{\gamma_G M_s}\right)^2} \quad (2.34)$$

The third form of the damping term (2.29) was introduced by F. Bloch for nuclear magnetic relaxation and adapted by Bloembergen (1950) to ferromagnetic relaxation. The rationale behind splitting the relaxation process into separate transverse and longitudinal processes is nicely explained in Sparks (1964), Ch. 2. In the present application since we will only be considering disturbances for which M_T ($\approx m$) $<<$ M_S (and hence $M_L - M_S$ is second order), we will use the simpler form

$$\left.\frac{\partial \vec{M}}{\partial t}\right|_{BB} = -\frac{\vec{m}}{\tau_1} \quad (2.35)$$

Where the Landau-Lifshitz and the Bloch-Bloembergen damping forms seem better suited to the idea of finite-lifetime spin-wave quanta, the Gilbert form appeals to our classical intuition because in this case the damping is proportional to $\partial\vec{M}/\partial t$ and hence is like the effect of a viscous medium on

$\vec{M}$. These ideas are borne out by the following analysis. Neglecting the time dependence of $\vec{H}_{eff}$ and assuming that $m << M_S$, all three forms of the equation of motion can be solved by

$$\vec{m} = \vec{m}_0 \, e^{-t/\tau_0} \, e^{i\omega t} \tag{2.36}$$

The parameters ω and τ_o obtained in this way are listed in table 2.1 Note in particular that a magnetic disturbance has

Table 2.1 - Transient response parameters ω and τ_o obtained for the magnetization when the Landau-Lifshitz, the Gilbert, or the Bloch-Bloembergen form of the damping term is used in the equation of motion.

Damping Type	τ_o	ω
Landau-Lifshitz	$\frac{M_s}{\lambda H_N}$	γH_N
Gilbert	$\frac{M_s}{G H_N}\left[1+\left(\frac{G}{\gamma M_s}\right)^2\right]$	$\gamma H_N\left[1+\left(\frac{G}{\gamma M_s}\right)^2\right]^{-1}$
Bloch-Bloembergen	τ_1	γH_N

an infinite lifetime if the Gilbert damping parameter, G, is either very large or very small. This is exactly what one would expect for a gyroscope in a classical viscous medium.

There is one further damping mechanism in metals;

namely, eddy-current damping. This damping arises because a time dependent magnetization implies a time dependent $\vec{b}$-field which through Faraday's law generates an electric field $\vec{e}(t)$ and the resulting current density causes joule heating losses because of the finite conductivity. This damping mechanism is self-consistently taken into account when we combine the equation of motion for $\vec{M}$ with the Maxwell equations and the constitutive relation which is Ohm's law. It is shown in Appendix A that eddy-current damping has only a negligible effect on thermal spin waves. The central problem here, however, is to calculate the response of a metallic ferromagnet to microwave radiation of a given frequency (forced oscillations). In this case, the metallic electrical conductivity becomes very important as we shall see.

2.2 The Response of a Ferromagnet to Microwave Radiation

2.2.1 The General Boundary Value Problem

We wish to solve the problem outlined in Fig. 2.1. Microwaves of known amplitude, frequency, and polarization impinge normally upon the surface of a prolate ellipsoid whose aspect ratio is much larger than unity. An external magnetic field (of sufficient strength to ensure that the ellipsoid is a single domain) is applied either parallel (parallel configuration) or perpendicular (perpendicular configuration) to the sample plane. We wish to calculate the amplitude and phase of both the transmitted and reflected microwave radiation. Initially, we shall restrict ourselves

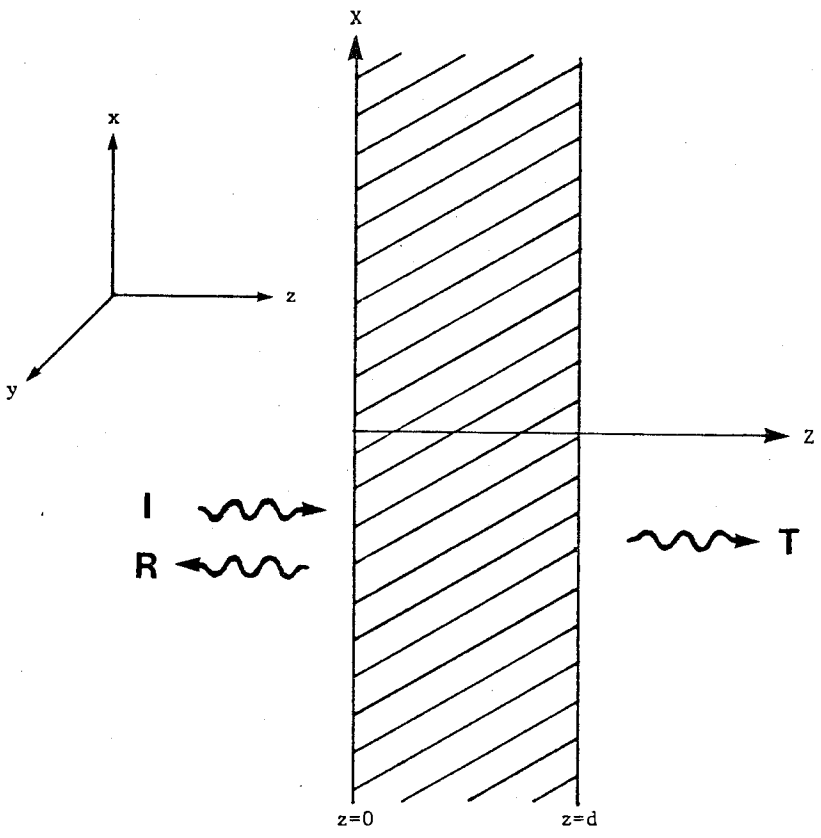

Fig. 2.1

Schematic diagram of the waves involved in the boundary value problem. The ferromagnet, in the shape of a thin circular disc, lies in the xy-plane between z=0 and d. Microwaves (I) are incident from z = $-\infty$. In steady state, a certain percentage (R) of these microwaves is reflected from the specimen and a certain percentage (T) is transmitted through the specimen.

to the Gilbert form of the damping term. Later, we can use relations (2.30), (2.34) and (2.35) to generalize the results. We can write the equation of motion of $\vec{M}$ in the form

$$-\frac{1}{\gamma}\frac{\partial \vec{M}}{\partial t} = \vec{M} \times \left(\vec{H}_{eff} - \frac{G}{\gamma^2 M_s^2} \frac{\partial \vec{M}}{\partial t} \right) \qquad (2.37)$$

$\vec{H}_{eff}$ is again given by (2.25) but we will now split $\vec{H}$ into the static applied field $\vec{H}_o$ and a dynamic field $\vec{h}$. Also, $\vec{M}$ is

assumed to have the form

$$\vec{M} = \vec{m} + \vec{M}_S \tag{2.38}$$

where $\vec{M}_S$, being the equilibrium magnetization inside an ellipsoid, depends neither on position nor on time and $\vec{m}$ is perpendicular to it. (In general, $\vec{m}$ has a component along $\vec{M}_S$. It is, however, second order and will be neglected. It is for this same reason that throughout this thesis, the magnitudes M and M_S are used more or less interchangeably.) The vector $\vec{M}_S$ is, of course, parallel to the static internal field, $\vec{H}_N = \vec{H}_o + \vec{H}_D$. Both $\vec{h}$ and $\vec{m}$ are assumed to vary in space and time as $e^{i(kz - \omega t)}$; ω being the frequency of the incident microwave radiation. I have assumed that the wavevector $\vec{k}$ of the waves excited by the microwaves will be in the z-direction (i.e. parallel to the specimen normal, see Fig. 2.1). This is a reasonable assumption, for, it will turn out that $2\pi/k$ is, at the very most, a few tens of microns while $2\pi c/\omega$ is of the order of 1 cm. Hence, even if the microwaves impinge upon the sample at a slightly oblique angle, these waves are strongly refracted into the direction of the specimen normal. With these considerations, (2.37) becomes

$$i\frac{\omega}{\gamma}\vec{m} = \vec{m} \times \left[\vec{H}_N + \left(\frac{2Ak^2}{M_s^2} - \frac{i}{M_s^2}\frac{G}{\gamma}\frac{\omega}{\gamma}\right)\vec{M}_s\right] - \vec{h} \times \vec{M}_s \tag{2.39}$$

In translating (2.37) into (2.39), terms of second order have been neglected. By this I mean that terms proportional

to h^2, hm, or m^2 have been neglected compared with those proportional to eg., hM or mH. This approximation is permissible because experimentally, in our case m/M at FMAR never exceeded 10^{-5} and it can be shown that at FMR, this ratio is only a factor of $\frac{\omega}{4\pi G} \sim 10^2$ larger.

Starting with Maxwell's equations (A.1 of Appendix A), one can find a second relation between $\vec{h}$ and $\vec{m}$ (A.2). Applying the fact that $\vec{k}$ is in the z-direction to this relation yields

$$\vec{h} = -\frac{4\pi}{1+ik^2\delta^2}\left(\vec{m} + i\delta^2 k^2 m_z \hat{z}\right) \qquad (2.40)$$

where $\hat{z}$ is the unit vector in the z-direction, and I have introduced the scaling length (related to the classical skin depth)

$$\delta = \left(\frac{c^2}{4\pi\omega\sigma}\right)^{\frac{1}{2}}$$

σ being the electrical conductivity. In order to avoid confusion, I remind the reader at this point that in Appendix A, ω was the frequency of any (thermally excited or otherwise) spin fluctuation; while in the present case, we are looking for spin fluctuations excited by the incident microwave radiation and as such, ω is fixed and well-defined. Here, we can neglect the imaginary (dielectric) term in the conductivity because $\omega \sim 10^{11}\ \text{sec}^{-1}$ for microwaves and $4\pi\sigma$ is no less than

$\sim 10^{17}\ \text{sec}^{-1}$; that is, the condition $4\pi\sigma >> \varepsilon\omega$ is easily satisfied.

Substituting (2.40) into (2.39) yields a homogeneous system of equations in the two components of $\vec{m}$ perpendicular to $\vec{M}_S$. The condition for non-zero $\vec{m}$ is that the determinant of the coefficients be zero. This gives rise to an equation that is quartic in k^2. (Actually, this is the dispersion relation for waves travelling in the z-direction.) Hence, for a fixed pumping frequency ω, we have 8 waves in the ferromagnet. Of these 8, 4 propogate in the +z-direction and 4 in the -z - direction. Of these 4, there are 2 of each polarization. Far from FMR, one can identify one of these groups as electromagnetic waves with skin effect properties, ie. damped electromagnetic waves; the other group of 4 waves can be identified as spin waves. Near FMR, one cannot make this distinction as all waves are mixtures of electromagnetic and spin waves. The complete boundary value problem including the two reflected waves (one of each polarization) and the two waves transmitted through the sample, comprises a total of 12 waves whose amplitudes are to be found. Thus, we need 12 boundary conditions; 6 at each surface of the disc. Continuity of $\vec{h}$ and $\vec{e}$ supplies us with 4 of these 6. The remaining two come from the boundary conditions on $\vec{m}$.

Experimental results in general indicate that the surface spins are intermediate between being pinned ($\vec{m} = 0$) and unpinned ($\partial\vec{m}/\partial z = 0$). (See Bailey and Vittoria (1972, 1973) or

Heinrich et al. (1977).) That is, one can interpret experimental results on the basis of a formula (first suggested by Rado and Weertman (1959)) of the form

$$\vec{m}\Big|_{z=0,d} + b_p \frac{\partial \vec{m}}{\partial z}\Big|_{z=0,d} = 0 \qquad (2.42)$$

where b_p is left as an adjustable parameter. With all the necessary boundary conditions, we now have 12 equations in 12 unknowns. Solution of this system is straight-forward using a digital computer.

2.2.2 The Perpendicular Configuration

While the above procedure is a good one for finding the general solutions to the boundary value problem, it is not very enlightening to the reader. For this reason, let us consider the special case of perpendicular configuration ($\vec{H}_o$ and $\vec{M}_S$ orthogonal to the plane of the disc). In this case, $\vec{m}$ lies in the plane of the sample and, by (2.40) (ie. by Maxwell's equations), so also does $\vec{h}$ have only transverse components. Then defining χ_{RF} by $\vec{m} = \chi_{RF}\vec{h}$, we have

$$\chi_{RF} = -\frac{1}{4\pi}\ (1 + ik^2\delta^2) \qquad (2.43)$$

Equation (2.39) can now be written

$$\begin{pmatrix} m_x \\ m_y \end{pmatrix} = \frac{M_S}{H_F^2 - (\omega/\gamma)^2}\begin{pmatrix} H_F & -i\frac{\omega}{\gamma} \\ i\frac{\omega}{\gamma} & H_F \end{pmatrix}\begin{pmatrix} h_x \\ h_y \end{pmatrix} \qquad (2.44)$$

(where $H_F \equiv H_N + \frac{2A}{M_s} k^2 - \frac{i}{M_s} \frac{G}{\gamma} \frac{\omega}{\gamma}$) thus defining a susceptibility tensor. This tensor can be diagonalized by going to the circular polarization representation $m_{\pm} = m_x \pm i m_y$ and $h_{\pm} = h_x \pm i h_y$. In that case, (2.44) can be written

$$\chi_{RF\pm} = \frac{M_S}{H_F \pm \omega/\gamma} \tag{2.45}$$

2.2.2a Ferromagnetic Resonance

Ignoring exchange and damping, (2.45) means that in the case of the lower sign, and with $H_N = \omega/\gamma$, a finite $\vec{m}$ is possible with $\vec{h} = 0$. The interpretation of this is simply that the natural frequency of precession of the spin system is γH_N and the natural polarization is that corresponding to the lower sign. Hence, microwaves of frequency $\omega = \gamma H_N$, when allowed to impinge upon the system are heavily absorbed. This is called ferromagnetic resonance (FMR). Practically, a fixed microwave frequency is used and H_N is varied. A maximum in absorption (or a minimum in reflection or transmission) is observed when the condition $H_N = \omega/\gamma$ is met. In this way, one can determine γ and hence the g-factor of the spins.

Magnetic damping contributes an imaginary part of $\frac{1}{M_S} \frac{G}{\gamma} \frac{\omega}{\gamma}$ to H_F. The presence of this term prevents χ_{RF-} from becoming singular at $H_N = \omega/\gamma$ and furthermore causes the absorption peak to have a finite width. This width is $\Delta H \sim \frac{1}{M_S} \frac{G}{\gamma} \frac{\omega}{\gamma}$ or $\Delta H/H_N \sim G/(\gamma M_S)$. Typically, for a metal, $G \sim 10^8 \text{sec}^{-1}$, $\gamma \approx 1.8 \times 10^7 \text{oe}^{-1}\text{sec}^{-1}$, and $M_S \lesssim 10^3$gauss.

Therefore, the fractional width is $\Delta H/H_N \gtrsim 10^{-2}$, or, at a frequency of $\omega/2\pi = 24$ GHz, $\omega/\gamma \approx 8000$ oe so that $\Delta H \gtrsim 100$ oe. If it weren't for the exchange contribution to H_F, one could determine the damping parameter by measuring the width of the absorption lineshape. The problem is that this contribution ($2Ak^2/M_S$) has a significant imaginary part at FMR and therefore contributes to the FMR absorption peak width. This can be shown by equating (2.43) and (2.45) for the lower sign case to find k^2 from the secular equation. At $H_N = \omega/\gamma$ and neglecting damping for simplicity, this equation is

$$H_E \delta^4 k^4 - i H_E \delta^2 k^2 - i 4\pi M_S = 0 \qquad (2.46)$$

where we have defined $H_E = 2A/(M_S \delta^2)$. For the case $4\pi M_S >> H_E$ (typically, at microwave frequencies, $H_E \lesssim 1$ oe), this yields

$$k^2 \approx \frac{i^{1/2}}{\delta^2}\left(\frac{4\pi M_S}{H_E}\right)^{1/2} \qquad (2.47)$$

and the exchange contribution to the FMR absorption linewidth is therefore

$$\Delta H_{ex} \lesssim \left| Im\left(\frac{2Ak^2}{M_S}\right)\right| \approx \frac{(4\pi A)^{1/2}}{\delta} \qquad (2.48)$$

For a typical ferromagnet, $A \sim 10^{-6}$ erg/cm and $\delta \sim 10^{-4}$ cm in the microwave region. Hence, ΔH_{ex} can be as large as ~ 50 oe; that is, comparable to the damping contribution to the FMR

absorption linewidth. Furthermore, if one solves the complete boundary value problem, one discovers that the exchange contribution to the FMR linewidth depends heavily upon the value of the pinning parameter b_p in (2.42). In general, therefore, the FMR absorption lineshape depends upon all three parameters; damping, exchange, and pinning.

As a tool for measuring ferromagnetic parameters, FMR has another disadvantage. Equation (2.47) implies that the damping length of the waves in the ferromagnet at FMR is

$$\frac{1}{Im(k)} \sim \left(\frac{H_E}{4\pi M_s}\right)^{1/4} \delta \qquad (2.49)$$

Using $4\pi M_s \sim 10^3$ to 10^4 gauss, $A \sim 10^{-6}$ erg/cm, and $\delta \sim 10^{-4}$ cm, we find $H_E \lesssim 1$ oe (thus justifying the approximation used to derive (2.47)) and hence, the damping length is of the order of 1000 Å. This means that most of the FMR absorption takes place within 1000 Å of the irradiated surface and hence FMR absorption measurements are very dependent upon sample surface quality.

2.2.2b Ferromagnetic Antiresonance

There is another special value of H_N associated with the susceptibility given in (2.45). This will be more obvious if we define a radio frequency permeability by $\vec{b} = \mu_{RF}\vec{h}$ ($\vec{b}$ is of course the r.f. magnetic induction). Then

$$\mu_{RF\pm} = 1 + 4\pi\chi_{RF\pm} = \frac{H_F \pm \omega/\gamma + 4\pi M_s}{H_F \pm \omega/\gamma} \qquad (2.50)$$

We see that in the absence of magnetic damping and effects of

exchange, $\mu_{RF-} = 0$ when $H_N = \omega/\gamma - 4\pi M_S$, or, $B_N = \omega/\gamma$. But $\mu_{RF} = 0$ implies that there is no r.f. $\vec{b}$-field to generate an r.f. electric field and hence no eddy-current damping. The result is that we have an infinite skin depth and the ferromagnet becomes transparent. Another way of understanding this is by writing (2.43) in terms of μ_{RF}:

$$\mu_{RF} = -ik^2\delta^2 \tag{2.51}$$

Thus, $\mu_{RF} = 0$ implies $k = 0$ and hence an infinite damping length. This is known as the phenomenon of ferromagnetic antiresonance (FMAR); it can be observed by monitoring the amplitude of the microwaves transmitted through the ferromagnet while varying the applied magnetic field. The existence of finite magnetic damping prevents μ_{RF-} from becoming exactly zero. and, just as with FMR, the effect is smeared out and a width of $\sim H_L \equiv \frac{1}{M_S}\frac{G}{\gamma}\frac{\omega}{\gamma}$ is imparted to the transmission amplitude peak. By equating (2.50) to (2.51) for the case of μ_{RF-} and $H_N = \omega/\gamma - 4\pi M_S$ and assuming $H_E << H_L << 4\pi M_S$, we find approximately

$$H_E \delta^4 k^4 - 4\pi M_s \delta^2 k^2 - H_L = 0 \tag{2.52}$$

The solutions to this secular equation are

$$\delta^2 k_{sw}^2 \approx \frac{4\pi M_s}{H_E} \sim 10^4 \tag{2.53a}$$

$$\delta^2 k_{em}^2 \approx \frac{-H_L}{4\pi M_s} \sim -10^{-2} \qquad (2.53b)$$

where the subscripts sw and em refer to spin wave and electromagnetic wave respectively. By solving the complete boundary value problem, one can show that the ratio of the amplitude (in $\vec{h}$) of the spin wave to that of the electromagnetic wave is the largest for fully pinned surface spins and even then is only $\frac{1}{\delta^2 k_{sw}^2} \sim 10^{-4}$. Therefore, the spin waves at FMAR can be neglected. Hence, for the important waves, the exchange contribution to H_F is $H_E \delta^2 k^2 \sim -10^{-3}$oe. This is absolutely negligible when compared with either $H_N - \omega/\gamma$ or H_L. From the above argument we can conclude not only that the value of A is unimportant but also that the pinning parameter is unimportant. The latter conclusion can be seen by an existence theorem: if we deny the existence of two of the waves in the ferromagnet, we need two fewer boundary conditions.

From (2.53), we can see that the damping length is $\sim\sqrt{\frac{4\pi M_S}{H_L}}\,\delta \sim 10\delta$. That is since $H_L = \frac{G}{\gamma M_S}\frac{\omega}{\gamma}$, the amplitude of the radiation transmitted through the specimen at FMAR contains the factor

$$\exp[Im(k)d] = \exp\left[\frac{-\omega/\gamma}{4\pi M_s}\left(\frac{2G}{\omega/2\pi}\right)^{1/2}\frac{d}{\delta}\right] \qquad (2.54)$$

In a non-magnetic metal of thickness d, radiation is attenuated by a factor of $\exp\left(\frac{-d}{\sqrt{2}\,\delta}\right)$. For $d/\delta \approx 50$ (ie. $d \approx 50\mu m$ when

$\delta \approx 1\mu m$; the skin depth of a typical metal at $\omega/2\pi = 24$ GHz), this factor is 10^{-15} corresponding to a transmitted power of less than 10^{-30} times the incident power. For an incident power of 1 watt, this results in an unobservably small transmitted signal. (The minimum detectable signal at room temperature using a 1 Hz bandwidth is $\sim 4 \times 10^{-21}$ watts. This corresponds to the thermal noise in a 1 Hz bandwidth. For a typical ferromagnet at FMAR, the attenuation factor is much larger: (2.54) becomes $\sim \exp \frac{-d}{10\delta} \sim 10^{-2}$. For 1 watt of incident power, this would give a transmitted power of $\sim 10^{-4}$ watts*. Hence, in this 'thick limit' we expect the phenomenon of FMAR to be readily observable. Furthermore, we expect it to depend strongly on both the damping parameter and the resistivity (through δ) but not on the exchange or the pinning parameter.

2.2.3 Other Configurations

So far, we have considered only the case of perpendicular configuration. In order that the reader may be convinced that the FMR and FMAR phenomena exist for other, less symmetric geometries, the case of general geometry will now be treated. For simplicity, we neglect both damping and exchange.

---

*Actually, besides (2.54), the transmission function also contains a factor $4(\omega/c)\, k\, \delta^2$ arising from the impedance mismatch between the vacuum and the metal. For our case, this factor is $\sim 10^{-3}$ yielding a maximum transmission of $\sim 10^{-10}$ watts - still readily observable.

Conditions on the external field, H_o, necessary for the appearance of these two phenomena will also be derived.

We will start with the equation of motion (2.39) for the case A = G = 0:

$$i\left(\omega/\gamma\right)\vec{m} = \vec{m} \times \vec{H}_N - \vec{h} \times \vec{M}_S \tag{2.55}$$

In matrix form, this equation is

$$\begin{pmatrix} i\omega/\gamma & -H_{Nz} & H_{Ny} \\ H_{Nz} & i\omega/\gamma & -H_{Nx} \\ -H_{Ny} & H_{Nx} & i\omega/\gamma \end{pmatrix} \begin{pmatrix} m_x \\ m_y \\ m_z \end{pmatrix} = \begin{pmatrix} M_{Sy}h_z - M_{Sz}h_y \\ M_{Sz}h_x - M_{Sx}h_z \\ M_{Sx}h_y - M_{Sy}h_x \end{pmatrix} \tag{2.56}$$

We will assume (see Fig. 2.1) that the waves in which we are interested travel in the z-direction. In that case, the Maxwell equation div $\vec{b} = 0$ implies that $h_z = -4\pi m_z$ and, with this substitution, the matrix equation (2.56) becomes

$$\begin{pmatrix} i\omega/\gamma & -H_{Nz} & B_{Ny} \\ H_{Nz} & i\omega/\gamma & -B_{Nx} \\ -H_{Ny} & H_{Nx} & i\omega/\gamma \end{pmatrix} \begin{pmatrix} m_x \\ m_y \\ m_z \end{pmatrix} = \begin{pmatrix} -M_{Sz}h_y \\ M_{Sz}h_x \\ M_{Sx}h_y - M_{Sy}h_x \end{pmatrix} \tag{2.57}$$

where, as before, $\vec{B}_N \equiv \vec{H}_N + 4\pi\vec{M}_S$; and $\vec{H}_N = \vec{H}_o + \vec{H}_D$ is the internal field. At FMR, $\vec{m}$ is finite while $h_x = h_y = 0$. This means that the determinant of the matrix must be zero; that is,

$$-i\left(\frac{\omega}{\gamma}\right)^3-\left(H_{Ny}B_{Nx}-H_{Nx}B_{Ny}\right)H_{Nz}+i\frac{\omega}{\gamma}\left(H_{Nx}B_{Nx}+H_{Ny}B_{Ny}+H_{Nz}^2\right)=0 \qquad (2.58)$$

But $\vec{H}_N$ and $\vec{M}_S$ are parallel. Hence, $\vec{H}_N$ is parallel to $\vec{B}_N$ and the middle term in (2.58) disappears. We are left with

$$\left(\frac{\omega}{\gamma}\right)^2=H_{Nx}B_{Nx}+H_{Ny}B_{Ny}+H_{Nz}^2=H_N\left(H_N+4\pi M_S\sin^2\theta\right) \qquad (2.59)$$

where θ is the angle between $\vec{M}_S$ and the z-axis. (Note that this is consistent with (A.6) of Appendix A). For the perpendicular configuration $\theta = 0$ and we regain the previously derived FMR condition $H_N = \omega/\gamma$. For the parallel configuration we get $(\omega/\gamma)^2 = H_N B_N$. It is, of course, more useful to express these conditions in terms of the externally applied magnetic field, $\vec{H}_o$. This can be done using (2.10):

$$\vec{H}_N = \vec{H}_o - \vec{\vec{N}}\,\vec{M}_S \qquad (2.60)$$

For a disc oriented as in Fig. 2.1, $\vec{\vec{N}}$ is diagonal with $N_x = N_y << 1$ and $N_z \approx 4\pi$. Thus, the conditions for FMR are

$$\perp \text{FMR:} \quad \omega/\gamma = H_o - N_z M_S \approx H_o - 4\pi M_S \qquad (2.61)$$

$$\parallel \text{FMR:} \quad \left(\omega/\gamma\right)^2=\left(H_o-N_xM_S\right)\left[H_o+\left(4\pi-N_x\right)M_S\right] \approx H_o\left(H_o+4\pi M_S\right) \qquad (2.62)$$

Using $\vec{b} = \vec{h} + 4\pi\vec{m}$, the matrix equation (2.57) can be rewritten:

$$\begin{pmatrix} i\omega/\gamma & -B_{Nz} & B_{Ny} \\ B_{Nz} & i\omega/\gamma & -B_{Nx} \\ -B_{Ny} & B_{Nx} & i\omega/\gamma \end{pmatrix} \begin{pmatrix} m_x \\ m_y \\ m_z \end{pmatrix} = \begin{pmatrix} -M_{Sz} b_y \\ M_{Sz} b_x \\ M_{Sx} b_y - M_{Sy} b_x \end{pmatrix} \qquad (2.63)$$

At FMAR, $\vec{m}$ is finite while $\vec{b}$ is zero. So, setting the determinant of the matrix in (2.63) to zero and simplifying, we get the FMAR condition

$$\omega/\gamma = B_N \qquad (2.64)$$

Hence we see that the FMAR condition on the internal field is independent of orientation. In terms of the externally applied field, we have

$$\perp \text{FMAR:} \quad \frac{\omega}{\gamma} = H_o + (4\pi - N_z)M_S \approx H_o \qquad (2.65)$$

$$\parallel \text{FMAR:} \quad \frac{\omega}{\gamma} = H_o + (4\pi - N_x)M_S \approx H_o + 4\pi M_S \qquad (2.66)$$

2.2.4 Magnetic Anisotropy

Throughout the theory developed above, it has been assumed

that the internal energy of our ferromagnet is independent of the direction of the spontaneous magnetization. In general, however, crystalline ferromagnets exhibit magnetic anisotropy which can be described by anisotropy fields as large as a few thousand oersteds. This anisotropy is not surprising in view of the non-spherical symmetry of the typical crystal structure. An amorphous ferromagnet cannot, of course, exhibit any magnetic anisotropy unless the randomness of its structure is spoiled by some kind of inhomogeneity.

The most reasonable (and simplest) type of anisotropy which one can assume for an amorphous ferromagnet which has been prepared in the form of a sheet is uniaxial anisotropy with axis parallel to the sheet normal. If we define θ as the angle between the sample normal and the magnetization $\vec{M}$, then E_A, the anisotropy energy per unit volume, is given by

$$E_A = K \sin^2\theta \tag{2.67}$$

where K is called the anisotropy constant. Using the coordinate system of Fig. 2.1, one can show that the effect of this energy can be expressed as a torque $\vec{\tau}_A$ which tends to align the magnetization along the anisotropy axis. This torque is given by:

$$\vec{\tau}_A = H_A\left(M_z/M_S\right)(M_y, -M_x, 0) \tag{2.68}$$

where we have defined an 'anisotropy field' $H_A \equiv 2K/M_S$.

In the perpendicular configuration, $\vec{M}$ can be written as (m_x, m_y, M_S) and hence the anisotropy torque is simply

$$\vec{\tau}_A = \vec{M} \times \vec{H}_A \tag{2.69}$$

if $\vec{H}_A$ is taken as being in the z-direction. By adding (2.69) to the right side of the equation of motion (2.37), it is clear that the anisotropy can be completely taken into account by adding H_A to the applied field. Hence, in the presence of uniaxial anisotropy, conditions (2.61) and (2.65) for the occurrence of FMR and FMAR become (for the case of an infinite disc)

$$\perp \text{ FMR:} \quad \omega/\gamma = H_o + H_A - 4\pi M_S \tag{2.70}$$

$$\perp \text{ FMAR:} \quad \omega/\gamma = H_o + H_A \tag{2.71}$$

For an infinite disc in the parallel configuration, $\vec{M}$ is (M_S, m_y, m_z) and so to first order in small quantities, (2.68) becomes

$$\vec{\tau}_A = -H_A \, m_z \, \hat{y} \tag{2.72}$$

When this is appended to the right side of the equation of motion (2.55), we find that (2.62) and (2.66) become

$$\| \text{FMR:} \quad (\omega/\gamma)^2 = H_o(H_o + 4\pi M_S - H_A) \tag{2.73}$$

$$\| \text{FMAR:} \quad (\omega/\gamma)^2 = (H_o + 4\pi M_S)(H_o + 4\pi M_S - H_A) \tag{2.74a}$$

$$\text{or} \qquad \omega/\gamma \approx H_o + 4\pi M_S - 1/2\ H_A \tag{2.74b}$$

for the case where the anisotropy field, $H_A = \frac{2K}{M_S}$ is much smaller than $H_o + 4\pi M_S$.

CHAPTER 3

EXPERIMENT

3.1 Sample Preparation and Characterization

Amorphous cobalt-phosphorus (Co-P) with approximately 25 atomic percent phosphorus was obtained from G.C. Chi* in the form of a 4 cm × 4 cm × ~100μm thick sheet plated on a 250μm thick sheet of copper. This specimen had been prepared using the original method developed by Brenner et al. (1950). A solution containing specified amounts of $CoCl_2$, $CoCO_3$, H_3PO_4, and H_3PO_3 dissolved in water is heated to 75°C, electrodes are inserted, and when a current is passed through the solution, Co-P begins to plate onto the cathode. The phosphorus concentration in the Co-P can be changed by changing the ratios of the concentrations of the various constituents of the electrolyte. The particular recipe used by Chi in preparing the specimen upon which the experiments were performed was: H_3PO_3, 95 g/l; $CoCO_3$, 50.6 g/l; $CoCl_2 \cdot 6H_2O$, 139.3 g/l; H_3PO_4, 50 g/l (= 35 ml/l of 85% solution). The current density he used was 100 mA/cm^2. In order to ensure a uniform phosphorus throughout the resulting Co-P, Chi used an electrodepositting apparatus which consisted of a large electrolyte reservoir connected to a small plating cell (Chi (1977)). An acid-proof pump forced electrolyte to flow past the two electrodes in the cell at a constant speed

*Present address: Bell Laboratories, Murray Hill, N.J. 07974, U.S.A.

while a thermistor connected to a feedback mechanism controlled a heater in the reservoir and in this way ensured that the electrolyte temperature did not vary.

The end product, though shiny, was not smooth. In particular, it had an uneven, pitted appearance. Surface irregularities were of the order of $3mm^2$ in area by ~10μm deep although in extreme cases, the pits went completely through the sample thickness. The copper substrate was dissolved away in an aqueous solution which contained 500 g of CrO_3 and 50 g of H_2SO_4 per liter of solution at 70°C. A 6 mm diameter disc was then spark-cut from the centre of the sheet. (This specimen will henceforth be referred to as specimen #1.) Both surfaces of this disc were polished by mechanical grinding on a lapping machine. Co-P can be polished very easily by lapping because it is hard and brittle. However, for thicknesses less than ~100μm, one must exercise extreme caution in order not to crack the specimen while polishing it. The resulting specimen was flat, smooth and shiny on both surfaces although one surface was shinier than the other.

A second disc, this one spark-cut from the perimeter of the original sheet, was polished in the same manner. The densities of both of the discs were measured by weighing them in benzaldehyde (specific gravity @ 25°C = 1.043) and in air. The density of specimen #1 was found to be (7.81 ± 0.05) g/cm^3 and the density of the disc from the perimeter was (7.89 ± 0.08) g/cm^3. These values are in good agreement with the results

of Cargill and Cochrane (1973) for Co-P samples of slightly different composition. Using the above density and the area of specimen #1, it was determined that the average thickness of that specimen was (78.7 ± 1.2)μm.

A 5 mm long × 1 mm wide strip also was spark-cut from the centre region of the original sheet and mechanically polished to a uniform thickness. This piece was used to measure the temperature dependence of the resistivity, ρ(T). Using indium as a solder, four leads were attached to the strip in a standard four-probe arrangement. At certain discrete temperature values, voltage readings for four or five different current values were taken and a resistance value inferred from the slope of the resulting current versus voltage plot. The results, plotted in Fig. 3.1, indicate a slight resistivity minimum at ~70°K. This is consistent with the results of others (see Rao et al. (1979) and references therein); amorphous metal-metalloid alloys, in general, have resistivity minima. Owing to the small size of the strip, an accurate value of the absolute resistivity was difficult to obtain. The value obtained at room temperature was

$$\rho = (125 \pm 7)\,\mu\Omega\text{cm} \qquad (3.1)$$

It is interesting that not only the qualitative shape of the ρ(T) curve but also the absolute value of ρ found here is very similar to the results of Berrada et al. (1977) for amorphous,

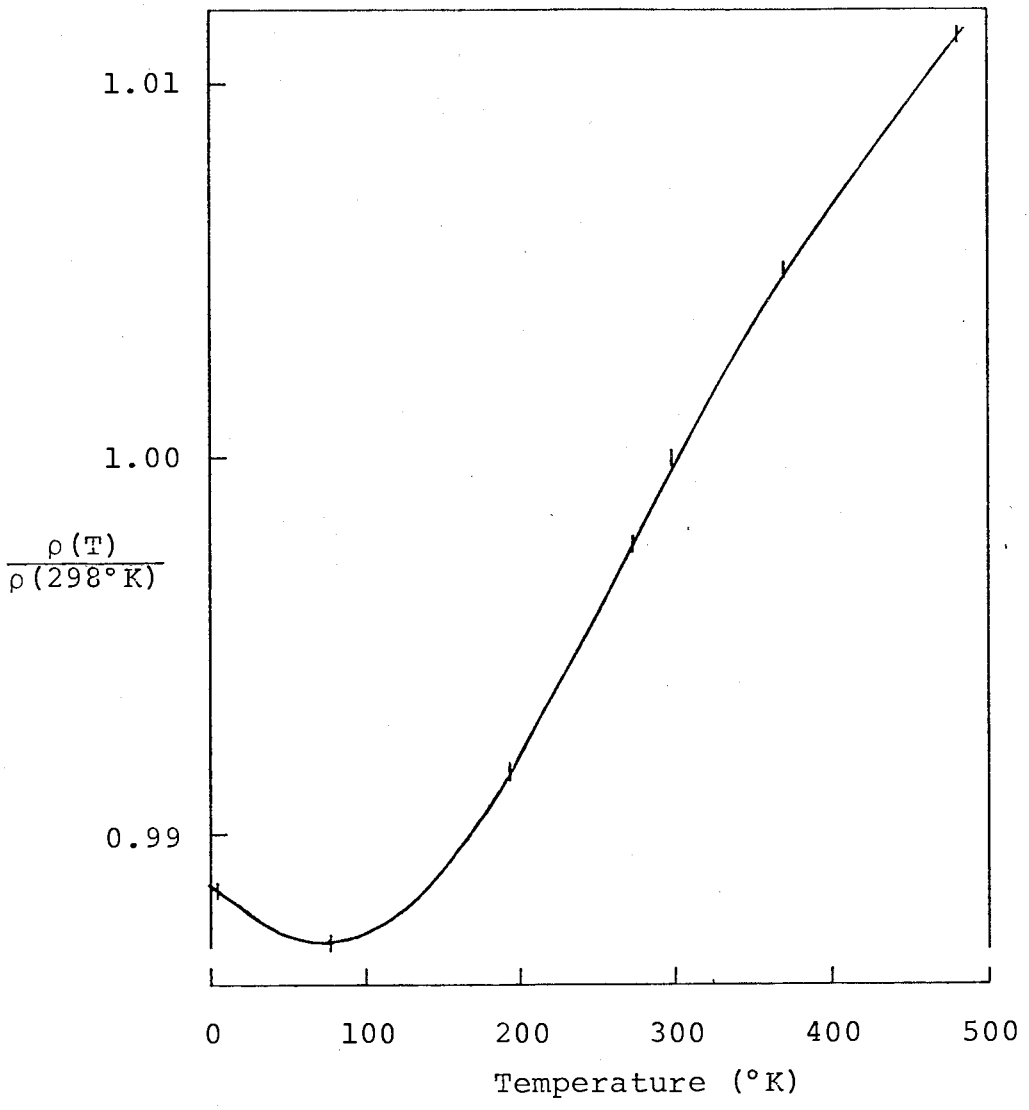

Fig. 3.1

Measured resistivity of Co-P normalized to unity at room temperature plotted as a function of temperature. The absolute resistivity at room temperature is (125 ± 7)μΩcm. The total variation of ρ from 0 to 500°K is less than 2.5%. The curve connecting the data points has been drawn only as a visual aid.

non-magnetic nickel-phosphorus.

Specimen #1 was annealled for 24 hours at 200°C. (According to Chi and Cargill (1976), this particular heat treatment does not produce any significant changes in the radial distribution function of Co-P.) In order to prove that

after the heat treatment the sample was still amorphous, another piece of Co-P was spark-cut from the original sheet, annealled in the same way, ground up, and used in a Debye-Scherrer powder camera. The resulting X-ray photographs displayed only the broad diffraction peaks characteristic of an amorphous material.

After this, sample #1 was mounted over a 3.5 mm diameter hole in a 100μm thick copper diaphragm using pure indium solder. Indium was used for 2 reasons: (1) Its melting point (190°C) is below the recrystallization temperature of Co-P (~280°C) and yet is greater than the temperature at which the FMAR signal became unobservably small; (2) Indium is mechanically very soft and thus is not expected to be able to support a stress large enough to significantly change the magnetic properties of the sample. This second point will be discussed in more detail in section 5.4.

As mentioned in chapter 2, in order to relate the magnetic field internal to the specimen to the externally applied field, it is necessary to know the sample demagnetization tensor $\vec{\vec{N}}$. (It is now more convenient to speak in terms of the tensor $\vec{\vec{D}}$ where $\vec{\vec{D}} = (1/4\pi)\vec{\vec{N}}$.) Specimen #1 was disc-shaped. For this geometry and with axes defined as in Fig. 2.1, $\vec{\vec{D}}$ is diagonal and $D_x = D_y$. The demagnetization factors D_x and D_z were obtained by comparing the shift in the free radical electron paramagnetic resonance field of a small piece of DPPH (α,α' - Diphenyl-β-picryl-hydrazyl) mounted in the centre of

the specimen surface as compared with DPPH mounted on the microwave cavity wall (Frait (1959)). (At the same time, the known g-factor of DPPH was used to calibrate the microwave frequency meter.) Specifically, the microwave power reflected from the resonant cavity was monitored as the externally applied magnetic field was varied. Two EPR signals were observed from the two pieces of DPPH. It is easy to show that the magnetic field just outside the surface of the specimen should have been such that the EPR signals were separated in field by either $4\pi D_x M_S$ (for the parallel configuration) or $4\pi(1 - D_z)M_S$ (in the case of the perpendicular configuration).

For specimen #1, the results at room temperature were

$$4\pi D_x M_S = (36.5 \pm 1.0)\text{oe} \tag{3.2a}$$

$$4\pi(1 - D_z)M_S = (72.5 \pm 3.5)\text{oe} \tag{3.2b}$$

Theoretically, we expect $D_x+D_y+D_z = 1$[†] and hence in our case,

$$1 - D_z = 2\ D_x \tag{3.3}$$

We see that this law is very well obeyed by the results (3.1). Using (3.3) as a constraint on (3.2) and the result that at room temperature, $4\pi M_S = 4.57$ kG (from chapter 4) we find

$$D_x = 0.0080 \pm 0.0002 \tag{3.4}$$

The specimen had an aspect ratio of

$$p = \frac{78.7\mu m \text{ thick}}{6.44 \text{ mm dia.}} = 0.0122 \qquad (3.5)$$

Theoretically, for a uniformly magnetized disc with $p << 1$[†],

$$D_x = p/2 = 0.0061 \qquad (3.6)$$

while for a uniformly magnetized oblate spheroid with the same aspect ratio[†],

$$D_x = \left(\pi/4\right) p = 0.0096 \qquad (3.7)$$

The result (3.4) is therefore consistent with the observations of Kraus and Frait (1973) who found that the oblate spheroid and uniformly magnetized disc models predict lower and upper bounds for the actual effective demagnetization factors for a disc.

3.2 The Microwave Apparatus

3.2.1 The Circuit

The apparatus used to measure the microwave transmittivity of the specimen has been described in detail in a previously published article (Cochran et al. (1977b)). Here I will give only a brief description. A schematic of the microwave circuit

[†]See, for example, Chikazumi (1964), chapter 2.

is shown in Fig. 3.2. About 1 watt of 24 GHz power was generated by a Varian* V1188BF klystron and fed into a critically coupled transmitter cavity. The specimen formed part of a common wall between this transmitter cavity and a critically coupled receiver cavity. The transmitted signal was subsequently chopped at 30 MHz and made to interfere with a reference signal by means of a balanced mixer and preamplifier. The reference signal was tapped directly from the klystron output and its phase could be altered through 360° by means of a precision phase-shifter. The 30 MHz component of the output from the preamplifier was further amplified and then rectified. The result was a DC voltage which was proportional to the amplitude of the microwave signal transmitted through the specimen as well as to the cosine of its phase relative to the reference signal. In practice, it is more convenient to deal with an AC signal. For this reason, a modulator operating at 200 Hz was inserted into the reference arm. The resulting 200 Hz signal was then converted to the desired analog signal by means of a lock-in amplifier locked to the 200 Hz chopper signal used to drive the modulator.

The portions of the schematic in Fig. 3.2 which have not yet been described have to do with stabilizing, tuning, and calibrating the apparatus. A portion of the output of the klystron was directed through a tunable reference cavity and detected by diode D1. The signal from D1 served as the input

*Varian Associates, 611 Hansen Way, Palo Alto, California.

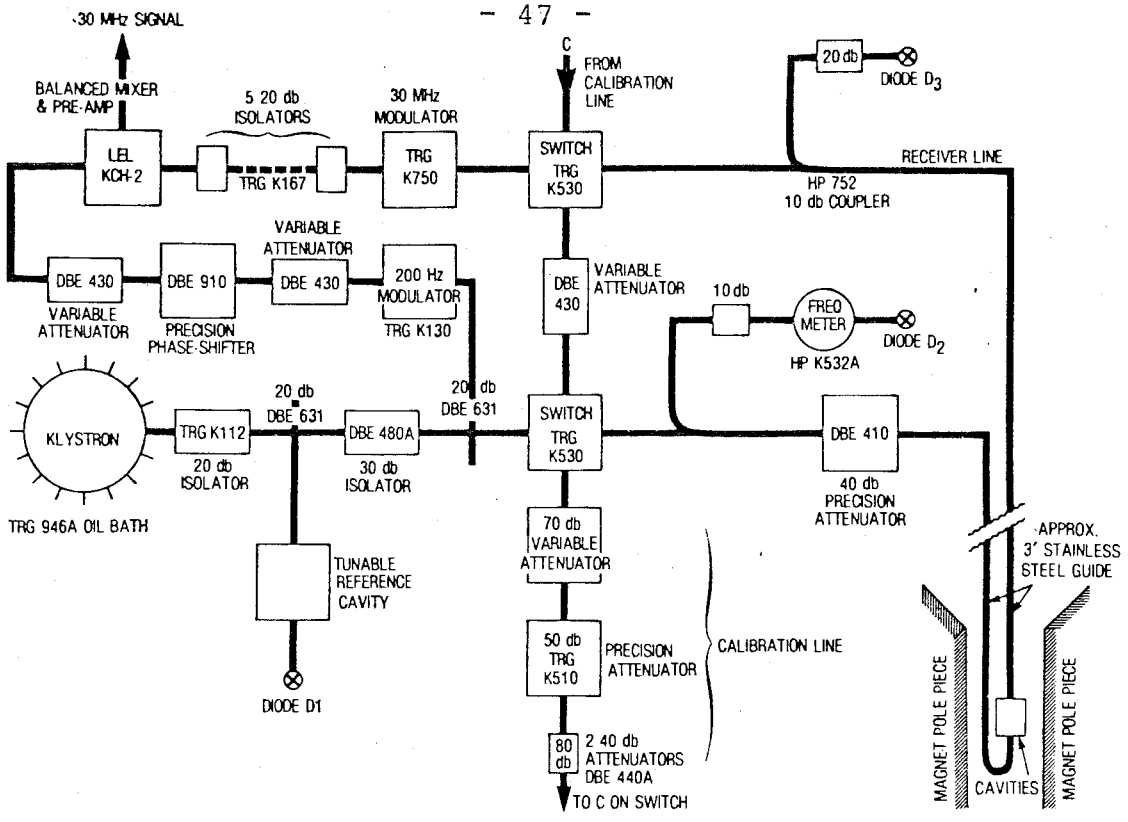

Fig. 3.2

Schematic diagram of the 24 GHz microwave transmission apparatus. (After Cochran et al. (1977b).)

to a control circuit which locked the frequency of the klystron to the resonant frequency of the reference cavity.

By means of two microwave switches, the microwaves could be directed either into the transmitter cavity or into the receiver cavity. The appropriate cavity could be tuned to the klystron frequency by using the cavity tuning rod to minimize the signal reflected from the cavity; ie., the signal appearing at diode D2 or D3. Diode D2 was also used in conjunction with the frequency meter to measure the microwave frequency. After having calibrated this meter (with DPPH as previously described) one could obtain the frequency with an accuracy of $\pm$ 0.015%.

A known fraction of the klystron output could also be shunted into the detection system by way of that part of the circuit of Fig. 3.2 labelled 'calibration line'. This feature was useful not only in calibrating the sensitivity of the receiver but also in calibrating the phase shifter. The latter calibration was performed by noting the two positions of the phase shifter for which the detected signal was zero and a maximum. These two settings, therefore, corresponded to phases (call them ϕ_1 and ϕ_2) which were separated by 90°. One could reproduce these settings to within 1°. Transmission measurements were always done in pairs; one at each phase. The transmitted microwave amplitude was then found by taking the square root of the sum of the squares of the two amplitudes and the relative phase was found by taking the arctangent of the ratio of the two amplitudes.

3.2.2 The Cavities

The cavities that were used are shown schematically in Fig. 3.3. These were identical to the stainless steel cavities described by Cochran et al. (1977b) except that they were made of brass. The cavity cross-section was 1.07 × 0.44 cm. This is identical to the cross-section of the K-band waveguide used in the rest of the microwave circuit and results in a guide wavelength in the propagating TE_{10} mode at 24 GHz of 1.54 cm. Hence, the inside length of the cavities, 3.06 cm, was very slightly less than two guide wavelengths. The sample (D in Fig. 3.3) was exposed by means of the 3.5 mm diameter

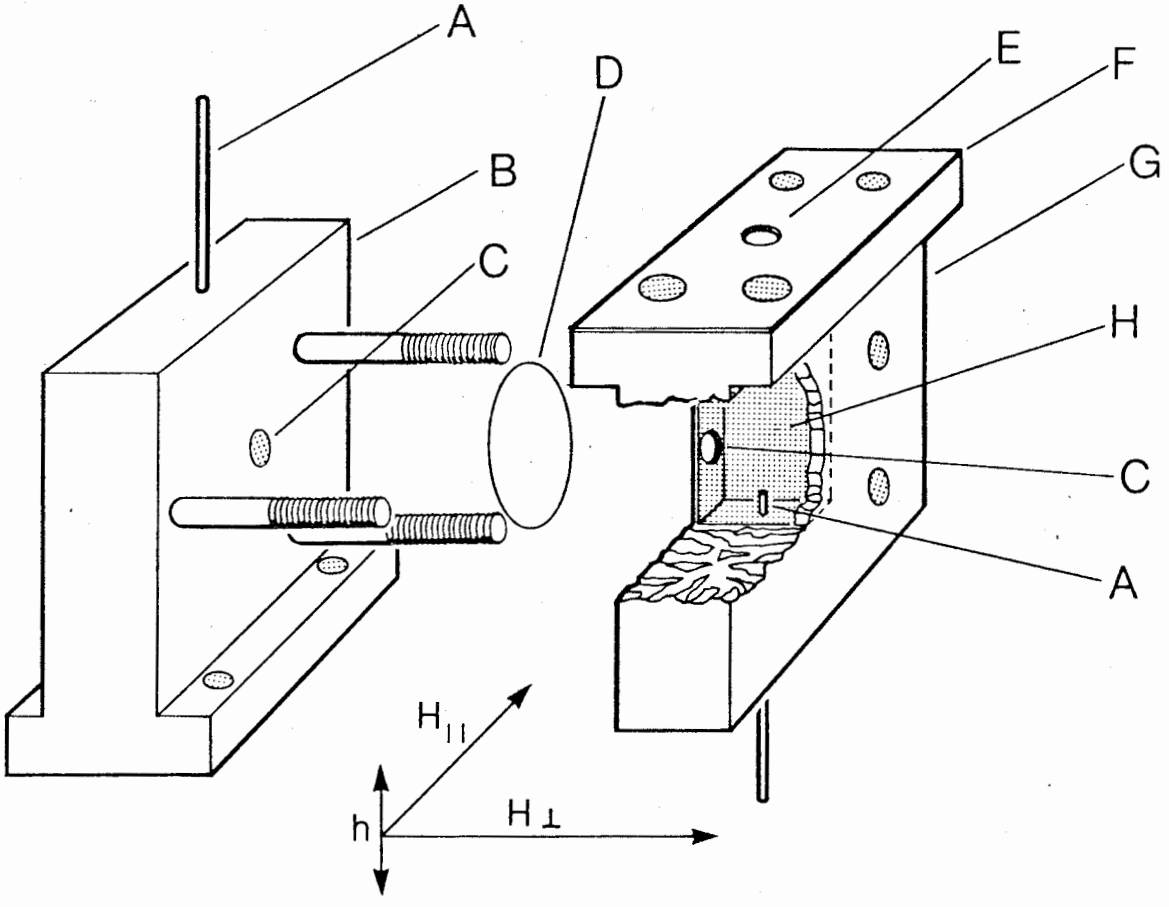

Fig. 3.3

View of the cavities and the specimen: (A) quartz tuning rod, (B) transmitter cavity, (C) coupling hole, (D) specimen (specimen diaphragm not shown), (E) critical coupling aperture between cavity and waveguide, (F) copper diaphragm, (G) receiver cavity, (H) interior of receiver cavity. The transmitter cavity was bolted to the receiver cavity with the sample diaphragm sandwiched tightly between. The total height of each cavity was 4.44 cm. The directions labelled $H_{||}$, and $H_{\perp}$ and h are, respectively; the external static magnetic field direction in the parallel configuration, the magnetic field direction in the perpendicular configuration and the direction of the radio frequency magnetic field. (After Cochran et al. (1977b).)

coupling holes (C) cut into the 200 μm thick narrow faces of the cavities. The coupling hole was placed in the h-wall of

the cavity one quarter of a guide wavelength from the end wall. This is a position of maximum radio frequency h-field and, also at this position, $\vec{h}$ is in the vertical direction. Hence, by rotating the magnet in the horizontal plane, one could make measurements for any orientation of the applied field, $\vec{H}_o$, with respect to the sample normal all the while maintaining $\vec{h}$ perpendicular to $\vec{H}_o$. By altering the depth of insertion of the 1 mm diameter tuning rods (A), one could not only tune the cavities to the maximum power frequency of the klystron but one could also compensate for changes in the cavity resonance frequency due to thermal expansion or to changes in the index of refraction of the gas inside the cavities. Quartz has an index of refraction greater than unity and so increases the effective volume and decreases the resonance frequency of a microwave cavity as it is inserted. The holes into which the tuning rods were inserted were 1 mm in diameter by 1.38 cm long. The damping length of 24 GHz radiation through a hole of this diameter is ~0.7 mm. (This takes into account the index of refraction of the quartz tuning rod.) Hence, 1.38 cm corresponds to ~ 20 damping lengths. Consequently, the tuning holes caused no microwave leakage problems.

The cavities were coupled to the rest of the microwave circuit by means of 127μm thick copper diaphragms (F). Holes (E) were cut into the diaphragms and adjusted in size until critical coupling was attained; that is, until less than 5%

of the incident power was reflected by the cavity at cavity resonance. At critical coupling, the half power frequencies of a cavity resonance were typically separated by ~ 32 MHz. This corresponds to an intrinsic quality factor of 1500.

3.2.3 The Apparatus for Temperatures Other Than Room Temperature

For making measurements at temperatures either higher than or lower than room temperature, the cavities and ~ 3 feet of stainless steel waveguide (see Fig. 3.2) were enclosed in a dewar. Above room temperature it was not necessary to use a dewar any more sophisticated than an evacuable container. Pressures of ~ 10^{-4} Torr were sufficiently low to prevent significant oxidation of the Co-P sample at the highest temperature used (~ 150°C). To heat the specimen, current was passed through a power resistor mounted below the cavities.

For temperatures less than room temperature, a liquid helium dewar containing a liquid nitrogen jacket was used. (See Lyall (1970) for a complete description of this dewar.) Measurements at temperatures above 4.2 °K were made on the fly (so to speak) as the apparatus warmed after all the liquid helium had boiled off. This was possible because the warming rate was never more than one degree over the time it took to make one run. One run consisted of two field sweeps (one for each phase) at ~5 minutes per sweep.

Temperatures were measured by simultaneously using both a copper vs. constantan and a chromel vs. gold + 0.07 atomic

% Fe thermocouple. Both thermocouples were soldered to a small copper plate which was bolted to the cavities. Both thermocouples were referenced to 273°K by means of an ice bath. The boiling points of helium and of nitrogen were used to correct previously published* calibration data for these types of thermocouples. In this manner, accuracies of better than 1 degree were possible for temperatures below room temperature. Above room temperature, the chromel vs. Au + 0.07 at. % Fe thermocouple was not useful; nonetheless, the temperature error should have been no larger than 2 degrees.

3.2.4 The Magnet

Magnetic fields were obtained by means of a Varian V-3800 fifteen inch electromagnet† having a 3 1/2 inch pole gap. It was capable of providing fields up to 16 koe in strength which were stable to within 0.1 oe and homogeneous to better than 0.1 oe over the volume of the specimen. A signal proportional to the field strength was obtained from a Bell model 810 gaussmeter**. This instrument was calibrated at two different values of magnetic field after each run by means of a proton nuclear magnetic probe. Over a linewidth, the magnetic

---

* The calibration data of L.L. Sparks et al. (1968) was used for the chromel vs. Au + 0.07 at. % Fe thermocouple; for the Cu vs. constantan thermocouple, the data of Shenker et al. (1955) was used.

† Varian Associates, 611 Hansen Way, Palo Alto, California.

** F.W. Bell, Inc., Columbus 12, Ohio.

field was assumed to be directly proportional to the gauss-meter signal. This assumption introduced errors in the value of the magnetic field which were no larger than 1 oe.

3.3 The Experimental Procedure

In order to give the reader a clearer idea of the procedure involved in making a microwave transmission measurement, a typical 'run' will here be described. First, the specimen was mounted between the cavities, the cavities mounted to the rest of the system and the dewar attached. After the sample had reached the desired temperature and the klystron had been locked to the reference cavity resonance frequency*, the receiver and transmitter cavities were tuned. At this point, the magnetic field was swept through FMR. Any field dependence of the transmitted signal in this range was necessarily spurious and meant that microwaves were leaking around the sample. The problem could always be solved by tightening the sample and cavity mounting screws (Fig. 3.3). Next, the specimen was aligned so that the angle between its normal and the magnetic field direction was so small that the FMAR line position was in error by less than 0.1 oe. This was done by making use of the fact that the FMAR transmission signal in perpendicular configuration exhibits a phase which is very sensitive to the angle between the specimen normal and the magnetic field.

*One seldom disturbed the setting of the reference cavity because it was necessary to recalibrate the phase shifter each time the klystron frequency was changed.

When the above 'preparatory work' had been completed, two field sweeps were made - one for each phase - each at a rate of ~ 2000 oe/10 min. This rate enabled one to use a time constant for the 200 Hz lock-in amplifier of 0.3 second with negligible ($\lesssim 1$ oe) consequent hysteresis. With this time constant, the system sensitivity was $\sim 10^{-17}$ watt. The signals from the lock-in amplifier and the gaussmeter were continuously recorded on an X-Y recorder for immediate viewing. Simultaneously, these signals were being digitized every 2 seconds and sent to the IBM 370 model 155 computer for permanent storage. After each sweep, the magnetic field was brought to a value (usually $\sim$ 2 koe above FMAR) where the transmitted amplitude should have been negligible ($<< 10^{-17}$ watt). The amplitude measured at this field was later used as a 'zero level' and subtracted from the transmission data for the appropriate phase. Zero level measurements were necessary because a field-independent background signal of $\sim 10^{-15}$ watt was always present in the apparatus. This remanent signal was due to direct leakage between the transmitter and receiver waveguide systems. After the data of the second phase had been recorded, the magnetic field was calibrated against a proton NMR standard field in the manner previously described.

3.4 Data Analysis

In order to prepare the results of a run for comparison with theory, the stored data were processed as follows. First the zero levels were subtracted from the data for each phase.

Then a program was run which used a simple linear interpolation scheme to construct data points for each phase on the same grid of 180 evenly spaced magnetic field values. The field grid spanned the same field range as was used for the experimental run. Having obtained both phases of the transmission signal for the same values of magnetic field, one could view the data on a Tektronix 4013 Computer Display Terminal* either in the form of transmission versus magnetic field (eg. Fig. 4.1a) or as a polar plot in which amplitude was plotted against the phase of the transmitted signal with magnetic field as an implicit variable (eg. Fig. 4.1b).

A computer program written by Andrew Kurn in FORTRAN IV was used to execute the boundary value problem described in section 2.2.1. This program is described by Cochran et al. (1977a). The input parameters were the external field range and the angle between the external field and the specimen normal; resistivity, ρ; disc thickness, d; frequency of radiation, $\nu = \omega/2\pi$; saturation magnetization, M_S (assumed to be independent of field); ω/γ; exchange stiffness constant, A; a damping parameter (either λ, G, or $1/\tau$); front and rear pinning parameters; and demagnetization factors, D_x and D_z. This program was capable not only of calculating the amplitude and phase of the transmitted microwave signal but also the total energy absorbed by the sample. The main output from the program was a plot (or printout) of the external field variation of the

* Tektronix Inc., P.O. Box 500, Beaverton, OR 97005, U.S.A.

transmission amplitude (or the absorption) and, if desired, a locus plot of transmission amplitude versus phase. A given plot could be superposed on the corresponding experimental plot and the two compared. Those parameters which had not been accurately predetermined by external measurements - namely, γ, ρ, λ, and M_S* - were adjusted until the best possible agreement between experiment and theory was secured. The g-factor and the magnetization were initially determined from the measured positions of peak transmitted amplitude in the two configurations (parallel and perpendicular). The two remaining parameters (λ and ρ) as well as more precise values for g and M_S were then deduced from the detailed comparison between calculated and experimental plots.

At first thought, it may seem that since λ and σ† are both

---

*As expounded in section 2.2.2b, the exchange and the pinning parameters affect the transmission signal only negligibly. As a matter of fact, for transmission fitting, it was found more convenient to use a version of the computer program written by Graeme Dewar (1978)) which neglected the exchange parameter (thereby making a pinning condition unnecessary) since this program was an order of magnitude faster (3 seconds central processing time vs. 30 seconds).

---

†When comparing magnetic damping with eddy-current damping, it is more convenient to speak in terms of σ, the conductivity rather than ρ, the resistivity. This is because just as magnetic damping is proportional to λ, so also is eddy-current damping proportional to σ.

parameters of absorption mechanisms (magnetic damping and eddy-current damping), they will affect the transmission signal in the same way. While it is true that increasing λ has the same effect as increasing σ on both the peak absolute transmitted amplitude (see equation (2.57)) and the locus plot (compare Fig. 3.4b with Fig. 3.5b), their effects on the width of the amplitude versus field plots are opposite. That is to say that decreasing σ will broaden the transmission lineshape while decreasing λ will make it narrower. (Compare Fig. 3.4a with Fig. 3.5a.) This is due to the very nature of antiresonance: at antiresonance, the eddy-current losses are a minimum. If these losses are further decreased by decreasing σ, the antiresonance effect will become less pronounced; that is, the lineshape will be broadened.

At any one discrete temperature, the 4 experimental plots (field and locus plots for both the parallel and the perpendicular configuration) were fitted using the 4 parameters g, M_s, $\lambda_{||}$ (the damping parameter for the parallel configuration), and $\lambda_{\perp}$ (the damping parameter for the perpendicular configuration). The resistivity should not be considered as an adjustable parameter because it was only fitted once. (This statement will be clarified in the next chapter.) While theory was made compatible with the data by using these 4 parameters, there were also 3 characteristics of the experimental data which were allowed to vary more or less freely. These were the following: (1) The absolute phase of the

Fig. 3.4: (a) Calculated relative transmission amplitude versus external magnetic field and (b) the corresponding locus plot (polar plot of transmission amplitude versus phase) for 3 different values of the Landau-Lifshitz damping parameter, λ. Arrows indicate the curve for which $\lambda = 1.85 \times 10^{8}\ sec^{-1}$, and the other two curves correspond to the values $\lambda = 1.65 \times 10^{8}\ sec^{-1}$ and $1.45 \times 10^{8}\ sec^{-1}$ respectively. The other parameters used for this calculation are: conductivity, $\sigma = 7.25 \times 10^{15}\ sec^{-1}$ (resistivity, $\rho = 124 \times 10^{-6}\ \Omega$-cm); angle between applied field and sample normal, $\theta = 0°$ (perpendicular configuration); $\omega/\gamma = 8.027$ koe; $4\pi M_S = 4.476$ kG; microwave frequency, $\omega/2\pi = 23.916$ GHz; thickness, $d = 78.7\mu m$; and demagnetization factors, $D_x = 1/2\ (1 - D_z) = 0.0080$.

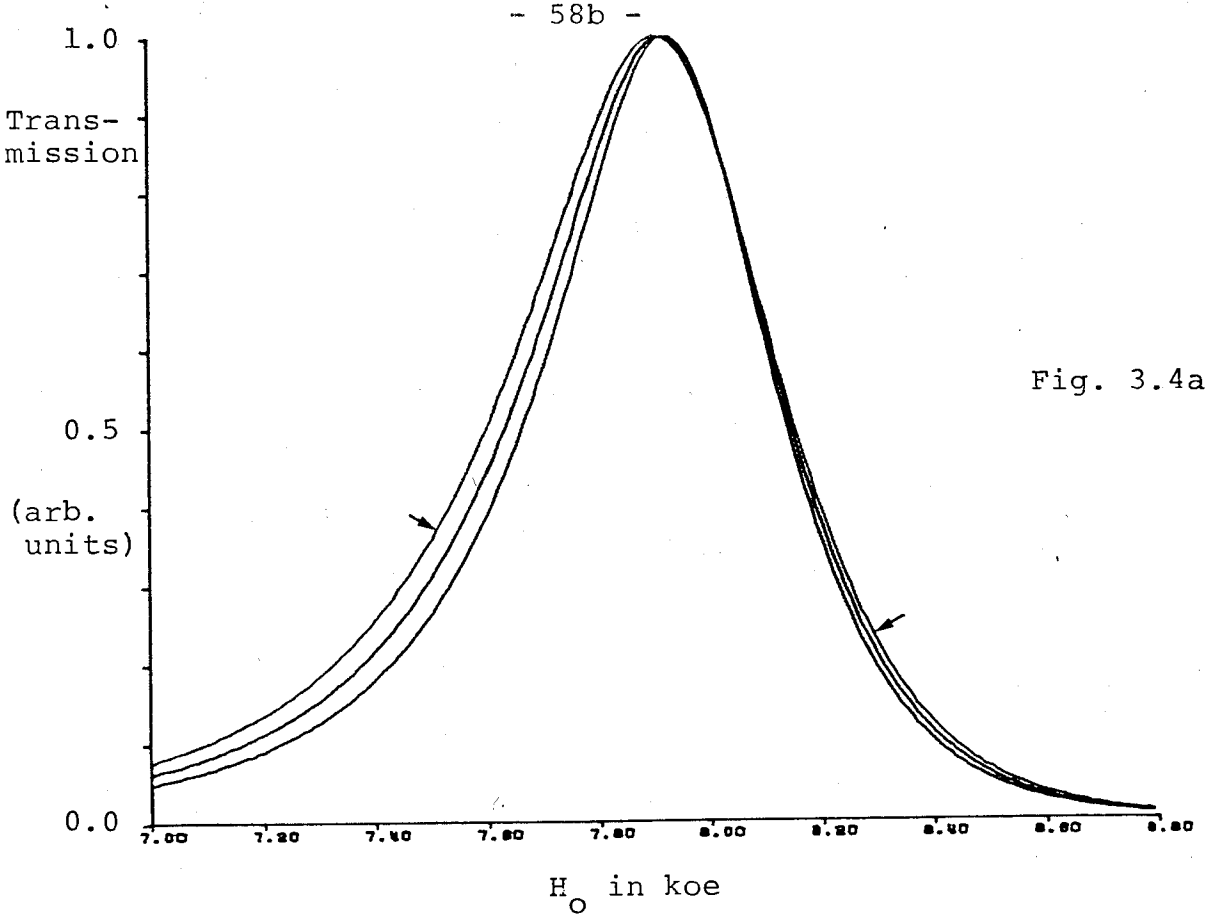

Fig. 3.4a

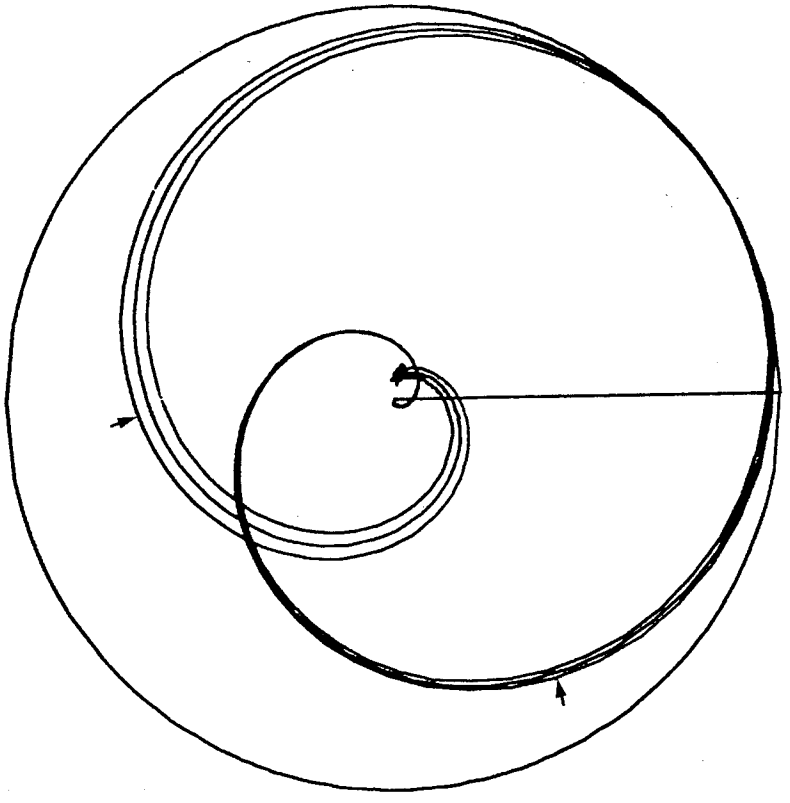

Fig. 3.4b

Fig. 3.5: (a) Calculated transmission amplitude versus external magnetic field and (b) the corresponding locus plot for 3 different values of the conductivity. Arrows indicate the curve for which $\sigma = 8.25 \times 10^{15}\ sec^{-1}$ ($\rho = 109 \times 10^{-6}\Omega$-cm), and the other two curves correspond to the values $\sigma = 7.25 \times 10^{15}\ sec^{-1}$ and $6.47 \times 10^{15}\ sec^{-1}$ ($\rho = 124 \times 10^{-6}\Omega$-cm and $139 \times 10^{-6}\Omega$-cm) respectively. For all 3 curves, $\lambda = 1.65 \times 10^{8} sec^{-1}$ and the other parameters used for the calculation are the same as those of Fig. 3.4. As with Fig. 3.4, the 3 curves have been normalized to the same maximum amplitude.

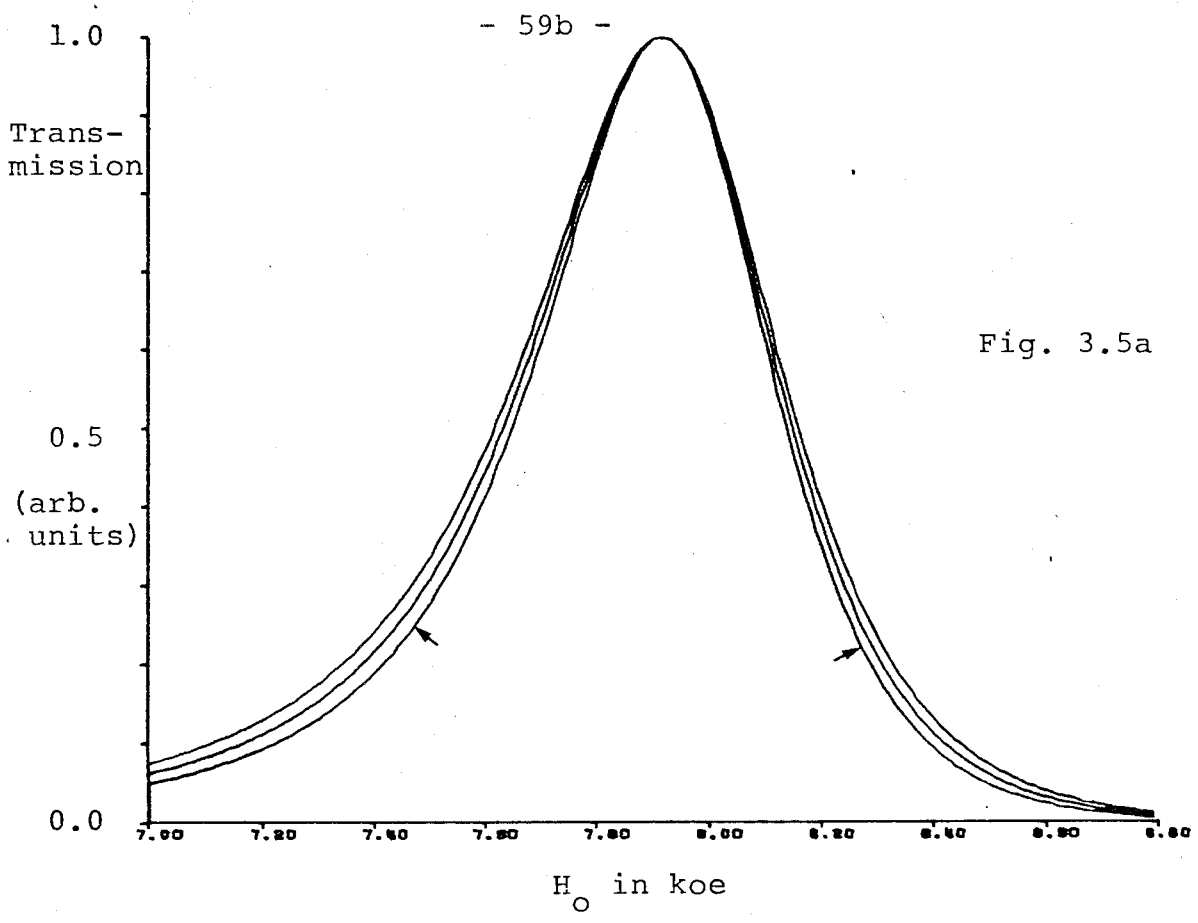

Fig. 3.5a

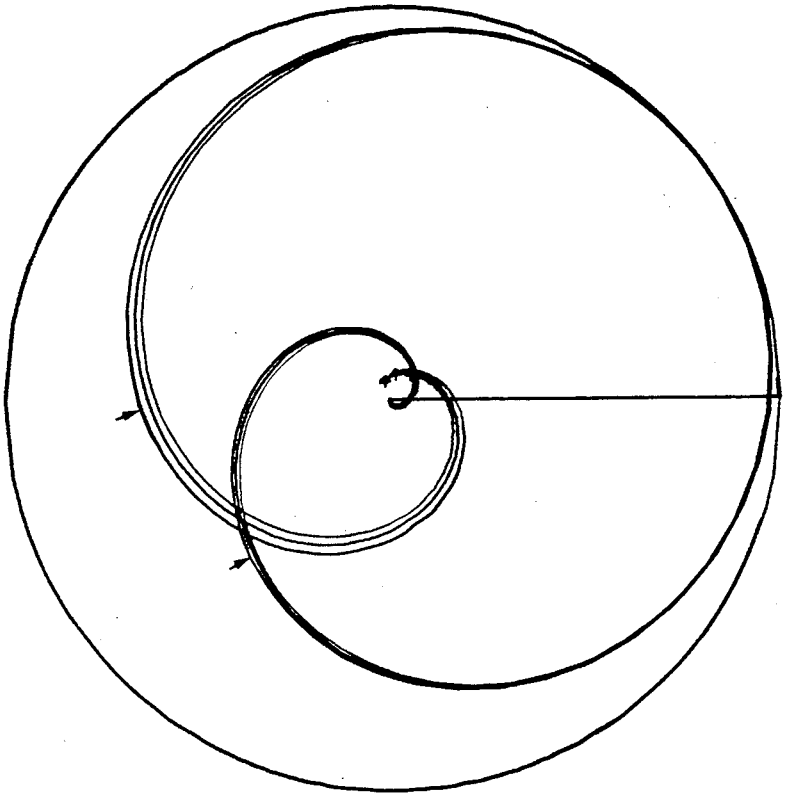

Fig. 3.5b

transmitted signal was not relied upon. In principle, one should be able to compare the phases of two different runs. However, the phase of the transmitted signal is so very sensitive to cavity coupling and cavity tuning that in practice this proved impossible. Changing the phase does not, of course, alter the transmission versus field plot; its only effect is to rotate the locus plot.

(2) As previously noted, phase shifter settings were only reproducible to approximately 1 degree. For this reason, it was necessary to allow for an error in the phase ϕ_2 relative to ϕ_1 of as much as 2 degrees. Adjusting the relative phase between the 2 field sweeps should not be considered as using up one 'degree of freedom' of the experimental data because it is impossible to duplicate the effects of such an adjustment with any one or a combination of the theoretical parameters at one's disposal. The effect of assuming an incorrect relative phase value is to introduce a sinusoidal modulation on top of the usual Lorentzian transmission lineshape.

(3) Although the experimental absolute transmitted amplitude was used for some data analysis purposes (see next chapter), its exact value in the case of any particular run was not useful. This was because the sensitivity of the microwave system (ie. the cavities) was very dependent upon

temperature and whatever gas* (He, N_2, or air) was inside the cavities at the time of the run. For this reason, theory and experiment were in general normalized to the same maximum amplitude when curve-fitting FMAR data.

3.5 FMR Apparatus

In analyzing the FMAR results, it was found necessary to postulate the existence of a small anisotropy field. This represents a third parameter which could influence the FMAR line position. At a given temperature, only the two line positions of parallel and perpendicular configurations are available, so it was necessary to obtain additional data in order to measure the contribution of anisotropy fields to the FMAR position. For this purpose, room temperature ferromagnetic resonance at 9 and at 24 GHz was used. The apparatus used for FMR absorption measurements at 24 GHz was identical to that described by Cochran et al. (1977b). Briefly, it consisted of a single critically coupled cavity into which microwaves which had been chopped at 7 Hz were fed. The sample formed part of one end wall of the cavity. Two DC biased thermistors were used; one which monitored the power level in the cavity, and one in contact with the back side of the specimen.

---

*The index of refraction of the medium inside the cavities was important because it changed the cavity coupling by changing the effective sizes of the coupling holes. In principle, one could correct for this by measuring the cavity coupling after each experimental run. Unfortunately, I did not have the forethought to make this measurement.

The amplitude of the 7 Hz component of the signal from each of the thermistors was measured by means of two lock-in amplifiers. A ratiometer was employed to find the ratio of these two amplitudes. The output signal from the ratiometer was digitized, recorded, and subsequently numerically smoothed and differentiated with respect to field in order to obtain the position of peak absorption with an accuracy of $\pm$ 4 oe.

The apparatus used for measuring FMR at 9 GHz was considerably more simplistic. The cavity used in this case was 50% undercoupled (ie. the size of the coupling hole was adjusted so that approximately 50% of the power incident on the cavity was reflected). A diode was used to monitor the reflected power. The external magnetic field was modulated at 55 Hz. The diode signal at the modulation frequency was proportional to the derivative of reflection with respect to field. In this way it was possible to locate the field corresponding to maximum absorption with an accuracy of $\pm$ 2 oe.

CHAPTER 4

RESULTS

Typical examples of the degree of agreement which can be obtained between theory and experiment are shown in Figs. 4.1, 4.2, 4.3, 4.4, 4.5, and 4.6. Of the six, the odd numbered figures are results from the perpendicular configuration and the even numbered ones are from the parallel configuration. Figs. 4.1 and 4.2 portray results from room temperature measurements; Figs. 4.3 and 4.4 from liquid helium temperature; and Fig. 4.5 and 4.6 from T = 379°K. These fits were obtained by normalizing experimental and calculated data to the same maximum amplitude and by allowing the Landau-Lifshitz damping parameter, λ, the magnetization, M_S, and the g-value unrestricted freedom in order to obtain the best possible fit. The resistivity, ρ, was treated in a slightly different manner. Initially, all the data from all the different temperature runs were fitted allowing ρ, λ, g, and M_S to vary as necessary to obtain the best possible fits. The resistivities obtained in this way were normalized to the room temperature value by using the measured temperature dependence of ρ (Fig. 3.1) and then were averaged. This yielded a room temperature resistivity of* $(124 \pm 6)\mu\Omega$cm in

*Strictly speaking, the fitted parameter was d/δ and the rather large uncertainty in the fitted value of ρ is due to a $\pm$ 1.5% uncertainty in d. Effectively, then, for further fitting purposes, the resistivity can be considered to be known to within 2% (the uncertainty in d/δ).

Fig. 4.1: (a) Transmission amplitude versus applied magnetic field and (b) the corresponding locus plot (polar plot of transmission amplitude versus transmission phase) for the perpendicular configuration. The measurement (crosses) was made at 305°K. Parameters used for the calculation (solid line) are: ω/γ = 8.027 koe, $4\pi M_S$ = 4.476 kG, λ = 1.65 $\times 10^8 sec^{-1}$, ρ = 124.0 $\times 10^{-6}$ Ωcm, $\omega/2\pi$ = 23.916 GHz, d = 78.7μm, and $D_x = 1/2\ (1 - D_z)$ = 0.0080. Theory and experiment have been normalized to the same maximum amplitude. The parameters ω/γ, $4\pi M_S$, and λ were found from curve-fitting the experimental points in this figure and Fig. 4.2 while the other parameters had been determined from separate, independent measurements.

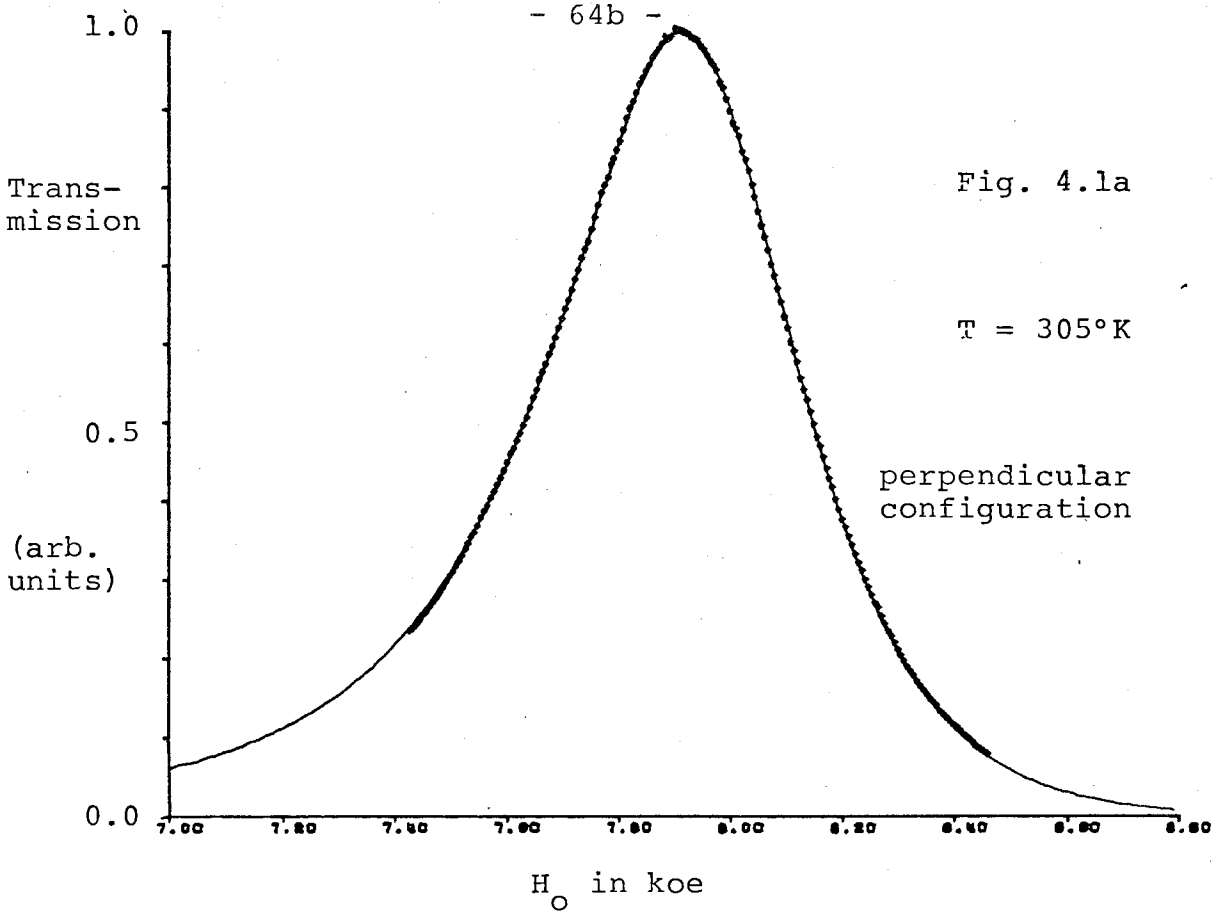

Fig. 4.1a

T = 305°K

perpendicular
configuration

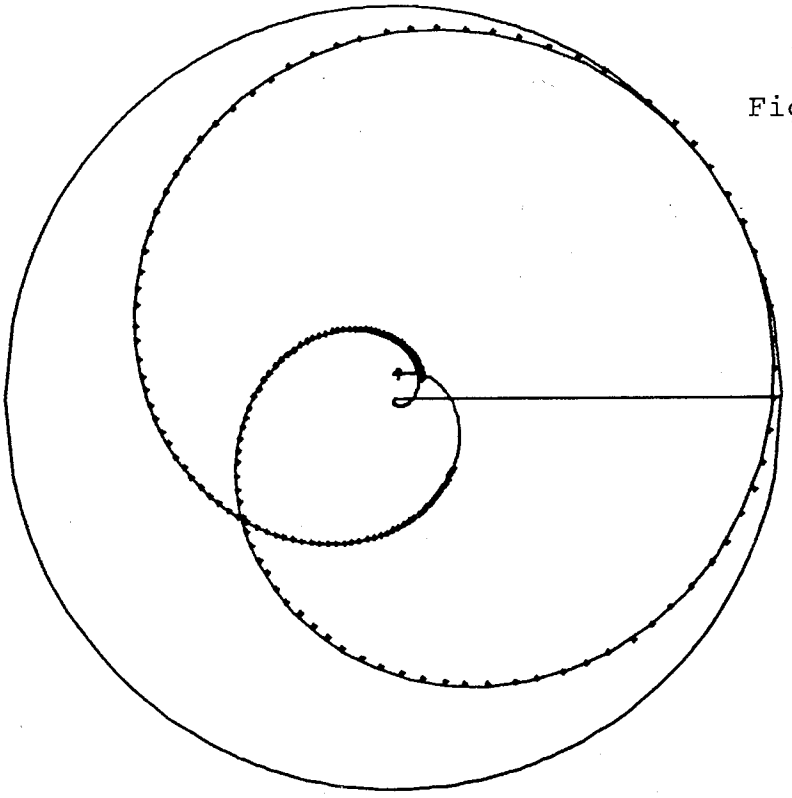

Fig. 4.1b

Fig. 4.2: (a) Transmission amplitude versus applied magnetic field and (b) the corresponding locus plot in the parallel configuration. The measurement (crosses) was made at 305°K. The Landau-Lifshitz damping parameter used for the calculation (solid line) is $\lambda = 1.70 \times 10^{8} \text{sec}^{-1}$ and all other parameters are the same as those used for Fig. 4.1. Theory and experiment were normalized to the same maximum amplitude.

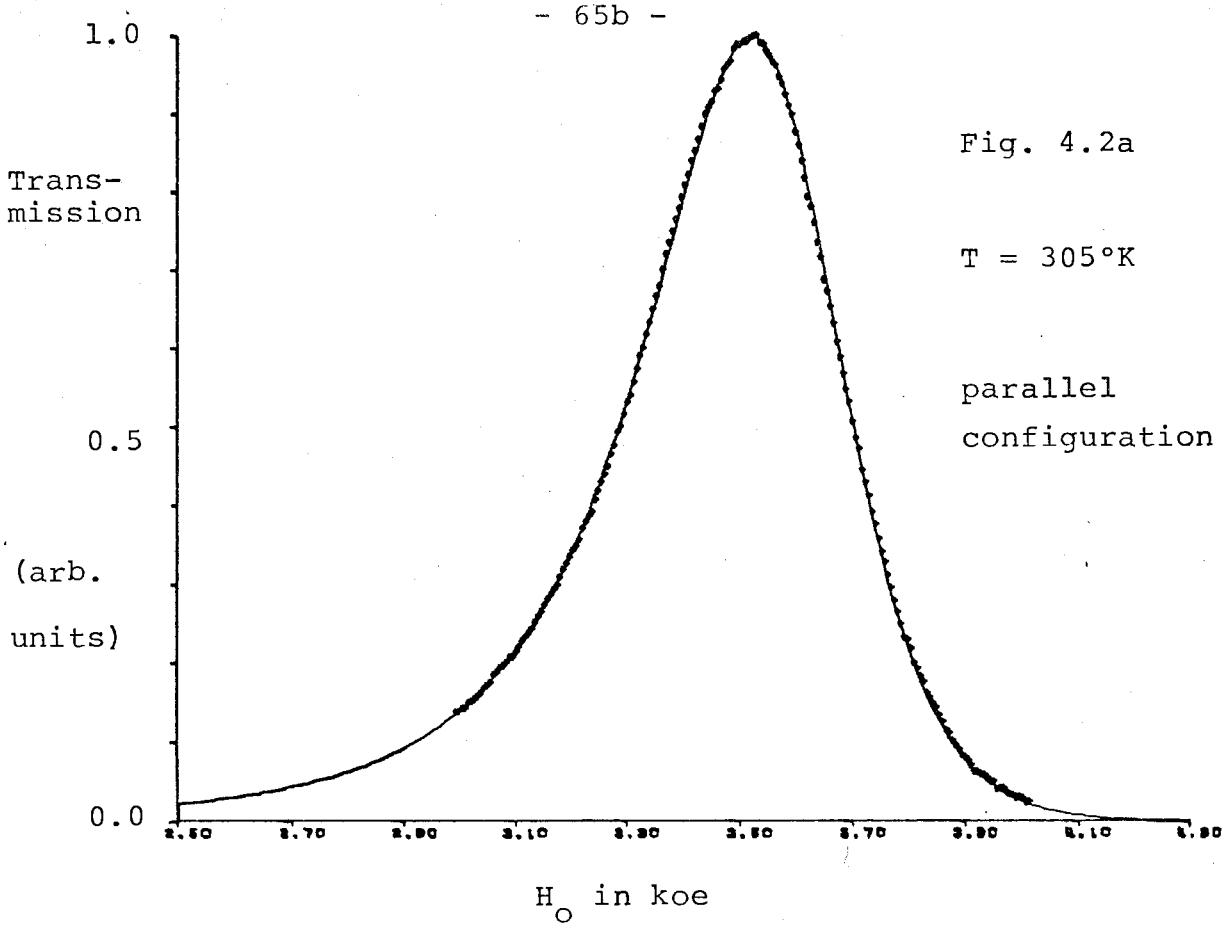

Fig. 4.2a

T = 305°K

parallel
configuration

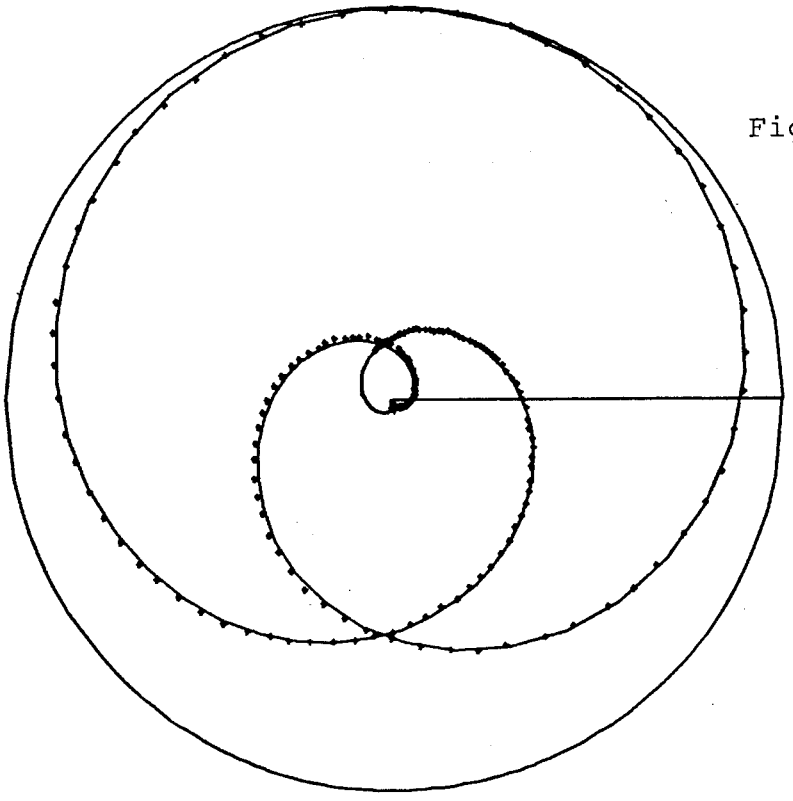

Fig. 4.2b

Fig. 4.3: Transmission versus field in the perpendicular configuration. Experimental points arise from a measurement carried out at 5°K. The solid curve was calculated using the fitted parameters: $\omega/\gamma = 8.106$ koe, $4\pi M_S = 6.414$ kG, and $\lambda = 1.60 \times 10^8 \text{sec}^{-1}$. The other parameters (those determined from external measurements are: $\rho = 122.6 \times 10^{-6} \Omega\text{cm}$, $\omega/2\pi = 23.953$ GHz, and d, D_x and D_z are the same as those of Fig. 4.1. Experiment was normalized to the amplitude that gave the best overall fit.

Fig. 4.4: Transmission versus field in the parallel configuration at T = 5°K. The parameters used for the calculation were identical to those used for Fig. 4.3 with the exception of λ: it had the value $1.62 \times 10^8 \text{sec}^{-1}$ in this case. The experimental data were again normalized to the amplitude that gave the best fit.

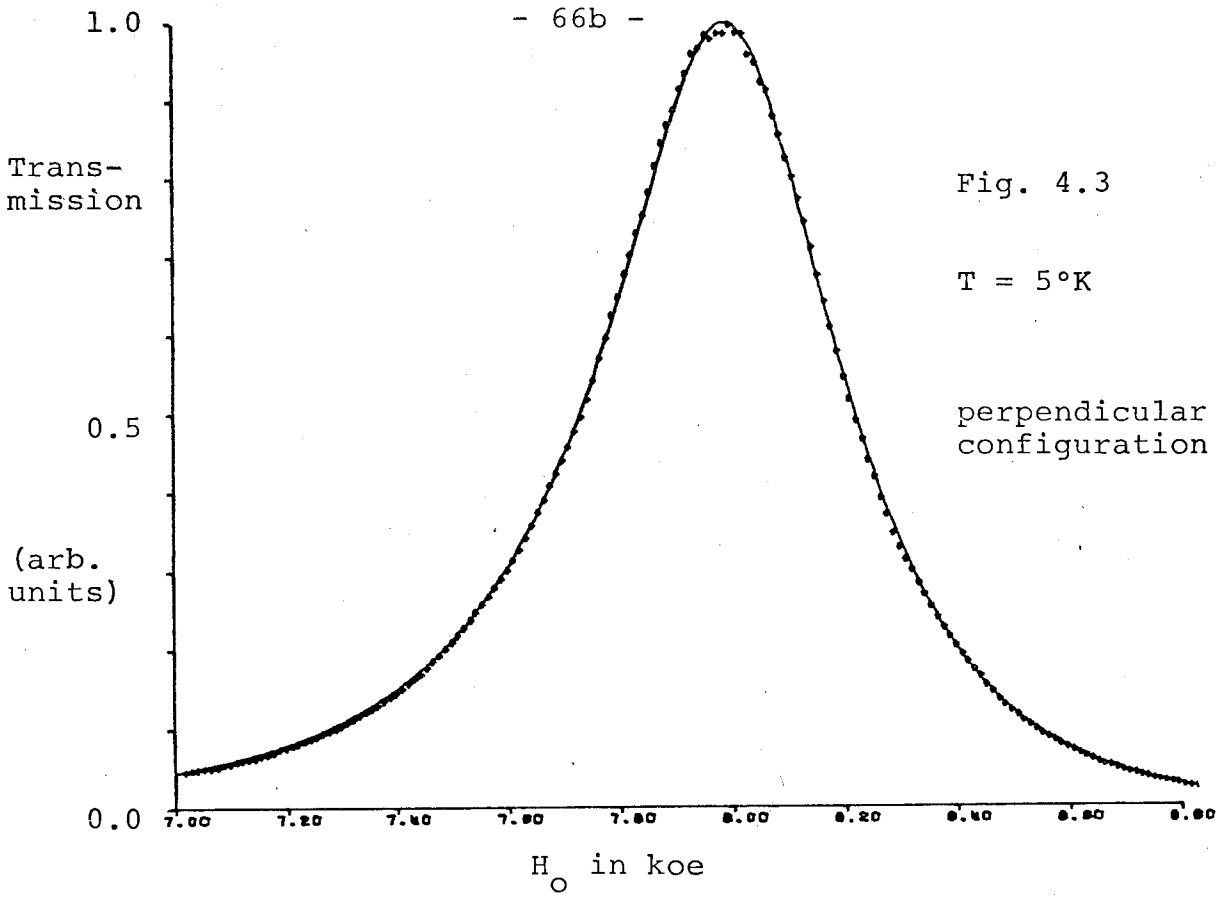

Fig. 4.3

T = 5°K

perpendicular
configuration

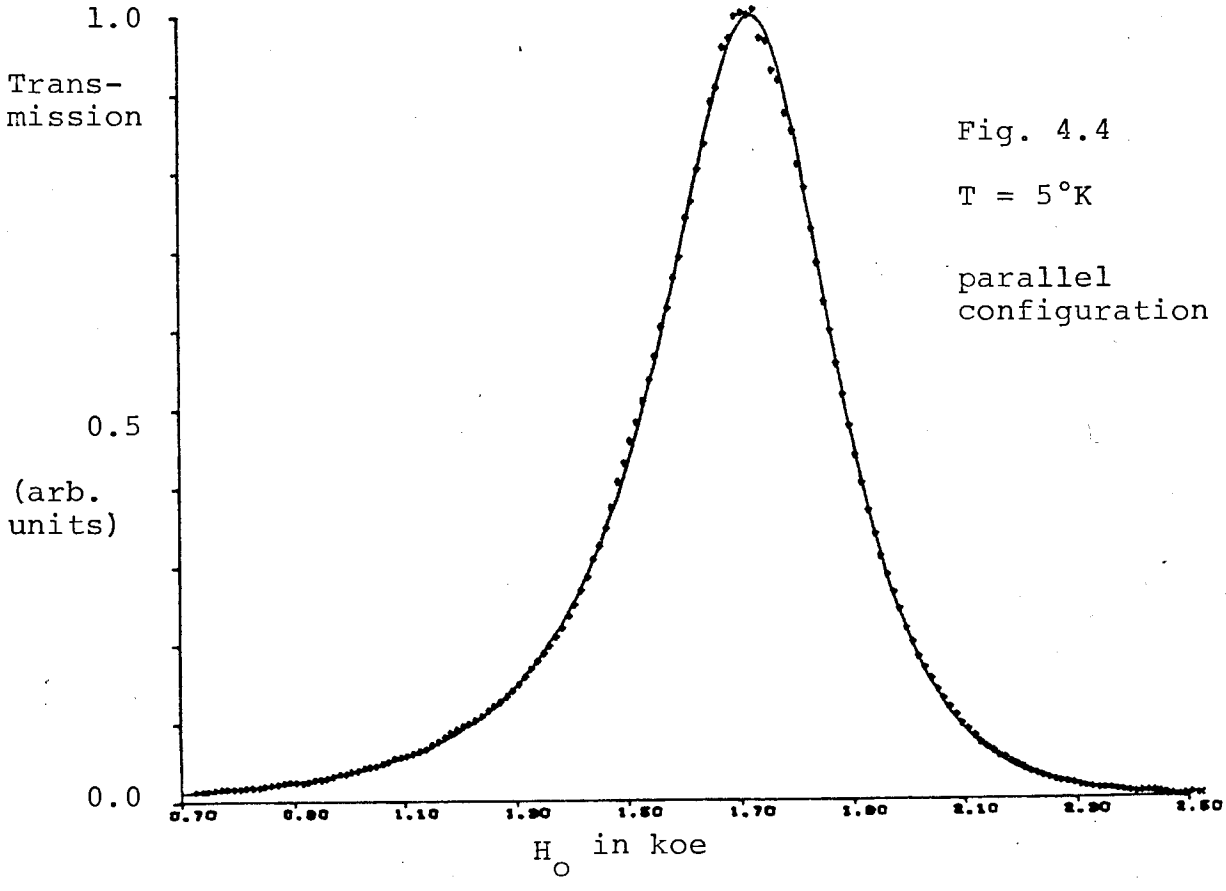

Fig. 4.4

T = 5°K

parallel
configuration

Fig. 4.5: Transmission versus field in the perpendicular configuration. Experimental points arise from a measurement carried out at 379°K. The solid curve was calculated using the fitted parameters: ω/γ = 7.993 koe, $4\pi M_S$ = 3.310 kG, and $\lambda = 1.69 \times 10^8 sec^{-1}$. The other parameters are: ρ = 124.7$\mu\Omega$cm, $\omega/2\pi$ = 23.916 GHz and d, D_x, and D_z are the same as those of Fig. 4.1. Experiment was normalized to the amplitude that gave the best overall fit.

Fig. 4.6: Transmission versus field in the parallel configuration at T = 379°K. The solid curve was calculated using $\lambda = 1.75 \times 10^8 sec^{-1}$ and all other parameters used were the same as those of Fig. 4.5. Again, the experimental data was normalized to the amplitude that gave the best fit. This amplitude corresponds to approximately 10^{-15} watts of power.

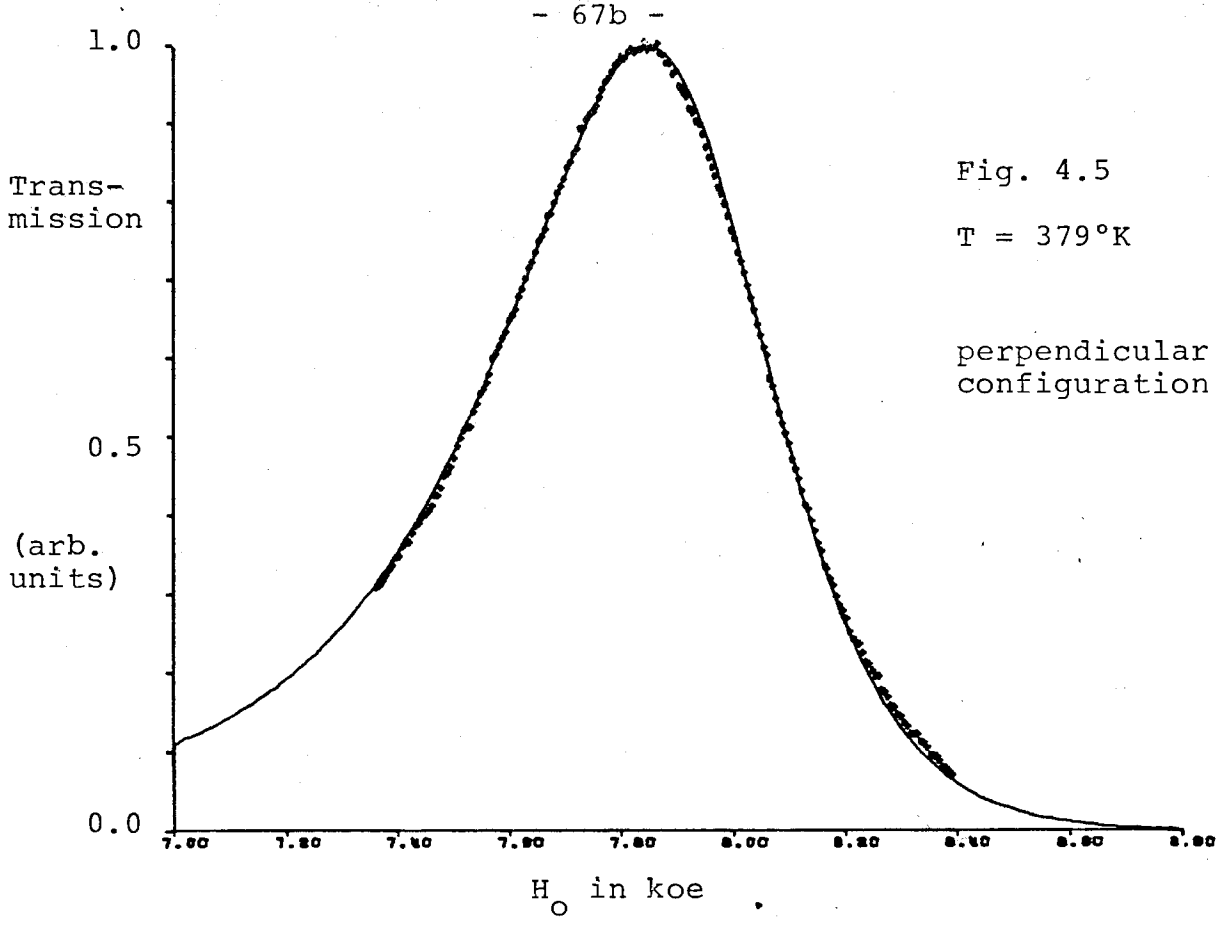

Fig. 4.5

T = 379°K

perpendicular configuration

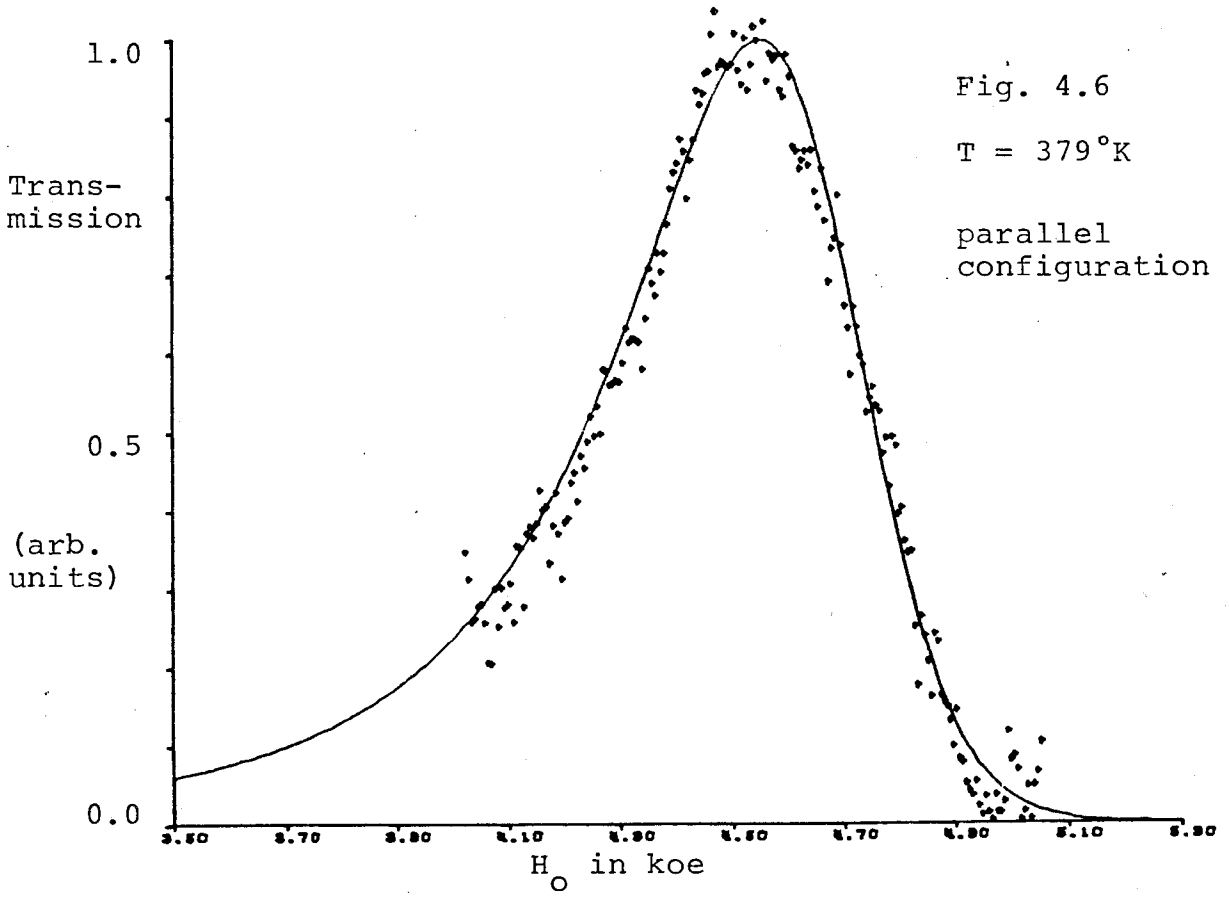

Fig. 4.6

T = 379°K

parallel configuration

excellent agreement with the result (3.1) $\rho = (125 \pm 7)\mu\Omega$cm obtained from the DC measurement. All the data were then fitted again; this time with the room temperature resistivity fixed and the resistivity for other temperatures obtained from the measured temperature dependence of ρ in Fig. 3.1.

Equation (2.54) suggests another method to determine ρ. According to this equation, the absolute peak transmitted amplitude is very sensitive to the ratio λ/ρ. In order to accurately calibrate the microwave system for absolute amplitude, a supermalloy specimen 100.6μm thick was used as a 'standard' sample. Supermalloy was used because it had been the subject of a previous study (Cochran et al. (1977a)) and hence its parameters were all known. In particular, because a large quantity of the material was available, one could easily determine d/δ to within 1% from external measurements. The supermalloy specimen was mounted on a diaphragm identical to the one used to mount the Co-P sample. Two room temperature, parallel configuration runs were made; one with the supermalloy sample and one with the Co-P sample. In addition to a slight adjustment of the cavity tuning rods, only the sample mounting screws (see Fig. 3.3) were disturbed between runs. The result obtained was:

$$\frac{\lambda}{\rho} = \frac{1.74 \times 10^{8}\,\text{sec}^{-1}}{124\mu\Omega\text{cm}} \pm 5\% \qquad (4.1)$$

where the major contributor to the 5% uncertainty was a 4% uncertainty in the damping parameter for supermalloy. Combined

with the fitting result (discussed below) for Co-P at room temperature in the parallel configuration, $\lambda = (1.70 \pm 0.03) \times 10^{8}\text{sec}^{-1}$, this yields $\rho = 121 \pm 8\mu\Omega\text{cm}$: a value which is in excellent agreement with the resistivity found by the previous two methods.

4.1 The Magnetic Damping Parameter

The results for λ obtained from fitting by the method described above are shown in Fig. 4.7. In general, changing λ by more than 2% in either direction resulted in noticeably worse agreement between experimental and calculated lineshapes*. To illustrate this point and also to give the reader a better feeling for the relation between λ and linewidth, the experimental points of Fig. 4.1 have been replotted in Fig. 4.8 along with calculated curves corresponding to values of λ separated by 3.6%.

One can see from Fig. 4.7 not only that λ is slighly temperature dependent but also that on average λ for the parallel configuration ($\lambda_{\parallel}$) is 2.5% larger than λ as deduced from the perpendicular configuration data ($\lambda_{\perp}$). This difference amounts to only 8 oe or ~1.5% of the linewidth. More compelling evidence for the conjecture that λ is both temperature- and configuration-dependent comes from the experimentally determined ratio of peak transmitted amplitude in the

* The values of λ deduced from data for which the signal to noise ratio was less than 30 had uncertainties of much larger than $\pm$ 2% and hence for the sake of clarity were not included in the graph Fig. 4.7.

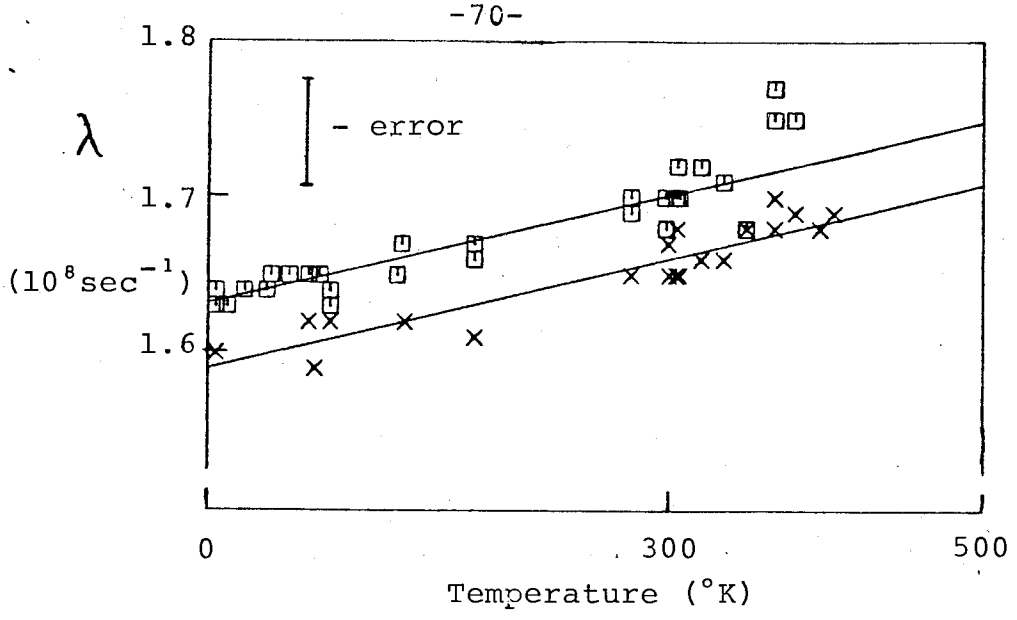

Fig. 4.7

The Landau-Lifshitz damping parameter, λ, as determined by curve-fitting the FMAR data, plotted as a function of temperature. Squares: λ as deduced from parallel configuration data. Crosses: λ as deduced from perpendicular configuration data. The indicated error bar applies to all the data points and amounts to ± 2%.

perpendicular configuration compared with the peak amplitude for the parallel configuration. This ratio is plotted versus temperature in Fig. 4.9*. On the same graph, corresponding theoretical curves for 3 cases have been plotted: (1) $\lambda_{||}$ and $\lambda_{\perp}$ are equal and depend linearly on temperature from $(1.61 \times 10^8)\ sec^{-1}$ at T = 0 to $(1.70 \times 10^8)\ sec^{-1}$ at T = 380° K (this is the least squares linear fit of $1/2\ (\lambda_{||} + \lambda_{\perp})$ vs. T);

*Actually, $4\pi M_S$ times the logarithm of $2^{3/2}$ times the ratio is plotted. This particular function was chosen because it is comparatively independent of temperature.

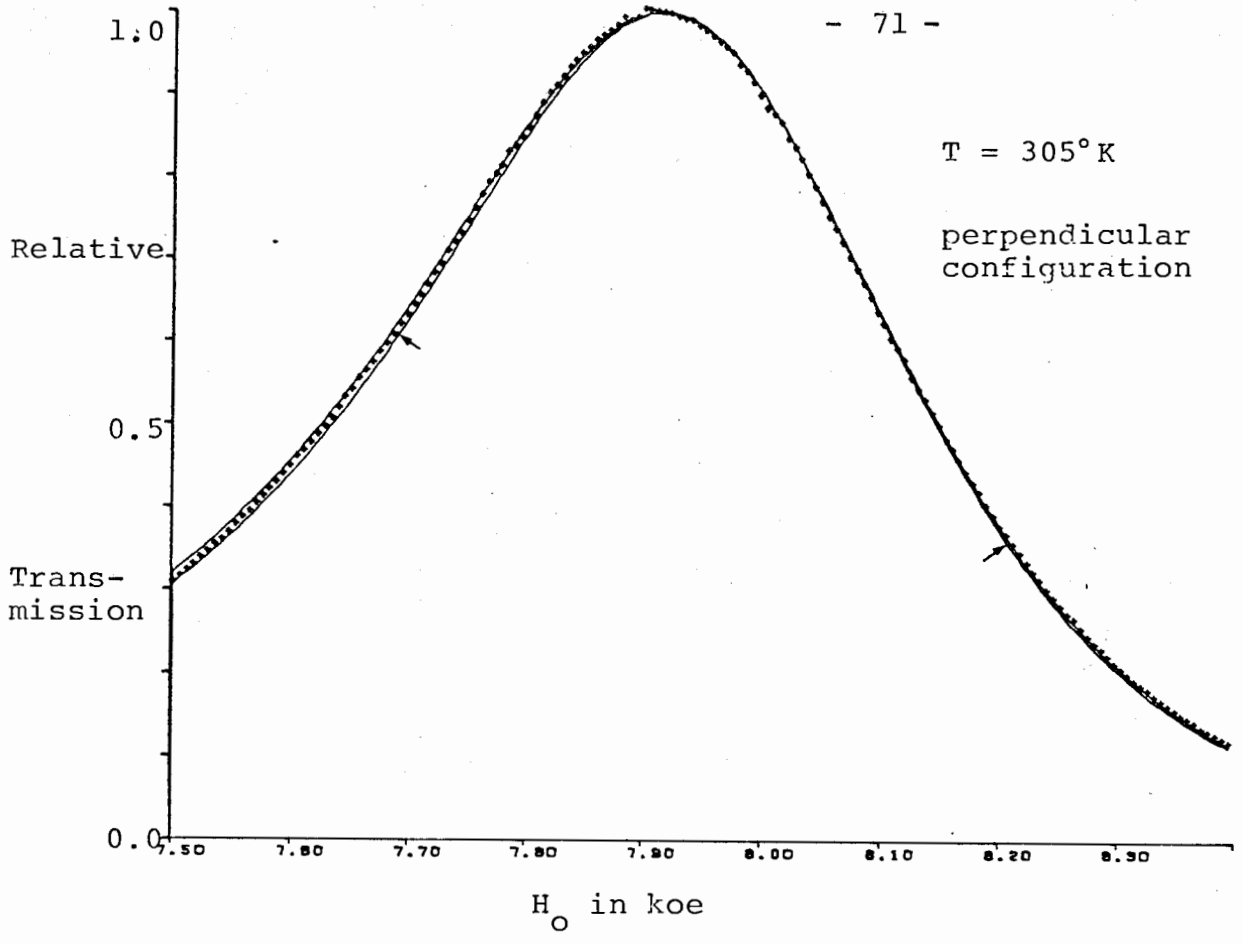

Fig. 4.8

This figure is identical to Fig. 4.1a except that the field scale has been expanded and there are calculated curves for two different values of λ. The narrower curve (indicated by arrors) was calculated using $\lambda = 1.62 \times 10^8$ sec^{-1} and the other curve was calculated using $\lambda = 1.68 \times 10^8 sec^{-1}$.

(2) $\lambda_{||} = (1.632 \times 10^8)$ sec^{-1} and $\lambda_{\perp} = (1.590 \times 10^8)$ sec^{-1}, both being independent of temperature (these are the values of λ extrapolated to T = 0°K); (3) $\lambda_{||} \neq \lambda_{\perp}$, the two values having been taken from the least squares linear fits to the data of Fig. 4.7. The superior agreement between experiment and the calculation for the third case is obvious, and, the discrepancies that do exist probably arise from the too-simple assumption that the relation between λ and temperature

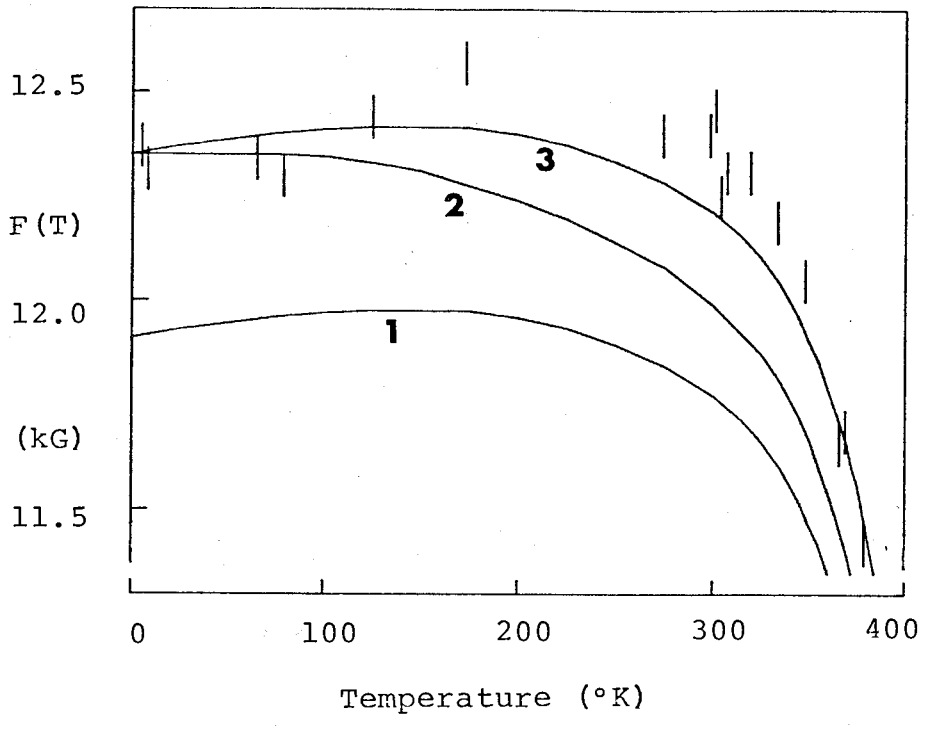

Fig. 4.9

Experimentally determined values of F(T) plotted versus T where $F \equiv 4\pi M_S \ln(2^{3/2} A_\perp / A_\parallel)$, A ≡ absolute transmitted amplitude at the FMAR peak in the perpendicular configuration ($A_\perp$) and in the parallel configuration ($A_\parallel$). Also plotted are calculated curves of F(T) for the following 3 cases: (1) $\lambda_\parallel$ and $\lambda_\perp$ are equal but depend linearly upon temperature from λ $1.61 \times 10^8 sec^{-1}$ at T = 0°K to $1.70 \times 10^8 sec^{-1}$ at T = 380°K. (2) $\lambda_\parallel \neq \lambda_\perp$ but the two damping parameters are independent of temperature; in particular, $\lambda_\parallel = 1.632 \times 10^8 sec^{-1}$ and $\lambda_\perp = 1.590 \times 10^8 sec^{-1}$. (3) $\lambda_\parallel \neq \lambda_\perp$ and both depend linearly upon temperature; in particular, $\lambda_\parallel = 1.632 \times 10^8 sec^{-1}$ at T = 0°K to $1.722 \times 10^8 sec^{-1}$ at T = 380°K while $\lambda_\perp = 1.590 \times 10^8 sec^{-1}$ at T = 0°K to $1.680 \times 10^8 sec^{-1}$ at T = 380°K.

is linear.

4.1a Other Forms of Damping

Had all the results been fitted using the Gilbert rather than the Landau-Lifshitz form of the damping term, the Gilbert parameter, G, would have been found to be numerically equal to the Landau-Lifshitz parameter, λ, to order $\alpha = \left(\frac{\lambda}{\gamma M_S}\right)^2$. This follows from equation (2.34):

$$\lambda = \frac{G}{1 + \left(\frac{G}{\gamma_G M_S}\right)^2}$$

The parameter α is less than 0.20% even for the smallest value of M_S obtained (M_S = 200 gauss at T = 414° K). Hence, these two different forms of the damping cannot be here distinguished. Using equation (2.30):

$$\left.\frac{\partial \vec{M}}{\partial t}\right|_{LL} = -\lambda\left(\frac{H_N}{M_S}\vec{m} - \vec{h}_\perp\right)$$

along with our knowledge that at FMAR the internal field, H_N, is $\omega/\gamma - 4\pi M_S$ (2.64) and that $\vec{h}_\perp = \vec{h} = -4\pi\vec{m}$, we find that at FMAR, the first order damping contribution to $\partial M/\partial t$ in the Landau-Lifshitz case is $-\lambda \frac{\omega/\gamma}{4\pi M_S}\vec{m}$. This, when compared with the Bloch-Bloembergen damping contribution, $-\vec{m}/\tau_1$ (2.35), immediately yields the correspondence

$$1/\tau_1 \longleftrightarrow \lambda \frac{\omega/\gamma}{4\pi M_S} \qquad (4.2)$$

In the temperature range studied, λ changed by less than 10% and ω/γ by less than 2% while $4\pi M_S$ ranged from 6.4 kG to 2.5 kG. Hence, analyzing all of the experimental data using only the Bloch-Bloembergen form of the damping mechanism will yield a damping parameter ($1/\tau_1$) which changes by a factor 2.5 over the temperature range studied. Therefore, the Bloch-Bloembergen form does not give as simple a description of the magnetic damping mechanism as do either the Landau-Lifshitz or the Gilbert forms.

4.2 The Saturation Magnetization

The results obtained for the saturation magnetization from curve-fitting are plotted in Fig. 4.10 and listed in Appendix B. As previously stated, it was impossible to make FMAR measurements above 414°K since at those temperatures the peak transmitted power fell below the noise level. Cochrane and Cargill (1974) have published $M_S(T)$ curves found from experiments performed on amorphous Co-P samples of various P concentrations. By adjusting the horizontal and vertical scales of Fig. 4.10, it was possible to superpose these data upon those of Cochrane and Cargill. In this manner, it was possible to extend the data of Fig. 4.10 beyond T = 414°K (dashed curve) and to determine a value of (460 $\pm$ 40)°K for

the Curie temperature. When compared with the results of Pan and Turnbull (1974), this Curie temperature suggests a phosphorus concentration in the sample of (24.6 $\pm$ 0.4) atomic %. Also, a comparison of low temperature magnetization values indicates that the composition of this sample was very similar to the one used by McColl et al. (1976) in their spin wave resonance experiments (25 $\pm$ 1 atomic % P).

FMAR runs in the parallel configuration were recorded at nine different temperatures below 80°K. It was the intention to use these runs in conjunction with the Bloch $T^{3/2}$ law to determine the spinwave dispersion coefficient, D. By being especially careful in calibrating the magnetic field and by reducing and correcting for effects of hysteresis caused by a finite apparatus time constant, it was possible to obtain FMAR lineshapes whose positions were uncertain to less than $\pm$ 2 oe. This coupled with an uncertainty of $\pm$ 2 oe in ω/γ from the perpendicular configuration FMAR line position yields a total uncertainty in $4\pi M_S$ of $\pm$ 4 oe. The experimental run of T = 12.5°K is plotted in Fig. 4.11. Also plotted in the same figure are theoretical curves calculated using (4π times) magnetizations differing by 8 gauss and which straddle the value $4\pi M_S$ = 6.4045 kG; the value which gave the best fit at 12.5°K.

The magnetization data below 80°K were fitted to the field dependent Bloch $T^{3/2}$ law (A. 7) derived by Argyle et al. (1963):

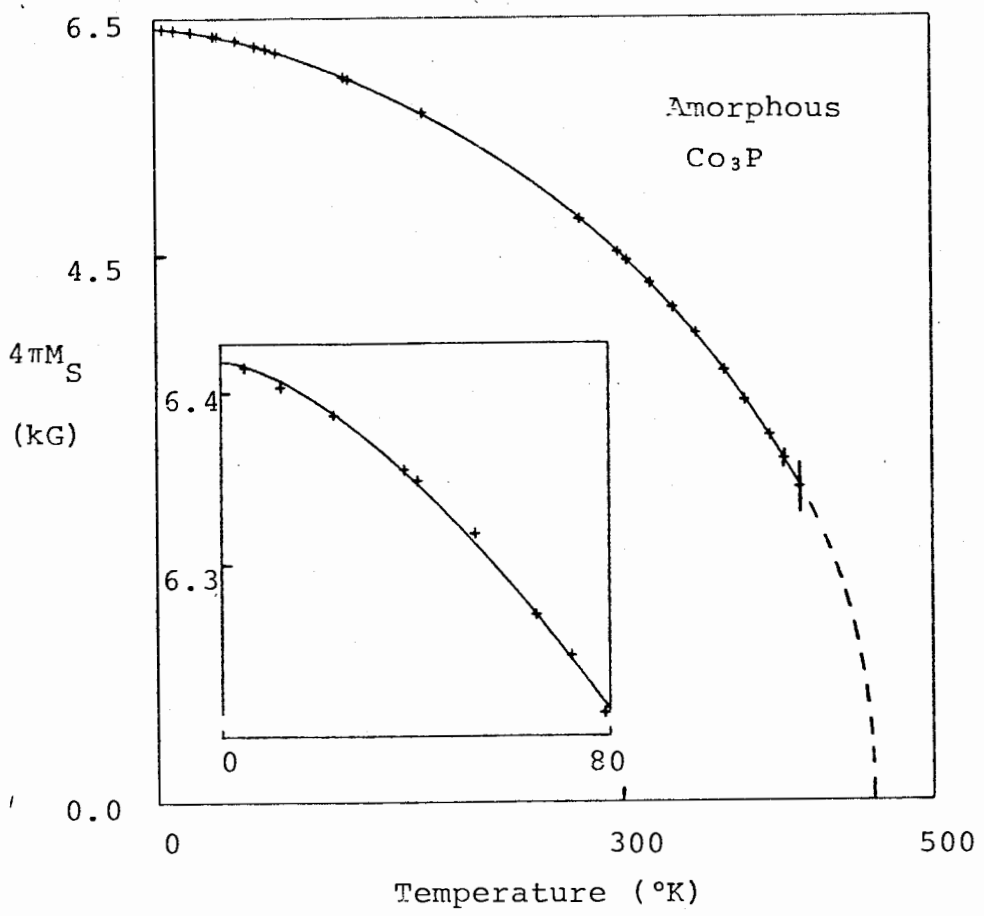

Fig. 4.10

Temperature dependence of $4\pi M_S$ deduced from curve-fitting the FMAR results. The solid curve is the interpolation of the data points.

Inset: the temperature variation of $4\pi M_S$ for low temperatures has been replotted on an expanded scale. In this case, the sizes of the experimental points correspond to the experimental uncertainty. Here, the solid curve is the best fit of the data to equation (4.3) (the $T^{3/2}$ law).

None of the plotted data have been corrected for anisotropy. The individual values of $4\pi M_S$ both with and without the assumption of the uniaxial anisotropy have been listed in Appendix B.

$$M_o - M_s(T) = g\mu_B \left(\frac{k_B T}{4\pi D}\right)^{3/2} G\left[\frac{g\mu_B(\omega/\gamma - 8/3\,\pi M_s)}{k_B T}\right] \quad (4.3)$$

where $G(x) \equiv 2.612 - 3.54\, x^{\frac{1}{2}} + 1.46\, x - 0.104\, x^2$.

(The expression used in (4.3) for the internal field is $\omega/\gamma - 4\pi M_S$; in accordance with the condition for FMAR (2.64).) In particular, a least squares linear regression analysis was performed on $M_S(T)$ versus $T^{3/2}G(x)$. This yielded

$$4\pi M_o = (6.419 \pm 0.004)\text{kG} \quad (4.4)$$

and the spinwave dispersion coefficient*

$$D = 113 \pm 4 \text{ meV } \mathring{A}^2 \quad (4.5)$$

This corresponds to an exchange stiffness constant $A = (2.33 \pm 0.08) \times 10^{-7}$ erg/cm. The fit obtained using these values of M_o and D had an rms error of 3.1 gauss; it is shown in the inset in Fig. 4.10. One can see that most of the experimental points lie on the fitted curve within experimental uncertainty.

---

*Neglecting the field dependence of M_S (i.e. setting $G(x) = 2.612$) changes D by ~ 5%.

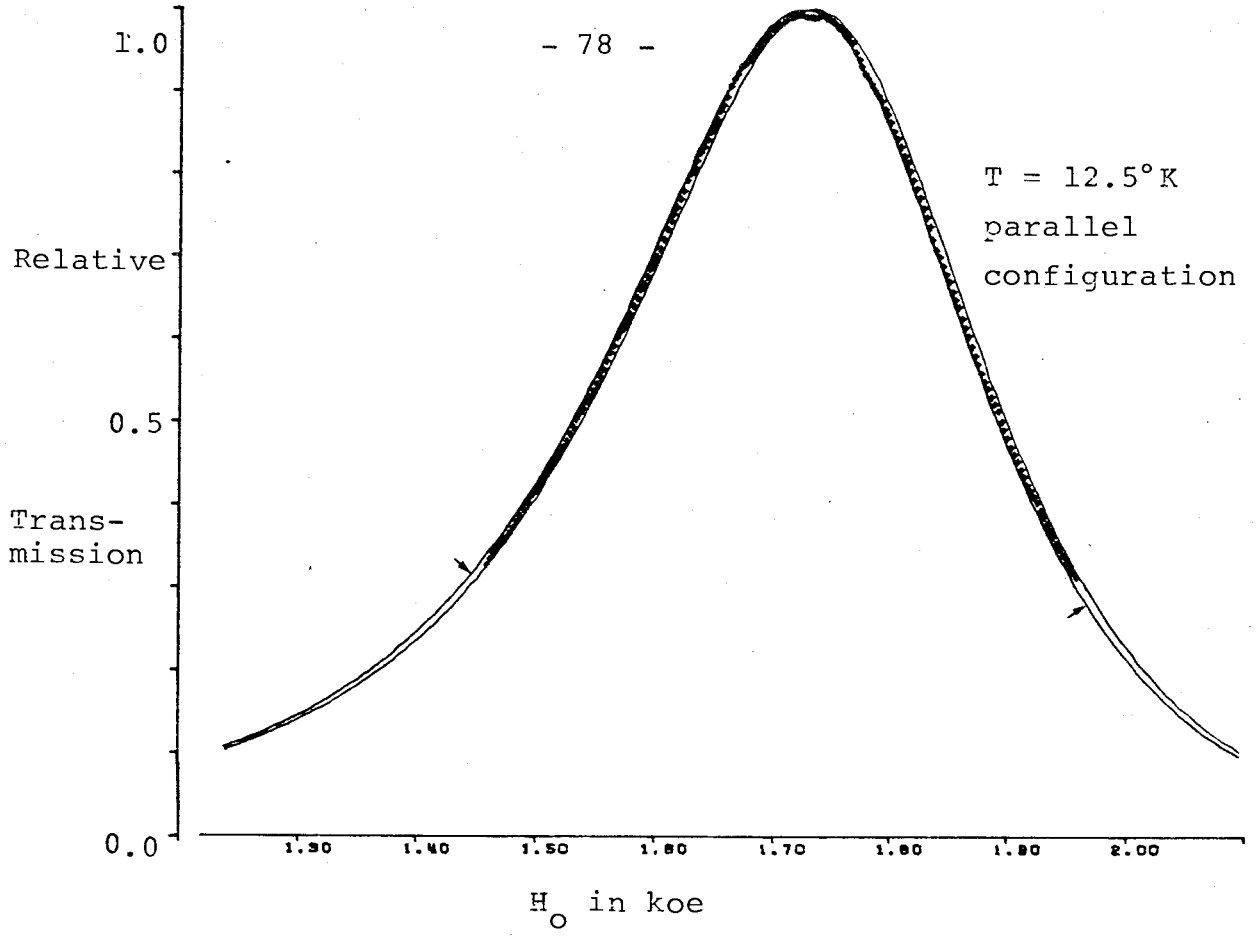

Fig. 4.11

Transmitted amplitude versus field for T = 12.5°K: a demonstration of the sensitivity of the calculated FMAR lineshape to variations in $4\pi M_S$. The two solid curves were calculated for $4\pi M_S$ = 6.4085 kG. (indicated by arrows) and $4\pi M_S$ = 6.4005 kG (rightmost curve). Other parameters had the values: ω/γ = 8.1035 koe and $\lambda = 1.63 \times 10^8 sec^{-1}$; ρ = 122.6 $\mu\Omega$cm, $\omega/2\pi$ = 23.953 GHz, and d, D_x and D_z are as in Fig. 4.1. The vertical scaling factor was again chosen for best fit.

4.3 The g-Factor

The values of the g-factor deduced from comparing the perpendicular configuration transmission data with calculations based on the Landau-Lifshitz equation of motion with the Landau-Lifshitz form of damping, and ignoring any anisotropy fields displayed a monotonic and reversible dependence upon

temperature. Values ranged from g = 2.11 at T = 5°K to g = 2.15 at 414°K (or, equivalently, with $\omega/2\pi$ = 24 GHz, the quantity ω/γ decreased by 150 oe as the temperature increased from 0 to 414°K). This is illustrated in Fig. 4.12; the individual values of g have also been listed in Appendix B.

It is possible that the g-factor of amorphous Co_3P is intrinsically temperature dependent; however, it will be argued in section 5.3 that this is extremely unlikely. It is more likely that the apparent temperature dependence of g is due to structural or compositional inhomogeneities which give rise to a magnetization dependent anisotropy field for, in this case, the perpendicular configuration FMAR peak is shifted down in field by H_A, the anisotropy field (see equation (2.73)). In order to test the proposed anisotropy, FMAR runs were made for 3 different positions of rotation of the sample about its normal. (Refer to Fig. 3.3.) The resulting FMAR lineshapes were found to be shifted from each other by less than 7 oe. If one compares this with the 150 oe change in ω/γ over the temperature range 5 - 414°K, one must conclude that any anisotropy, if present, is predominantly uniaxial; the axis being the specimen normal. Furthermore, this type of anisotropy would not be surprising since the specimen normal was also the electrodeposition growth axis.

4.3a The FMR Results

If, as in section 2.2.4, we write the anisotropy energy as $E_A = K \sin^2\theta$ where θ is the angle between $\vec{M}$ and the sample

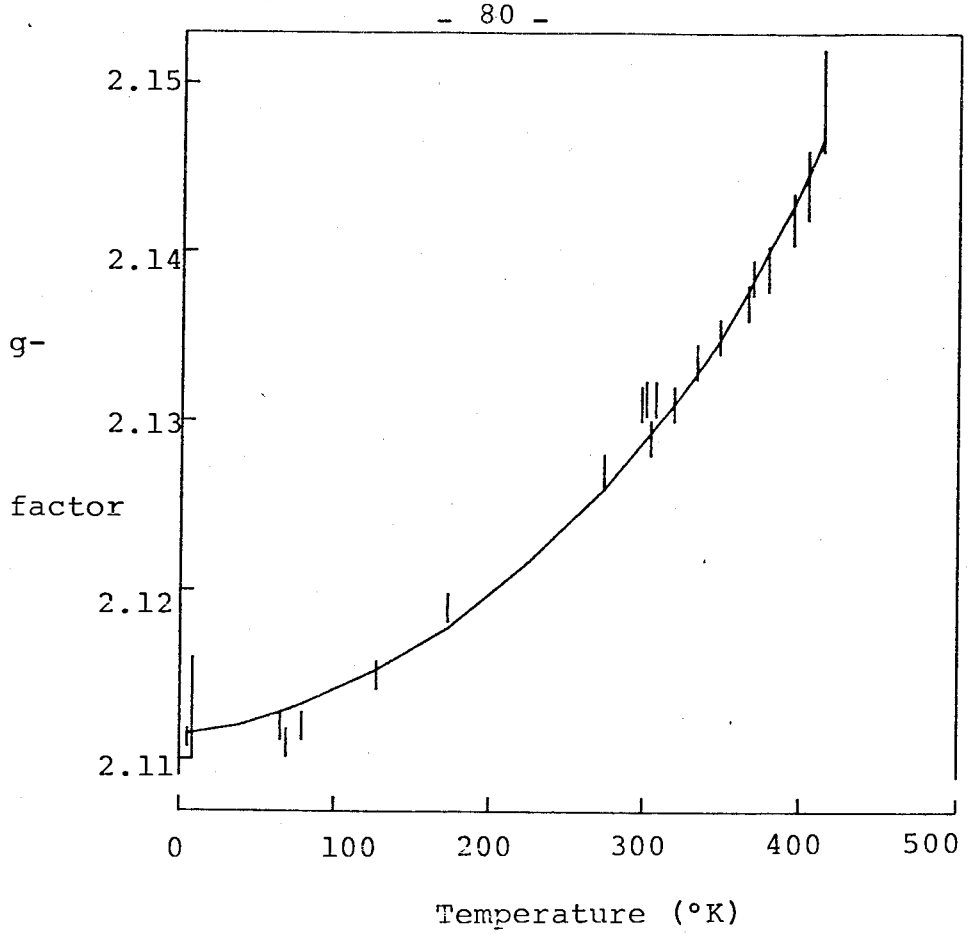

Fig. 4.12

The apparent temperature dependence of the g-factor as deduced from curve fitting using the Landau-Lifshitz form of the damping and assuming no magnetic anisotropy. Values obtained for the g-factor are < 0.2% larger if the Gilbert rather than the Landau-Lifshitz form is used to analyze the experimental data.

The g-values from which this graph has been plotted are listed in Appendix B.

normal, and define an anisotropy field, $H_A = 2K/M_S$, then the new FMAR conditions are ((2.71) and (2.74)):

$\perp$ FMAR: $\omega/\gamma = H_o + H_A$

$\parallel$ FMAR: $(\omega/\gamma)^2 = (H_o + 4\pi M_S)(H_o + 4\pi M_S - H_A)$

$$\text{or } \omega/\gamma = H_o + 4\pi M_S - 1/2\ H_A$$

$$\text{for } H_A << H_o + 4\pi M_S$$

With the inclusion of an additional parameter, H_A, it is no longer possible to uniquely determine g and M_S from the FMAR data. In order to lift this indeterminacy, ferromagnetic resonance (FMR) abosrption experiments were carried out on the same sample at room temperature and frequencies of 9 and 24 GHz. The conditions for FMR to occur in an infinite disc with uniaxial anisotropy are ((2.70) and (2.73)):

$$\perp \text{ FMR:} \quad \omega/\gamma = H_o - (4\pi M_S - H_A)$$

$$\| \text{ FMR:} \quad (\omega/\gamma)^2 = H_o \left[H_o + (4\pi M_S - H_A) \right]$$

It is obvious, then, that one can uniquely determine the g-factor and $4\pi M_S - H_A$ by performing FMR measurements in both configurations. It was shown in section 2.2.2a that at FMR, the microwaves do not penetrate very deeply into the sample (< 1 μm in the present case) and that therefore FMR experiments yield information only about the surface of the sample. FMR absorption measurements were consequently made on first one side of the specimen and then the other side to test the sample homogeneity.

The parameters obtained by matching the calculated line-

width (the separation between inflection points of the absorption versus field plot) and line-position to the experimentally measured values are shown in Table 4.1. The calculations were made assuming the Landau-Lifshitz form of damping. Owing to the comparatively small value of the exchange parameter, A, inferred from the magnetization data*, the calculated FMR lineshapes were not very sensitive to the surface pinning condition. Specifically, full pinning broadens the linewidth by $\lesssim 10$ oe (see equation (2.48)) and shifts the line position by $\lesssim 7$ oe when compared with the case of no pinning. These considerations contribute a $\pm 3\%$ uncertainty in λ and contribute less than $\pm 0.1\%$ to the uncertainty in g.

One can see from Table 4.1 that the values of λ needed to explain the observed FMR linewidths were significantly larger than the values found from FMAR. Furthermore, they were not the same for each side of the sample, nor even for each configuration. Bhagat et al. (1966) and, more recently, our research group (Heinrich et al. (1977)) have observed a correlation between FMR linewidth and surface roughness. A less than perfect surface gives rise to a distribution in

*At room temperature, A is expected to be significantly smaller than it is at low temperatures. In particular, McColl et al. (1976) found the room temperature value to be one half the low temperature result. For this reason, $A = 1.2 \times 10^{-7}$ erg/cm was used here.

Table 4.1

The properties of amorphous Co_3P as deduced from room temperature FMR measurements. These values should be compared with the FMAR reuslts:

$$4\pi M_S - 3/2\ H_A = (4.520 \pm 0.020)\text{kG}$$

$$\lambda_{\parallel} = 1.68 \times 10^8 \text{sec}^{-1}$$

$$\lambda_{\perp} = 1.64 \times 10^8 \text{sec}^{-1}$$

Also, from spin wave resonance, McColl et al. (1976) found:

$$g = 2.125 \pm 0.007$$

freq. (GHz)	side of sample	g-factor	$4\pi M - H_A$ (kG)	$\lambda_{\parallel}$ (10^8sec^{-1})	$\lambda_{\perp}$ (10^8sec^{-1})
9.1045	dull side	2.124 ±.003	4.600 ±.020	2.10 ±.15	3.00 ±.25
	shiny side	2.122 ±.003	4.452 ±.020	2.00 ±.15	2.50 ±.15
23.970	dull side	2.123 ±.002	4.613 ±.020	1.90 ±.10	2.30 ±.15
	shiny side	2.125 ±.002	4.460 ±.020	1.85 ±.10	1.85 ±.10

local demagnetizing fields and also - and this is most severe in the case of the perpendicular configuration - to a distribution in magnetization direction. The conjecture that sample surface roughness was responsible for the FMR line broadening indicated by the values of λ in Table 4.1 is supported by the

following three observations: (1) The shiniest surface gave the narrowest lineshape. (2) The lineshapes were broader for the perpendicular configuration than for the parallel configuration. (3) The data taken at the higher frequency (where the FMR condition ((2.61) and (2.62)) demands larger applied fields and a larger applied field causes less distribution in magnetization direction) gave smaller apparent λ's.

The values of $4\pi M_S - H_A$ as deduced from FMAR at the two frequencies agreed within experimental error* for a particular surface, but values for the two surfaces differed by ~ 150 oe. (This is of the same order of magnitude as the expected size of the anisotropy field.) It is not known whether this difference corresponds to a discrepancy in M_S or in H_A. A gradient in either M_S or H_A through sample thickness would, by 'smearing out' the FMAR conditions ((2.71) and (2.74)) significantly broaden the FMAR lineshapes. In particular, such a gradient in H_A would broaden the FMAR lineshape for the perpendicular configuration by 150 oe but, because of the nature of the condition for FMAR (2.74), it would broaden the lineshape in the parallel configuration by only one-half of this amount. This would result in a discrepancy between $\lambda_{\parallel}$ and $\lambda_{\perp}$ corresponding to a difference in linewidth of 75 oe. Recall that only an 8 oe discrepancy was observed. The

---

* One must realize that the uncertainty ± 1 degree in temperature causes an additional uncertainty ± 10 gauss in $4\pi M_S$. (See Fig. 4.10.)

possibility of a gradient in M_S can be dismissed in a similar manner. It can easily be shown for the perpendicular configuration that in the presence of such a gradient in M_S, the local demagnetizing field is still equal to negative 4π times the local magnetization and hence the FMAR condition $H_N = \omega/\gamma - 4\pi M_S$ still translates into $H_o = \omega/\gamma$ and the lineshape is not broadened. In the parallel configuration, however, there is no demagnetizing field and the FMAR lineshape is expected to be broadened by the variation in $4\pi M_S$, namely by 150 oe. The observed difference between $\lambda_{||}$ and $\lambda_{\perp}$ from FMAR allows a variation in $4\pi M_S$ through the sample thickness of only 8 oe. One must, therefore, conclude that the values of $(4\pi M_S - H_A)$ as found from FMR apply only to the sample surfaces and not to the bulk. This is unfortunate because it was hoped that by comparing the values of $(4\pi M_S - H_A)$ from FMR with those of $(4\pi M_S - 3/2\ H_A)$* from FMAR, some idea of the absolute magnitude of H_A could be deduced.

The fact that the g-factors found from FMR in Table 4.1 all agree with each other and with the result of McColl et al. (1976) indicates that whatever caused $4\pi M_S - H_A$ to be different

---

*This expression arises because if no anisotropy is assumed, then $4\pi M_S$ is obtained by subtracting the parallel configuration FMAR field from that of the perpendicular configuration. If this procedure is applied to the uniaxial anisotropy case, equations (2.71) and (2.74 b) yield $4\pi M_S - 3/2\ H_A$.

at each surface did not affect the g-factor. It is, therefore, reasonable to assume that the value $g = 2.124 \pm 0.002$ from Table 4.1 represents the intrinsic bulk value of the g-factor. If we further make the reasonable assumption that the intrinsic g-factor is temperature independent, we can use it along with the data of Fig. 4.12 to find H_A as a function of temperature. When plotted versus $4\pi M_S$ rather than temperature, it is found (Fig. 4.13) that H_A decreases linearly with M_S and goes through zero at $4\pi M_S \approx 5.1$ kG ($\sim 200°K$).

4.3b Effect of Other Forms of Damping on the Values of H_A

With reference to Table 2.1, one can see that the use of the Bloch-Bloembergen rather than the Landau-Lifshitz form of damping would not change the above conclusions about H_A. In the Gilbert damping case, however, equation (2.34) asserts that the resonance and antiresonance line positions are slightly damping-dependent. This changes the detailed findings for H_A versus $4\pi M_S$ only slightly. In particular, the g-factor found from the room temperature FMR measurements must be multiplied by the factor $1 + \left(\frac{\lambda}{\gamma M_S}\right)^2$ and hence (using the FMAR value of λ and, of course, the room temperature value of M_S) becomes $g = 2.125 \pm .002$. This decreases ω/γ by 5 oe and hence decreases H_A (at all temperatures) by 5 oe. Also, for Gilbert damping the calculated FMAR transmission line in perpendicular configuration is shifted upward in field by an amount $\omega/\gamma \left(\frac{\lambda}{\gamma M_S}\right)^2$ and therefore the apparent anisotropy field is increased by the same amount. This turns out to be,

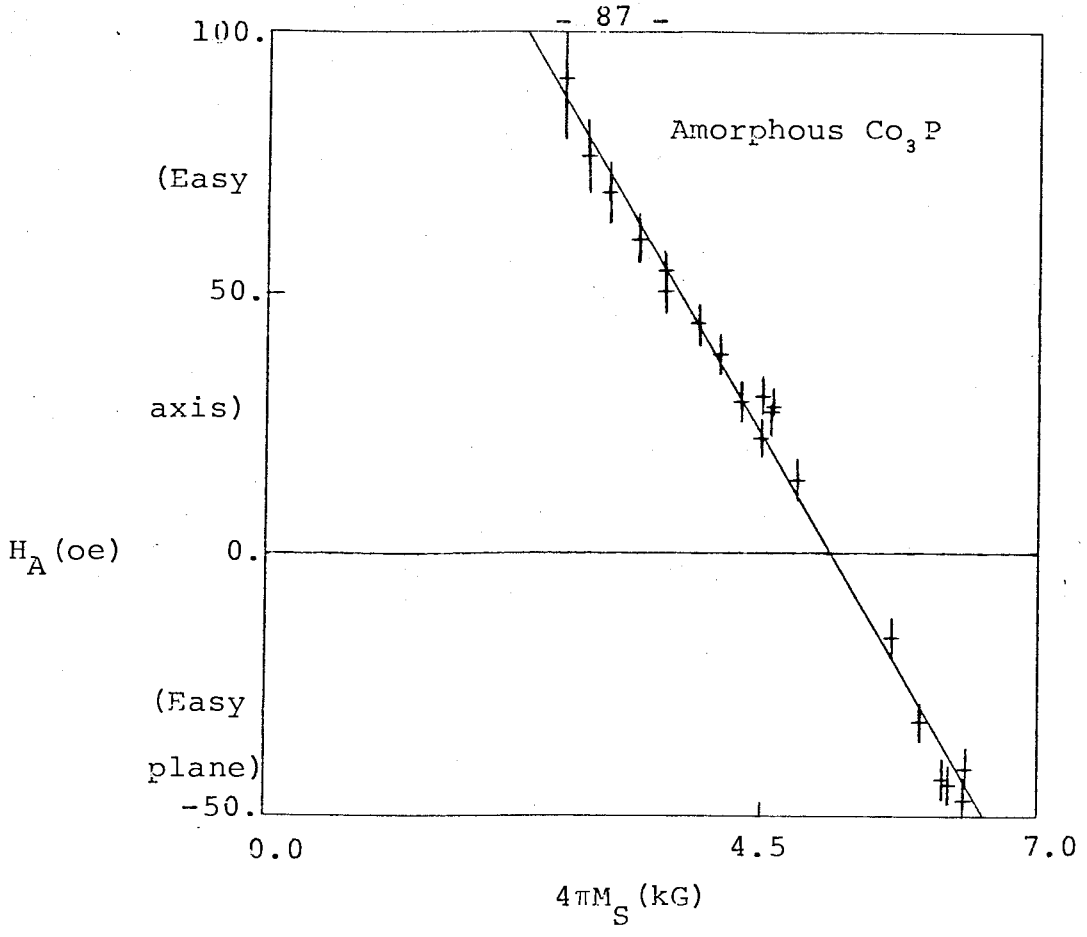

Fig. 4.13

Uniaxial anisotropy field versus $4\pi M_S$ as deduced from the perpendicular FMAR line position combined with the value g = 2.124 ± 0.002 obtained from FMR. The systematic ∓8 oe uncertainty arising from the uncertainty in this g-factor has not been included in the error bars of the data points. The 'least squares' linear fit to the data has also been plotted. The experimental values used to plot this graph are listed in Appendix B.

for example, 16 oe at $4\pi M_S$ = 2.5 kG and 2.5 oe at $4\pi M_S$ = 6.4 kG. The net effect of analyzing the data with the Gilbert rather than the Landau-Lifshitz form of damping, therefore, is to shift the apparent anisotropy field by a small magnetization-dependent amount. This amount is only 11 oe at the highest temperature for which FMAR data was recorded and decreases to

- 2.5 oe at 0°K. Such a shift is insignificant in that it does not change the conclusion that H_A changes linearly with $4\pi M_S$.

4.3c Effect of Anisotropy on the Values of $4\pi M_S$

One complication arising from the presence of anisotropy is that the quantity which was used as $4\pi M_S$ in section 4.2 is actually the quantity $4\pi M_{eff} = 4\pi M_S - 3/2\ H_A$ (see footnote p. 90). The magnetization dependence of the anisotropy field is given by

$$H_A = H_{Ao} - 4\pi\alpha M_S \tag{4.6}$$

where $\alpha = 0.036 \pm 0.002$ and $H_{A0} = 186 \pm 8$ oe (from Fig. 4.13). It follows that both M_o and the coefficient of $T^{3/2}$ in equation (4.3) should be corrected since

$$4\pi M_S = 4\pi M_{eff} + 3/2\ H_{Ao} - 3/2\alpha\ 4\pi M_S \tag{4.7}$$

The corrected values are

$$4\pi M_o = 6.355 \pm 0.020 \text{ kG} \tag{4.8}$$

$$D = 117 \pm 4 \text{ meV } \mathring{A}^2 \tag{4.9}$$

A table of the values of $4\pi M_S$ deduced for amorphous Co_3P

assuming the internal anisotropy field given by equation (4.6) is presented in Appendix B.

CHAPTER 5

DISCUSSION

5.1 The Magnetic Damping Parameter

The damping parameter deduced using the Bloch-Bloembergen form of the damping contribution to $\partial\vec{M}/\partial t$ was found to be strongly temperature dependent while that deduced using the Landau-Lifshitz (or the Gilbert) form was only weakly dependent on temperature. This observation suggests that the Landau-Lifshitz form is more fundamental than the Bloch-Bloembergen form. A similar conclusion was reached by Dewar et al. (1977) from FMAR measurements on nickel made between 370 and 637°K.

There is no a priori reason to expect λ to be independent of temperature or configuration. Indeed, since the spinwave dispersion relation (equation A.6) is dependent on both the magnitude and direction of the magnetization, one would expect λ to show such a dependence. (This is because of the variation of the density of final scattering states into which a magnon can be scattered.) This argument would, of course, only apply for damping due to magnon-magnon scattering. In a case such as the present one - where λ is only slightly dependent upon temperature and configuration - one can therefore conclude that this mechanism makes at most only a very small contribution to the total damping. Besides the magnon-magnon interactions, there are many other processes which can lead to spin relaxation in ferromagnets; for instance, magnon-phonon

processes like those proposed by Kasuya and Le Craw (1961). But even these mechanisms cannot be expected to give rise to a relaxation frequency as large as the value $\sim 10^8 sec^{-1}$ observed in metals (Table 5.1).

It is generally (and plausibly) conceded that the relaxation of magnetic disturbances in metals occurs predominantly by means of interactions between spinwaves and conduction electrons*. One of the most important of these interactions is the exchange interaction between the electrons responsible for the ferromagnetism and the conduction electrons. Turov (in Vonsovskii (1966), chapter 5), for example, showed that indeed this interaction can be expected to result in relaxation frequencies as large as $\sim 10^9 sec^{-1}$. The foregoing suggests the possibility that the observed ($\sim 5\%$) change in λ (Fig. 4.7) for Co_3P over the temperature range studied is somehow related to the 2.5% change in the conductivity (Fig. 3.1) over the same temperature range. There are 3 reasons why this explanation is not likely. (1) The measured Landau-Lifshitz damping parameters of ferromagnetic metals whose resistivities differ by an order of magnitude can be within a factor of 2 of each other. Conversely, materials with very similar structures, compositions and values of resistivity can have damping parameters which differ by as much as a factor of

*This type of damping is not be be confused with the eddy-current damping which has already been taken into account in the boundary value problem. (See section 2.1.6.)

2. See Table 5.1. (2) Dewar et al. (1977) concluded that for nickel, the Landau-Lifshitz damping parameter was independent of temperature over the range 30 - 360°C while over this same range the resistivity changed by more than a factor of 3. (3) Explaining the temperature variation of λ as being due to the temperature variation of ρ still does not account for the result that the damping parameter as deduced from the perpendicular configuration data was not equal to that deduced from the parallel configuration data.

Kambersky (1976) has shown that the decay of spin waves in metals can be explained in terms of the spin-orbit coupling torques. In particular, he was able to explain the main qualitative features of the temperature dependence of λ observed in nickel. One can crudely gauge the strength of the spin-orbit interaction by the amount with which the observed g-factor differs from the free electron value. Referring to Table 5.1, one can see that despite widely differing resistivities, there appears to be a correlation between λ and g ($\lambda \sim (g - 2) \times 10^9 sec^{-1}$). This observation lends support to the approach of Kambersky.

As has been already stated, magnetization dependent damping is possible through the mechanism of magnon-magnon scattering. Let us assume that the intrinsic magnetic damping parameter of ideally homogeneous and structurally random Co-P is independent of temperature and that the slight temperature dependence observed in the present case is due to small

Table 5.1

Summary of the results of other workers for the damping parameter, λ, and the g-factor of various ferromagnets showing the lack of any strong correlation between λ and ρ, and, on the contrary, a significant correlation between λ and g.

Material	Structure	Method	ρ ($\mu\Omega$cm)	λ $10^8 sec^{-1}$	g	Reference
Fe	Crystalline	FMR	10	~0.7	2.09	1
Ni	Crystalline	FMR	7	2.3	2.22	1
Ni	Crystalline	FMAR	10 to 30	2.5	2.19	2
Supermalloy	Crystalline	FMAR	60	1.0	2.11	3
Metglas 2826	Amorphous	FMAR	150	0.9	2.05	4
Metglas 2826	Amorphous	FMR	150	<1.4	2.07	5
Metglas 2826A	Amorphous	FMR	150	1.7	2.16	5
Metglas 2826B	Amorphous	FMR	150	0.8	2.10	5
Co_3P	Amorphous	FMAR	124	1.65	2.12	This work.

References:
(1) Bhagat et al. (1966).
(2) Dewar et al. (1977).
(3) Cochran et al. (1977a).
(4) Cochran et al. (1977).
(5) Bhagat et al. (1977).

independently scattering inclusions of magnetization M_S' present in the sample in an amount corresponding to a volume fraction β. (This particular model is not completely arbitrary - as will be seen in section 5.3.) Magnetization inhomogeneities encourage 2-magnon processes (whereby one magnon is destroyed and another of equal energy but different $\vec{k}$ is created) by not

demanding the conservation of magnon momentum. Sparks ((1964), chapter 5) has treated the case of 2-magnon scattering from independent, spherical voids ($M_S' = 0$) by using quantum-mechanical transition-probability theory. He found that the contribution of this process to the FMR linewidth is proportional to $4\pi M_S \beta$; the proportionality constant being of order unity. In view of the naive hand-waving argument given below, this result is not very surprising. Inclusions of magnetization M_S' can be expected to give rise to stray fields which are of the order of $4\pi|M_S - M_S'|\beta$ in size and which occupy a volume of the order of the volume of the inclusions. This will effectively make the internal field uncertain to about $\delta H \equiv 4\pi|M_S - M_S'|\beta$ and result in a smearing of the FMAR (or FMR for that matter) lineshape by this amount.

Assuming that M_S' is not as strongly temperature dependent as M_S, this picture is consistent with the measured temperature dependence of λ only if $M_S' > M_S$. It has already been concluded in relation to the proposed anisotropy that the structure of the sample is symmetric about the sample normal. Hence, the proposed inclusions, if not spherical, are (on average) spheroidal - the symmetry axis, of course, being the sample normal. It remains to be seen whether the inclusions are prolate or oblate. For needle-shaped (prolate) inclusions, one would expect larger stray fields (and hence broader lines and larger apparent λ's) for the parallel configuration than for the perpendicular configuration. Hence, one would expect

$\lambda_{||} > \lambda_{\perp}$ if the inclusions are needle-shaped. Conversely, oblate inclusions would imply $\lambda_{\perp} > \lambda_{||}$. The experimental result that $\lambda_{||} > \lambda_{\perp}$, therefore, supports the prolate case.

On the basis of this model, an estimate of the volume fraction that the inclusions occupy can be obtained as follows. Over the temperature range studied, λ changed by $\sim 6\%$. This corresponds to a line-width change of ~ 20 oe. Assuming that M_S' is relatively independent of temperature, it follows that $4\pi|M_S - M_S'|$ changed by ~ 4000 gauss over the temperature range studied. This would be expected to lead to a change in δH of $\sim \beta(4000)$ oe. Equating this to the observed change in λ of ~ 20 oe leads to the order of magnitude estimate $\beta \sim 0.005$. Taking the cube root of this number yields the result that the inclusions are separated by ~ 10 times their diameter. This lends credence to the assumption that the inclusions are far enough apart to be essentially non-interacting.

Another consequence of the above model is that the actual intrinsic λ for amorphous Co_3P could be as small as 1.4×10^8 sec^{-1}. This follows from the assumption that the inclusions are pure cobalt ($4\pi M_S' = 17$ kG). Pure cobalt inclusions would produce the largest stray fields and, therefore, the largest extrinsic line broadening.

5.2 The Saturation Magnetization

The magnetization data of Fig. 4.10 have been corrected for anisotropy and replotted in Fig. 5.1 along with the known magnetization curve of nickel. Comparison of the two curves

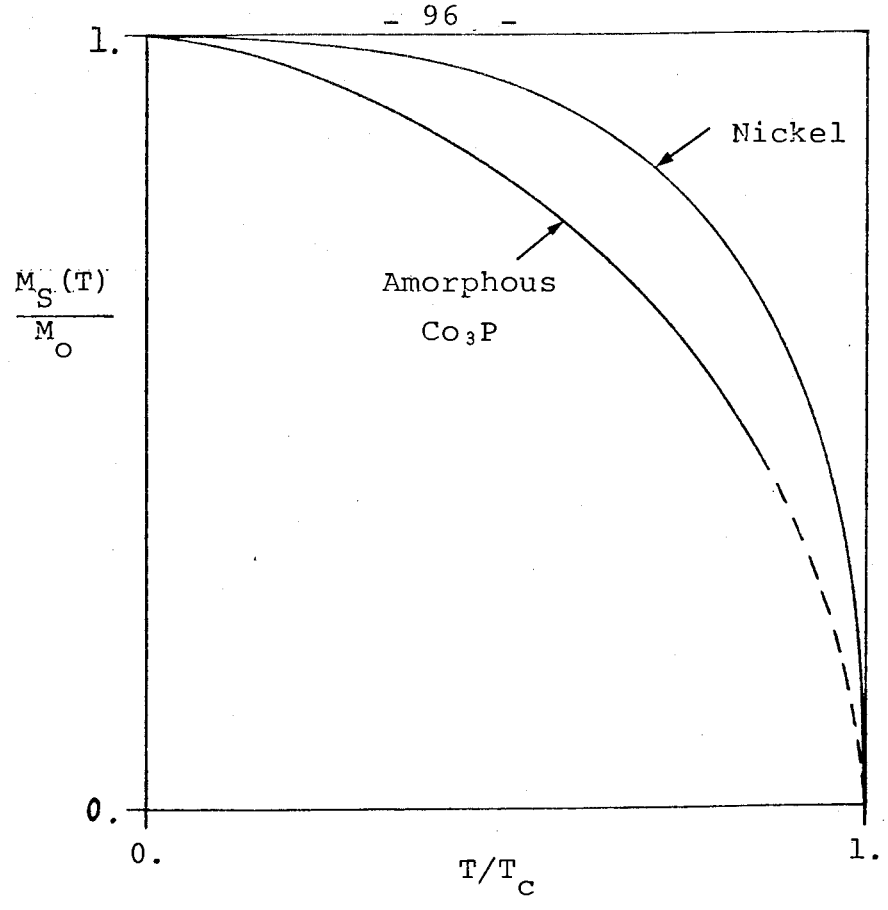

Fig. 5.1

The experimentally determined magnetization curve of amorphous Co_3P (from Fig. 4.10) has been plotted using normalized scales of magnetization and temperature. For purposes of comparison, the magnetization curve for polycrystalline nickel (Weiss and Forrer (1926)) has also been plotted here.

points up to what seems to be a characteristic feature of amorphous ferromagnets. Namely, that when the reduced magnetization ($M(T)/M_o$) is plotted versus the reduced temperature (T/T_c), the results for amorphous materials consistently fall below those of any typical crystalline system. (See Cochrane and Cargill (1974) and references therein.) Handrich and Kobe (Handrich (1969), Handrich and Kobe (1970)) modified

the mean field theory for amorphous ferromagnets by omitting lattice periodicity in the Hamiltonian and introducing a parameter representing the mean square fluctuation of the strength of the exchange interaction between two nearest-neighbour spins. While achieving the desired flattening of the M vs. T curve, the agreement with experiment was still only qualitative. (See Pan and Turnbull (1974).)

The comparatively rapid drop in magnetization with temperature for amorphous ferromagnets at low temperatures is not necessarily symptomatic of a small spin wave dispersion coefficient, D; for, in that case, one would also expect a low Curie temperature. What this means is that the distinguishing feature of amorphous ferromagnets is not so much the smallness of D, but rather the size of the dimensionless parameter $B_{3/2}$ defined by writing the $T^{3/2}$ law in the form

$$\left[M_o - M(T)\right] / M_o = B_{3/2}(T/T_c)^{3/2} \qquad (5.1)$$

For crystalline ferromagnets, $B_{3/2}$ is typically 0.12 while for amorphous ferromagnets it is 3 or 4 times larger than this value. (See Chien and Hasegawa (1977).) Working backwards from the value D = 117 meV $\mathring{A}^2$ for the present specimen yields

$$B_{3/2} = 0.45 \pm 0.06 \qquad (5.2)$$

(The large uncertainty is due to the uncertainty in T_c.) For

many purposes (Cargill (1975)), one can use macroscopic hard spheres randomly packed in a dense structure as an adequate model (the DRPHS model) of an amorphous material. By applying a Heisenberg model of localized spins to such a structural model, Krey (1978) has calculated that $B_{3/2} = 0.59$* for the spin quantum number $S = 1/2$ and $B_{3/2} = 0.51$* for $S = 1$; in reasonable agreement with (5.2). It is interesting that a calculation of $B_{3/2}$ for the crystalline fcc case also yields values of ~ 0.5 - significantly larger than the observed values (~ 0.1). What this all means is that the amorphous ferromagnets are much better described by a model of localized spins than are the crystalline ferromagnetic metals.

Shown in Table 5.2 are values of the spin wave dispersion coefficient, D, deduced from the data of other researchers. Typically, the low temperature magnetization measurements were performed between 1 and 100°K. Assuming that $D \sim 100$ meV $\mathring{A}^2$, the thermal magnons were characterized by wavenumbers in the range $0.03\ \mathring{A}^{-1} \lesssim k \lesssim 0.3\ \mathring{A}^{-1}$. The spin wave resonance experiments were performed on specimens whose thicknesses were $\sim 2000\ \mathring{A}$. Standing spin wave modes of up to order 10 were observed and this corresponds to a wavenumber range $0.003\ \mathring{A}^{-1} \lesssim k \lesssim 0.03\ \mathring{A}^{-1}$. In the neutron diffraction experiment, D was measured using momentum transfers in the range $0.01\ \mathring{A}^{-1} \lesssim k$

* These figures were found by Krey to vary by approximately 25% depending upon the functional form that he assumed for the exchange integral $J(r)$.

Table 5.2

Values of the spin wave dispersion coefficient, D, for Co-P as found by other researchers using various phosphorus concentrations.

Phosphorus Concentration (%)	D (meV Å)	Measurement Method	Measurement Temperature (divided by T_c)	Reference
19	134±5	M(T)	0 - 0.1	Cochrane and Cargill (1974)
20.3	115±5	M(T)	0 - 0.1	
22	126±5	M(T)	0 - 0.1	
23.6	103±5	M(T)	0 - 0.1	
25	128±3	M(T)	0 - 0.3	
	138±5	SWR	0.01	McColl et al. (1976)
	132±5	SWR	0.17	
	94±5	SWR	0.67	
24.6	117±4	M(T)	0 - 0.17	Present work.
20	185	ND	0.46	Mook et al. (1975).

Measurement methods: M(T), low temperature magnetization;
SWR, spin wave resonance;
ND, neutron diffraction for wavenumber $k \lesssim 3.0 \times 10^6 cm^{-1}$.

$\lesssim 0.03$ Å^{-1}. It is obvious from all the magnetization-type measurements that the value of D is not very sensitive to phosphorus content. This is reasonable for it has been found by X-ray measurements (Chi and Cargill (1976)) that the mean

nearest neighbour Co-Co distance does not depend strongly on phosphorus content. It is, therefore, fair to compare the value of D obtained in the present study with the value obtained by Mook et al. (1975) using neutron diffraction. There is obviously a significant discrepancy. Similar disagreements have been found in other amorphous ferromagnetic metals, for example, $Fe_{75} P_{15} C_{10}$ (Axe et al. (1974)), $(Fe_{1-x}Mo_x)_{80} B_{10} P_{10}$ (Axe et al. (1977)) and crystalline Ni* (Aldred (1975)). In all these cases, the neutron diffraction result for D is significantly (as much as 1.5 times) larger than the $T^{3/2}$ law result.

Another way of looking at the discrepancy is to assume that the neutron diffraction result accounts for all the propagating spin wave states. Then a magnetization is predicted by spin wave theory which decreases too slowly with temperature as compared with experiment. It has therefore been postulated that there are low energy thermal excitations besides spin waves (e.g. local excitations or Stoner single particle excitations) which contribute to the decrease of magnetization with temperature. However, the temperature dependence of M(T) predicted using the spin stiffness coefficient obtained by McColl et al. (1976) from spin wave resonance is substantially in agreement with experiment. (See Table 5.2.) This seems to deny the existence of the postulated additional low lying modes.

*It should be noted here that Birgeneau et al. (1978) have found no such discrepancy in amorphous $(Fe_xNi_{1-x})_{75} P_{16} B_6 Al_3$.

The explanation which resolves all of the above findings is yet to be found.

5.3 The g-Factor

The g-factor of a free electron is known to be 2.0023 (see, for example, Kittel (1971)). The fact that the g-factor of the particles responsible for ferromagnetism is close to 2 means that the particles are electrons. The fact that the g-factor of the electrons is not exactly 2.0023 means that they are not completely free. That is, they have a small amount of orbital character. Since g=1 for orbital motion (i.e. the number of Bohr magnetons of magnetic moment associated with an orbital angular momentum $\vec{h}$ is unity), one would expect the g-factor of the ferromagnetic electrons to be slightly less than 2. Although this is the case when measured by mechanical means, the g-factor found from an electromagnetic experiment is always greater than 2 (usually by approximately 10%). This paradox was first explained by Kittel (1949 or see Advanced Topic M in Kittel (1971) for a simpler explanation) as being due to the fact that the orbital motion is 'quenched' by the lattice. By this is meant that while the magnetic moment associated with the orbital character still contributes to the total magnetic moment, the orbital angular momentum does not contribute to the total angular momentum.

It is reasonable, therefore, to suppose that the deviation of a g-factor from its free electron value is dependent only upon the structure of the material of which the electron is

a part. This hypothesis is borne out by experiment. From FMAR experiments done on nickel at temperatures between room temperature and slightly above T_c it was found (Dewar et al. (1977)) that the g-factor of nickel has the temperature independent value 2.187 $\pm$ 0.005. Also, it was found (Cochran et al. (1977)) that for the amorphous ferromagnet METGLAS 2826, g = 2.053 $\pm$ 0.005 in the temperature range 26 to 270°C. Amorphous Co-P has a metastable structure. Hence, if its g value varied at all with temperature, it would not be expected to do so reversibly. It is for this reason that the apparent variation of g portrayed in Fig. 4.12 is taken to imply the existence of anisotropy and the g-factor (g = 2.124 $\pm$ 0.002) measured by means of FMR at room temperature is assumed to apply at all temperatures. This conclusion is further reinforced by the findings of McColl et al. (1976). For a Co-P sample (whose phosphorus content was very close to that of the present specimen) they found that g = 2.125 $\pm$ 0.007 independent of temperature from 4.2°K to room temperature.

5.4 The Magnetic Anisotropy

It was argued in section 4.3 that the anisotropy implied by the apparent variation of the g value with temperature is unaxial with the sample normal as axis. This type of anisotropy was also found in Co-P by Dietz and Hünseler (1977) from observations of domain patterns, by Chi and Cargill (1975) from measurements of saturation fields, and by McColl et al. (1976) from FMR measurements. The origin of this anisotropy cannot be

determined conclusively from the present experiments. However, a number of possibilities can be convincingly eliminated. A macroscopic gradient in magnetization along the direction of the sample normal is ruled out because it was shown in section 5.1 that $4\pi M_S$ could not have varied by any more than 8 oe in this direction. Another possibility is that the anisotropy was caused by stress arising from the different rates of thermal expansion between the Co-P and the copper diaphragm upon which it was mounted. It is well known (see, for example, Chikazumi (1964)) that a stress σ_s in a ferromagnet results in an anisotropy field $3\lambda_S\sigma_S/M_S$ where λ_S is the (saturation) magnetostriction. The sample was annealled after it had already been mounted. Therefore, assuming that the indium mounting solder did not creep, one would expect the stress, and hence the anisotropy, to be zero at the melting point of indium (450°K). Even in the event of creepage, one could not expect the anisotropy field to be zero at a point below room temperature as was observed (Fig. 4.13). Of the two experimental points shown at 366°K ($4\pi M_S$ = 3.56 kG) in Fig. 4.13, one was deduced from data taken after the temperature had been increasing and the other from data taken after the temperature had been decreasing (i.e., immediately after the 414°K runs). Further, these 2 runs were separated in time by 2 weeks. The fact that they yielded anisotropy fields differing by only (4 ± 8)oe implies not only that the yield stress of the indium was not exceeded at temperatures up to

414°K, but also that creep did not play a significant role. The yield stress of indium is 388 psi at room temperature (Metals Handbook (1961)). From Simpson and Brambly's (1971) measurement on a chemically deposited amorphous Co-P sample with 9 at. % P, $\lambda_S = -4.3 \times 10^{-6}$. This places an upper limit of ~ 40 oe on H_A at room temperature*; and this upper limit is much smaller at the high temperatures used because the yield stress of indium decreases with temperature whereas for isotropic ferromagnets, λ_S falls off with temperature at least as fast as the magnetization (usually $\lambda_S \propto M_S^2$). The conclusion therefore is that stress effects cannot be responsible for most of the observed anisotropy field.

The observed anisotropy field may have been caused by compositional inhomogeneity. Using specimens prepared in the same way as ours, Chi and Cargill (1975) deduced the presence of prolate ellipsoidal (needle-shaped) inclusions in the Co-P. The needles were oriented with their long axes parallel to the growth direction; that is, normal to the specimen plane. This model is consistent with the results for the damping parameter as discussed in section 5.1. Using this model along with the assumption that the exchange interaction is strong enough to hold the spins inside and outside the inclusions parallel, one finds an anisotropy energy (Brown and

---

*There is a factor of 40 involved in calculating the stress inside the Co-P because the cross-sectional area of the Co-P sample was one-fortieth the area of contact between the indium and the Co-P.

Morrish (1957)).

$$E_A = \pi\beta(M - M')^2 \sin^2\theta \qquad (5.3)$$

where $\beta(<< 1)$ is the volume fraction that the inclusions occupy. M' is the magnetization in the inclusions, and θ is the angle between the bulk magnetization and the sample normal. This yields an anisotropy field*

$$H_A = 2\pi\beta(M - M')^2/M \qquad (5.4)$$

Assuming that M' is not as strongly temperature dependent as M, the only way in which this anisotropy field can decrease with increasing magnetization is if M' > M; implying thereby that the inclusions are cobalt-rich. This also is consistent with the damping parameter results. However, an anisotropy field of the form 5.4 is neither linear in M nor does it pass through zero.

The assumption that the spins inside the inclusions are parallel to those of the bulk breaks down when the inclusions are separated by an average distance much larger than an exchange length (an exchange length being defined as one Bloch

*The singularity in this expression at M=0 has no significance because the assumption that $\vec{M}$ and $\vec{M}'$ are parallel breaks down long before M approaches zero. It arises because the local inhomogeneity is assumed to exert a torque on all the bulk spins (by the mechanism of the exchange interaction).

wall thickness $\sim \sqrt{A}/M \sim 100$ Å in the present case). This is because one inclusion can only be expected to exert a torque on those spins which are within one exchange length of it. Using $\beta \sim 0.005$ as deduced from the λ results (section 5.1) and a diameter of the inclusions ~ 100 Å (Chi and Cargill (1975)) we find that the inclusions are separated by a distance large compared with the exchange length. Therefore, it would seem that the assumption that $\vec{M}$ and $\vec{M}'$ are decoupled is most appropriate.

If $\vec{M}$ and $\vec{M}'$ are decoupled, then the anisotropy field is

$$H_A = 2\pi M\beta \qquad (5.5)$$

This result follows from a magnetostatic calculation of the energy of the system in which the direction of the inclusion magnetization is held fixed along the direction of the long axis of the inclusion, but the direction of the bulk magnetization is allowed to vary. The anisotropy field given by (5.5) is, however, inconsistent with the data because it increases as the average magnetization increases. Possibly, an intermediate-strength coupling between the inclusions and the bulk could result in the observed dependence of H_A on magnetization. However, the solution for the general case of the response of an inhomogeneous magnetic system to an external field is a very difficult problem which has not been solved.

CHAPTER 6

CONCLUSION

The transmission of microwaves through amorphous Co_3P between 5 and 414°K could be successfully described by an equation of motion which used the Landau-Lifshitz form of the damping term. The damping parameter, λ, necessary for this description varied by only a few percent with temperature and configuration. The value of λ was found to be approximately $1.6 \times 10^8 sec^{-1}$; of the same order of magnitude as the damping parameters of crystalline ferromagnets.

Two other forms of the damping term were also considered. The Gilbert damping parameter was essentially the same as the Landau-Lifshitz damping parameter; the Bloch-Bloembergen damping parameter, however, varied by a factor of 2.5 over the temperature range studied. It is clear, therefore, that the Landau-Lifshitz or the Gilbert form of the damping gave a simpler description of the microwave frequency properties of the amorphous Co_3P specimen than the Bloch-Bloembergen form did.

The saturation magnetization required to fit the observed transmission curves was found to vary with temperature in the manner which is characteristic of amorphous ferromagnets. The spin wave dispersion coefficient, D, found by fitting the low temperature (5 - 79°K) magnetization to the Bloch $T^{3/2}$ law was essentially in agreement with those previously-published values which had been obtained by direct measurements of the magnetization. However, this value for D was significantly smaller than the single previously-published result obtained

from neutron diffraction experiments. The explanation which resolves the discrepancy is not known.

The microwave transmission data was interpreted on the basis of the assumption that the intrinsic g-factor of amorphous Co_3P is independent of temperature. This assumption forced the postulation of the existence of magnetic anisotropy in the specimen. Further, it was found that the anisotropy was uniaxial in nature with axis parallel to the specimen normal. The magnitude of the anisotropy field was found to decrease linearly with the saturation magnetization. In particular, this field changed by approximately 150 oe over the temperature range studied.

The variation of λ with temperature and configuration and the variation of the anisotropy field with magnetization appears to be consistent with a model of oriented, cobalt-rich inhomogeneities in the specimen.

APPENDIX A

A More General Spin Wave Dispersion Relation

Inside a ferromagnetic continuum, let $\vec{e}$, $\vec{h}$, and $\vec{m}$ be the space-time dependent components of the electric field, the magnetic field and the magnetization respectively. With neglect of the tensor properties of the conductivity, σ, and of the dielectric constant, ϵ, Maxwell's equations take the form:

$$\text{curl}\ \vec{h} = \frac{\epsilon}{c}\frac{\partial \vec{e}}{\partial t} + \frac{4\pi\sigma}{c}\vec{e} \qquad \text{(A.1a)}$$

$$\text{curl}\ \vec{e} = -\frac{1}{c}\frac{\partial \vec{h}}{\partial t} - \frac{4\pi}{c}\frac{\partial \vec{m}}{\partial t} \qquad \text{(A.1b)}$$

$$\text{div}\,(\vec{h} + 4\pi\vec{m}) = 0 \qquad \text{(A.1c)}$$

Assuming that $\vec{e}$, $\vec{h}$, and $\vec{m}$ vary in space and time as $e^{i(\vec{k}\cdot\vec{r} - \omega t)}$ yields the solution

$$\vec{h} = \frac{\frac{4\pi\omega\bar{\sigma}}{c^2}\, i(4\pi\vec{m}) - 4\pi(\vec{k}\cdot\vec{m})\vec{k}}{k^2 - \frac{4\pi\omega\bar{\sigma}}{c^2}\, i} \qquad \text{(A.2)}$$

where

$$\bar{\sigma} \equiv \sigma - i\,\omega\,\frac{\epsilon}{4\pi}$$

Typically, for a metal, $\sigma \gtrsim 10^{16}\ \text{sec}^{-1}$. (As a metal, Co-P is

a relatively poor conductor with a resistivity of $\sim 10^{-4}\Omega$cm. This corresponds to a conductivity in electrostatic units of $\sim 10^{16}\ \text{sec}^{-1}$.) For thermal spin waves, $\hbar\omega \sim k_B T$. Hence, the imaginary part of $\bar{\sigma}$ has a magnitude $\sim \frac{k_B T}{\hbar}\frac{\varepsilon}{4\pi} \sim \frac{k_B T}{2h}$. Even for temperatures as high as 10^3° K, this amounts to only $10^{13}\ \text{sec}^{-1}$; much less than σ, the real part of $\bar{\sigma}$. Therefore, for Co-P (or any metal having a lower resistivity), one may ignore the effects of the displacement current upon thermal spin waves up to temperature of order 10^3 °K.

When calculating the response of a ferromagnet to microwave radiation, one must use the complete solution of Maxwell's equations (A.2). However, if (A.2) is to be applied to the case of thermal spin waves, it can be simplified considerably because $k^2 >> 4\pi\omega\sigma/c^2$. To see this, let us use the approximate dispersion relation $\hbar\omega = Dk^2$ (2.19). In that case, $4\pi\omega\sigma/c^2 = \frac{4\pi\sigma}{\hbar c^2} Dk^2$ and it remains only to show that $\frac{4\pi\sigma D}{\hbar c^2} << 1$, or, $\sigma << \frac{\hbar c^2}{4\pi D}$. Experimentally, it has been found that the spin wave dispersion constant, D, is never larger than ~ 1 eV Å^2. For this value of D, $\frac{\hbar c^2}{4\pi D} \sim 10^{20}\ \text{sec}^{-1}$ which is indeed much larger than the conductivity of all but very pure single crystal ferromagnets. Hence, at least in the case of amorphous ferromagnets, eddy-current damping of thermal spin waves is negligible. To a very good approximation, we can therefore rewrite (A.2) as

$$\vec{h} = -(4\pi/k^2)(\vec{k}\cdot\vec{m})\vec{k} \qquad (A.3)$$

From chapter 2, the reader knows of another relation between $\vec{m}$ and $\vec{h}$, namely, the equation of motion (2.39). Using the definition of γ (2.3) and A (2.26), (2.39) can be written in the form

$$i\hbar\omega\vec{m} = \vec{m}\times\left(g\mu_B\vec{H}_N + Dk^2 - i\hbar\omega\frac{G}{\gamma}\frac{1}{M_S}\right) - g\mu_B\vec{h}\times\vec{M}_S \quad \text{(A.4)}$$

($\vec{H}_N$ is the internal static magnetic field and G is the Gilbert magnetic damping parameter.) For Co-P, $G/\gamma \approx 10$ oe while M_S at low temperatures is approximately 500 gauss. By using the approximate dispersion relation, $\hbar\omega = Dk^2$, we can see that (at least in the case of Co-P) the magnetic damping of thermal spin waves is unimportant. By neglecting the damping term in (A.4) and using (A.3) for $\vec{h}$, the matrix form of (A.4) is*

$$\begin{pmatrix} g\mu_B(4\pi M)\frac{k_x k_y}{k^2} - i\hbar\omega & g\mu_B\left(H_N + 4\pi M\frac{k_y^2}{k^2}\right) + Dk^2 \\ g\mu_B\left(H_N + 4\pi M\frac{k_x^2}{k^2}\right) + Dk^2 & g\mu_B(4\pi M)\frac{k_x k_y}{k^2} + i\hbar\omega \end{pmatrix}\begin{pmatrix} m_x \\ m_y \end{pmatrix} = \begin{pmatrix} 0 \\ 0 \end{pmatrix} \quad \text{(A.5)}$$

The vector $\vec{m}$ lies in the xy-plane because a co-ordinate system has been chosen in which $\vec{M}_S$ (and hence also $\vec{H}_N$) is in the

*No importance should be attached to the fact that M_S has been replaced by M. While the vectors $\vec{M}_S$ and $\vec{M}$ are different ($\vec{M} = \vec{m} + \vec{M}_S$), the difference between the magnitudes M_S and M is of second order.

z-direction. (Note that this differs from the co-ordinate system of Fig. 2.1.) By demanding that the determinant of the matrix in (A.5) be zero, one obtains a dispersion relation which after considerable algebraic manipulation becomes

$$(\hbar\omega)^2 = (Dk^2 + g\mu_B H_N)\left[Dk^2 + g\mu_B (H_N + 4\pi M_s \sin^2\theta)\right] \qquad (A.6)$$

where θ is the angle between $\vec{k}$ and $\vec{M}_S$.

Equation (A.6) differs from the approximate dispersion relation $\hbar\omega = Dk^2$ (2.19) in two important respects. (1) The energy of a spin wave of a given wavevector has been increased by at least $g\mu_B H_N$. This is due to the Zeeman term $\vec{\mu}\cdot\vec{H}_N$ in the Hamiltonian of the spin system. (2) There is now a range of possible wavenumbers for a single magnon energy. This occurs because of the dipole-dipole interaction resulting from the non-uniformity of $\vec{M}$ in the bulk. One possible objection to the dispersion relation (A.6) is that it leads to the absurd conclusion that the energy of a 'uniform precession spin wave' (that is, a magnon for which $\vec{k} = 0$) depends upon its direction. The reason is that in treating the dipole-dipole interactions as resulting in a static demagnetizing field $\vec{N}\vec{M}_S$ and a temporally and spatially varying field (A.3), we have neglected the demagnetizing effect resulting from the discontinuity of $\vec{m}$ at the specimen surface. For spin waves with wavelengths much shorter than a typical sample dimension, $\vec{m}$ varies sufficiently

rapidly over the sample surface that the effects of its discontinuity there average to zero. If, on the other hand, the spin waves in which we are interested have wavelengths comparable to a sample dimension, the boundaries of the ferromagnet must be properly taken into account. It is then found that there no longer exists a continuum of magnon states but rather a set of discrete magnetostatic modes. These modes are known as the Walker modes after L.R. Walker (1957). Using $k^2 \sim \hbar\omega/D \sim k_B T/D$, we find that above 1°K, thermal excitation of the Walker modes should only be important for specimen sizes of less than a few hundred angstroms.

By the same method as that of section 2.1.4, one can now use the dispersion relation (A.6) to find the magnetization as a function of temperature and applied field. However, the required integration over $\vec{k}$-space can only be performed numerically. It is much simpler (and, in the end, more enlightening) to solve the problem by making a few more approximations. One can show (Keffer (1966), section 17) that for magnons with energies that satisfy $\hbar\omega >> g\mu_B(4\pi M_S)$, the $\sin^2\theta$ term in (A.6) can be replaced by its average and the dispersion relation becomes approximately,

$$\hbar\omega = Dk^2 + g\mu_B(H_N + (4/3)\pi M_S) \qquad (A.7)$$

This is a very pleasing result: the first order correction to the internal field which results from taking into account the dipole-dipole field (A.3) is simply the Lorentz field, $(4/3)\pi M$.

Recognizing that $\hbar\omega \sim k_B T$, one can see that the necessary inequality ($\hbar\omega >> g\mu_B(4\pi M)$) is satisfied in our case ($4\pi M$ = 6400 gauss) if $T >> 1°K$.

Using the approximate dispersion relation (A.7) in the k-space integral (2.21) results in the following expression for magnetization

$$M_o - M(T) = g\mu_B \left(\frac{k_B T}{4\pi D}\right)^{3/2} \sum_{p=1}^{\infty} p^{-3/2} \exp\left[\frac{-g\mu_B}{k_B T}\left(H_N + \frac{4}{3}\pi M\right)p\right] \quad (A.8)$$

In general, the sum in this expression is very slowly converging and so the series:

$$\sum_{p=1}^{\infty} p^{-3/2} e^{-p/x} \doteq 2.612 - 3.54X^{1/2} + 1.46X - 0.104X^2 + \cdots \quad (A.9)$$

is numerically more convenient (Charap (1960)).

APPENDIX B

Experimental Values of g, $4\pi M_S$ and H_A

The following is a table of the values of g, $4\pi M_S$, and H_A for amorphous Co_3P as deduced from the experimentally measured FMAR line positions at various temperatures. The first column contains the temperatures at which the FMAR runs were made. The second and third columns contain, respectively, $4\pi M_S$ and the g-factor; both obtained by assuming that there was no anisotropy. The fourth column contains the values of the anisotropy field obtained by assuming that the g-factor was in fact independent of temperature and that the apparent temperature variation (in column 3) was due solely to a temperature dependent anisotropy field. In particular, it was assumed that the g-factor was 2.124 ± 0.002 as obtained from the room temperature FMR results and that the anisotropy was uniaxial with axis perpendicular to the plane of the sample. The presence of such anisotropy implies that what was thought to be $4\pi M_S$ in column 2 is actually $4\pi M_{eff} = 4\pi M_S - 3/2\ H_A$. Assuming that H_A varied linearly with $4\pi M_S$ as in equation (4.6), the corrected values of $4\pi M_S$ are given by equation (4.7). The adjusted values of $4\pi M_S$ have been listed in column 5.

T(°K)	$4\pi M_{eff}$(kG)	g	H_A(oe)	$4\pi M_S$(kG)
5±.5	6.416±0.004	2.1112±0.0008	-48±2	6.352
12.5±.5	6.405±0.004	*	*	6.342
23.5±.5	6.388±0.004	———	———	6.325
38 ±.5	0.356±0.004	———	———	6.295
40.7±.5	6.349±0.004	———	———	6.289
52.5±.5	6.318±0.004	———	———	6.259
65 ± 1	6.271±0.004	2.1120±0.0008	-44±2	6.214
72 ± 1	6.247±0.004	2.1110±0.0008	-43±2	6.192
79 ± 1	6.214±0.004	2.1120±0.0008	-48±2	6.160
125 ± 1	5.992±0.005	2.1150±0.0008	-32±2	5.950
173 ± 1	5.711±0.005	2.1190±0.0008	-16±2	5.683
274 ± 1	4.819±0.005	2.127 ±0.001	13±3	4.837
298 ± 1	4.547±0.005	2.131 ±0.001	28±3	4.579
304 ± 2	4.477±0.006	2.130 ±0.001	27±3	4.512
319 ± 2	4.284±0.006	2.131 ±0.001	29±3	4.329
333 ± 2	4.083±0.006	2.134 ±0.001	38±3	4.139
348 ± 2	3.870±0.007	2.135 ±0.001	43±3	3.936
366 ± 2	3.560±0.008	2.138 ±0.001	52±3	3.642
379 ± 2	3.31 ±0.01	2.139 ±0.001	60±4	3.41
395 ± 2	3.02 ±0.03	2.142 ±0.001	69±5	3.13
404 ± 2	2.83 ±0.05	2.144 ±0.002	76±7	2.95
414 ± 2	2.57 ±0.20	2.149 ±0.003	91±11	2.70

*No FMAR runs were made in the perpendicular configuration for temperatures between 5 and 65 K.

APPENDIX C

Index of Symbols

A symbol which is introduced as a vector may appear in the text as a scalar. In that case, it refers only to the magnitude of that particular vector. If it appears as a scalar with the subscript x,y, or z, then it refers to the x, y, or z component of the vector.

Symbol	Description	Equation or place of first occurrence.
A	exchange stiffness parameter	(2.26)
$A_{\parallel}$	maximum transmitted amplitude in the parallel configuration	Fig. 4.9
$A_{\perp}$	maximum transmitted amplitude in the perpendicular configuration	Fig. 4.9
a	nearest neighbour distance	Sec. 2.1.4
$\vec{B}_N$	internal magnetic induction ($= \vec{H}_N + 4\pi\vec{M}_S$)	Sec. 2.2.2b
$B_{3/2}$	dimensionless $T^{3/2}$ coefficient	(5.1)
$\vec{b}$	r.f. magnetic induction	Sec. 2.2.2b
b_p	surface spin pinning parameter	(2.42)
c	speed of light	(2.3)
D	spin wave dispersion coefficient	(2.12)
$\vec{\vec{D}}$	demagnetization tensor ($= \frac{1}{4\pi}\vec{\vec{N}}$)	Sec. 3.1
D_x, D_y, D_z	diagonal components of $\vec{\vec{D}}$	Sec. 3.1
d	specimen thickness	Sec. 2.2.1
E	energy	(2.1)
E_A	anisotropy energy	(2.67)
$\vec{e}$	r.f. electric field	Sec. 2.1.6

Symbol	Description	Equation or place of first occurrence
e	3 meanings: (1) magnitude of $\vec{e}$	Sec. 2.1.6
	(2) electronic elementary charge	(2.3)
	(3) fundamental constant (~2.7183)	~~~
F	$4\pi M_S \ln(2^{3/2} A_\perp / A_\parallel)$	Fig. 4.9
G	Gilbert damping parameter	(2.28)
$G(x)$	$2.612 - 3.54\, x^{\frac{1}{2}} + 1.46\, x - 0.104\, x^2$	(4.3), (A.9)
g	spectroscopic splitting factor	(2.3), Sec.4.3
$\vec{H}$	magnetic field	(2.1), (2.4)
$\vec{H}_o$	static part of magnetic field	Sec. 2.2.1
H_A	anisotropy field	(2.68)
$\vec{H}_D$	demangetization field	(2.10)
H_E	$2A/(M_S \delta^2)$	(2.46)
$\vec{H}_{eff}$	internal field plus exchange effective field	(2.13)
$\vec{H}_{EX}$	exchange effective field	(2.12)
ΔH_{ex}	exchange contribution to FMR abosrption line width	(2.48)
H_F	$H_N + (2A/M_S)k^2 - (i/M_S)(G/\gamma)(\omega/\gamma)$	(2.44)
H_L	magnetic damping effective field	(2.52)
$\vec{H}_N$	static part of internal magnetic field	(2.30), (2.39)
$\vec{h}$	r.f. magnetic field	(2.30), (2.39)
$\vec{h}_\parallel$	vector component of $\vec{h}$ in the direction parallel to $\vec{M}_S$	Sec. 2.1.6
$\vec{h}_\perp$	$\vec{h} - \vec{h}_\parallel$	(2.30)
$h_\pm$	$h_x \pm i\, h_y$	Sec. 2.2.2

Symbol	Description	Equation or place of first occurrence
$\vec{h}_{ij}$	field at site of i^{th} dipole caused by j^{th} dipole	(2.8)
$\hbar$	Planck's constant divided by 2π	(2.2)
i	$\sqrt{-1}$	—
$J(r)$	exchange integral	Sec. 5.2
K	anisotropy constant	(2.67)
$\vec{k}$	thermal spin wave vector or r.f. wavevector	(2.18), (A.2)
k_B	Boltzmann's constant	(2.21)
$\vec{M}$	local magnetic moment per unit volume: a function of both space and time within a ferromagnet	(2.24)
M_o	saturation magnetization at $T = 0$	(2.20)
$\vec{M}_L$	vector component of $\vec{M}$ in the direction of $\vec{M}_S$.	(2.29)
$\vec{M}_S$	saturation magnetization (static part of $\vec{M}$): assumed to be independent of position	(2.9), (2.20)
M'_S	magnetization of inhomogeneities	Sec. 5.1
$\vec{M}_T$	$\vec{M} - \vec{M}_L$	(2.29)
$\vec{m}$	r.f. part of $\vec{M}$	(2.30), (2.38)
$m_{\pm}$	$m_x + i\, m_y$	Sec. 2.2.2
m_e	mass of the electron	(2.3)
N	total number of elementary dipoles in the specimen	(2.20)
$\vec{\vec{N}}$	demagnetization tensor	(2.10)
N_x, N_y, N_z	diagonal components of $\vec{\vec{N}}$	(2.60)
n	total number of magnons	(2.20)

Symbol	Description	Equation or place of first occurrence
n_ω	total number of magnons of frequency ω	(2.20)
p	specimen aspect ratio	(3.5)
$\vec{r}$	general position vector (=(x,y,z))	—
$\vec{r}_{ij}$	position vector connecting i^{th} and j^{th} spin sites	(2.8)
$\vec{s}$	electron spin angular momentum	(2.5)
T	temperature	—
t	time	—
V	total volume of specimen	(2.9)
x,y,z	Cartesian position coordinates	—
α	2 meanings: (1) $\left[\lambda/(\gamma M_S)\right]^2$	Sec. 4.1a
	(2) slope of H_A vs. $4\pi M_S$ plot	(4.6)
β	fraction of the specimen volume occupied by inhomogeneities	Sec. 5.1
γ	gyromagnetic ratio	(2.3)
γ_G	gyromagnetic ratio in the Gilbert formalism	(2.31)
γ_{LL}	gyromagnetic ratio in the Landau-Lifshitz formalism	(2.34)
δ	a scaling length related to the classical skin depth (= $\left[c^2/(4\pi\omega\sigma)\right]^{\frac{1}{2}}$)	(2.40)
ε	specimen dielectric constant	Sec. 2.2.1, (A.2)
θ	angle between specimen normal and $\vec{M}_S$	(2.59)
λ	Landau-Lifshitz damping parameter	(2.27)

Symbol	Description	Equation or place of first occurrence
$\lambda_{\parallel}$	λ for the parallel configuration	Sec. 4.1
$\lambda_{\perp}$	λ for the perpendicular configuration	Sec. 4.1
λ_S	saturation magnetostriction	Sec. 5.4
$\vec{\mu}$	magnetic dipole moment (general)	(2.1)
$\vec{\mu}_i$	magnetic dipole moment of i^{th} spin	Sec. 2.1.1
$\vec{\mu}(\vec{r})$	a continuous function constructed such that $\vec{\mu}(\vec{r}_i) = \vec{\mu}_i$	(2.12)
μ_B	the Bohr magneton	(2.3)
μ_{RF}	proportionality constant (in general, a tensor) between $\vec{b}$ and $\vec{h}$	(2.50)
$\mu_{RF\pm}$	$b_\pm/h_\pm$	(2.50)
ρ	electrical resistivity	Sec. 3.1
σ	electrical conductivity	(2.40)
$\bar{\sigma}$	conductivity which includes the effects of the displacement current	(A.2)
σ_S	internal stress	Sec. 5.4
$\vec{\tau}$	torque vector	(2.4)
$\vec{\tau}_A$	anisotropy torque	(2.68)
τ_o	spin relaxation time constant	(2.36)
τ_1	transverse spin relaxation time constant	(2.29)
τ_2	longitudinal spin relaxation time constant	(2.29)
χ_{RF}	proportionality constant (in general, a tensor) between $\vec{m}$ and $\vec{h}$	(2.43)
$\chi_{RF\pm}$	$m_\pm/h_\pm$	(2.45)
ω	angular frequency	(2.2)

BIBLIOGRAPHY

Aldred, A.T.: Phys. Rev. B11, 2597 (1975).

Ament, W.S. and G.T. Rado: Phys. Rev. 97, 1558 (1955).

Argyle, B.E., S.H. Charap, and E.W. Pugh: Phys. Rev. 132, 2051 (1963).

Axe, J.D., L. Passell, and Tsuei: AIP Conf. Proc. 24, 119 (1974).

Axe, J.D., G. Shirane, T. Mizoguchi, and K. Yamauchi: Phys. Rev. B15, 2763 (1977).

Bailey, G.C. and C. Vittoria: Phys. Rev. Lett. 28, 100 (1972).

Bailey, G.C. and C. Vittoria: Phys. Rev. B8, 3247 (1973).

Berrada, A., M.F. Lapierre, B. Loegel, P. Panissod, C. Robert and J. Beille: Physica 86-88B, 790 (1977).

Bhagat, S.M., L.L. Hirst, and J.R. Anderson: J. Appl. Phys. 37, 194 (1966).

Bhagat, S.M., S. Haraldson, and O. Beckman: J. Phys. Chem. Solids 38, 593 (1977).

Birgeneau, R.J., J.A. Tarvin, G. Shirane, E.M. Gyorgy, R.C. Sherwood, and H.S. Chen: Phys. Rev. B18, 2192 (1978).

Bloch, F.: Z. Physik 61, 206 (1930).

Bloembergen, N.: Phys. Rev. 78, 572 (1950).

Brenner, A., D.E. Couch, and E.K. Williams: J. Res. Natl. Bur. Std. 44, 109 (1950).

Brown, Jr., W.F.: "Magnetostatic Principles in Ferromagnetism". Amsterdam: North-Holland Publ. Co. (1962).

Brown, Jr., W.F. and A.H. Morrish: Phys. Rev. 105, 1198 (1957).

Cargill III, G.S.: Solid State Phys. 30, 227 (1975).

Charap, S.H.: Phys. Rev. 119, 1538 (1960).

Chi, G.C.: Ph.D. thesis (unpublished) (1977).

Chi, G.C. and G.S. Cargill III: AIP Conf. Proc. 29, 147 (1975).

Chi, G.C. and G.S. Cargill III: AIP Conf. Proc. 31, 359 (1976).

Chien, C.L. and R. Hasegawa: Phys. Rev. B16, 2115 (1977).

Chikazumi, S.: "Physics of Magnetism". New York: John Wiley & Sons Inc. (1964).

Cochran, J.F., B. Heinrich, and R. Baartman: Physica 86-88B, 807 (1977).

Cochran, J.F., B. Heinrich, and G. Dewar: Can. J. Phys. 55, 787 (1977a).

Cochran, J.F., B. Heinrich, and G. Dewar: Can. J. Phys. 55, 834 (1977b).

Cochrane, R.W. and G.S. Cargill III: Phys. Rev. Lett. 32, 476 (1974).

Dewar, G.: "Ferromagnetic Antiresonant Microwave Transmission through Nickel". Unpublished Ph.D. thesis (1978).

Dewar, G., B. Heinrich, and J.F. Cochran: Can. J. Phys. 55, 821 (1977).

Dietz, G.: J. Mag. Mag. Mat. 6, 47 (1977).

Dietz, G. and A. Hunseler: J. Mag. Mag. Mat. 6, 68 (1977).

Frait, Z.: Czech. J. Phys. 9, 750 (1959).

Gilbert, T.L.: Phys. Rev. 100, 1243 (1955).

Handrich, K.: Phys. Stat. Sol. 32, K55 (1969).

Handrich, K. and S. Kobe: Acta Phys. Polon. A38, 819 (1970).

Heinrich, B., J.F. Cochran, and R. Baartman: Can. J. Phys. 55, 806 (1977).

Heinrich, B. and V.F. Meshcheryakov: ZhETF Pis. Red. 9, 618 (1969).

Heinrich, B. and V.F. Meshcheryakov: ZhETF 59, 424 (1970).

Herring, C. and C. Kittel: Phys. Rev. 81, 869 (1951).

Holstein, T. and H. Primakoff: Phys. Rev. 58, 1098 (1940).

Kaganov, M.: Fiz. Met. Met. 7, 287 (1959).

Kambersky, V.: Czech. J. Phys. B26 (1976).

Kasuya, T. and R.C. LeCraw: Phys. Rev. Lett. 6, 223 (1961).

Keffer, F.: Handbuch der Physik 18/2, 1 (1966).

Keffer, F. and R. Loudon: J. Appl. Phys. 32, 2S (1961); erratum 33, 250 (1962).

Kittel, C.: Phys. Rev. 76, 743 (1949).

Kittel, C.: "Introduction to Solid State Physics." New York: John Wiley & Sons Inc. (4th ed., 1971).

Korenman, V., J.L. Murray, and R.E. Prange: Phys. Rev. B16, 4032 (1977).

Kraus, L. and Z. Frait: Czech. J. Phys. B23, 188 (1973).

Krey, V.: Z. Physik B31, 247 (1978).

Landau, L. and E. Lifshitz: Phys. Z. Sowjetunion 8, 153 (1935).

McColl, J.R., D. Murphy, G.S. Cargill III, and T. Mizoguchi: AIP Conf. Proc. 29, 172 (1976).

Metals Handbook, ed. by T. Lyman: American Society for Metals, Metals Park, Ohio (8th ed., 1961).

Mook, H.A., N. Wakabayashi, and D. Pan: Phys. Rev. Lett. 34, 1029 (1975).

Pan, D. and D. Turnbull: J. Appl. Phys. 45, 1406 (1974).

Prange, R.E. and V. Korenman: Phys. Rev. B19, 4691 (1979).

Rado, G.T. and J.R. Weertman: J. Phys. Chem. Sol. 11, 315 (1959).

Rao, K.V., H. Gundmundsson, H.U. Aström, and H.S. Chen: J. Appl. Phys. 50(3), 1592 (1979).

Shenker, H., J.I. Lauritzen, Jr., R.J. Corruccini, and S.T. Lonberger: Natl. Bur. Standards (U.S.) Report 561 (1955).

Simpson, A.W. and D.R. Brambly: Phys. Stat. Sol. B43, 291 (1971).

Sparks, L.L., R.L. Powell, and W.J. Hall: Natl. Bur. Standards (U.S.) Report 9712 (1968).

Sparks, M.: "Ferromagnetic Relaxation Theory." New York: McGraw-Hill Book Co. (1964).

Stoner, E.C.: Proc. Roy. Soc. (London) A165, 376 (1938).

Vonsovskii, S.V.; editor: "Ferromagnetic Resonance". New York: Pergamon Press Inc. (1966).

Walker, L.R.: Phys. Rev. 105, 390 (1957).

Weiss, P. and R. Forrer: Ann. Phys. 5, 153 (1926).